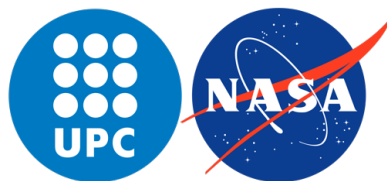# Connecting the Grad-Shafranov Reconstruction Technique to Flux-rope Models

NASA Goddard Space Flight Center

Heliophysics Science Division (HSD)

Universitat Politècnica de Catalunya

Jordi Jumilla Lorenz

Bachelor's Thesis

Degree in Engineering Physics - Degree in Mathematics

Supervisor (NASA GSFC): Teresa Nieves Chinchilla
Co-supervisor (UPC): Gloria Sala Cladellas

May 2021

UNIVERSITAT POLITÈCNICA DE CATALUNYA
BARCELONA**TECH**
Facultat de Matemàtiques i Estadística

UNIVERSITAT POLITÈCNICA DE CATALUNYA
BARCELONA**TECH**
Centre de Formació Interdisciplinària Superior

UNIVERSITAT POLITÈCNICA DE CATALUNYA
BARCELONA**TECH**
Escola Tècnica Superior d'Enginyeria
de Telecomunicació de Barcelona

telecos
BCN

Abstract

English:

The Grad-Shafranov reconstruction technique (GSRT) is a well-established methodology based on a fundamental magnetohydrodynamics (MHD) equation that has been widely applied to analyse magnetic flux ropes from in-situ measurements of spacecrafts. These structures are also traditionally reconstructed based on analytical models. One of them, the 2016 Circular-Cylindrical (CC) model and its extension to complex geometries, 2018 Elliptical-Cylindrical (EC) model have also been proven to describe, with high level of accuracy, the magnetic flux ropes. The goal of this research is to determine what are the connections between the above mentioned methods. An updated and easy-to-use version of the GSRT has been developed using Python. This tool has been used to reconstruct synthetic events using simulated in-situ measurements created with the CC and EC models. Finally, the GSRT has been applied to reconstruct a real event observed by STEREO A, and used to infer the properties of the magnetic fields, current densities, distortion and other geometrical parameters.

Català:

La tècnica de reconstrucció de Grad-Shafranov (GSRT) és una metodologia ben establerta basada en una equació fonamental de la magnetohidrodinàmica (MHD). Aquest mètode ha estat àmpliament aplicat en l'anàlisi de cordes de flux magnètic a partir de mesures in-situ de missions espacials. Aquestes estructures magnètiques han sigut tradicionalment reconstruïdes utilitzant models analítics. Un d'ells, el circular-cilíndric (CC) de 2016 i la seva extensió a geometries més complexes, l'el·líptic-cilíndric (EC) de 2018 han demostrat ser capaços de descriure, amb alt nivell de precisió, les cordes de flux magnètic. L'objectiu d'aquesta investigació és determinar les connexions entre els mètodes descrits anteriorment. Una versió actualitzada i fàcil d'usar de la GSRT ha estat desenvolupada amb Python. Aquesta eina ha estat utilitzada per a reconstruir esdeveniments amb mesures in-situ simulades creades amb els models CC i EC. Finalment, la GSRT ha estat aplicat a la reconstrucció d'un esdeveniment real observat per STEREO A, i usada per inferir les propietats dels camps magnètics, densitats de corrent, distorsió i altres paràmetres geomètrics.

Castellano:

La técnica de reconstrucción de Grad-Shafranov (GSRT) es una metodología bien establecida basada en una ecuación fundamental de la magnetohidrodinámica (MHD). Este método ha sido ampliamente aplicado en el análisis de cuerdas de flujo magnético a partir de medidas in-situ de misiones espaciales. Estas estructuras magnéticas han sido tradicionalmente reconstruidas usando modelos analíticos. Uno de ellos, el circular-cilíndrico (CC) de 2016 y su extensión a geometrías más complejas, el elíptico-cilíndrico (EC) de 2018 han demostrado ser capaces de describir, con alto nivel de precisión, las cuerdas de flujo magnético. El objetico de esta investigación es determinar las conexiones entre los métodos descritos anteriormente. Una versión actualizada y fácil de usar de la GSRT ha sido desarrollada en Python. Esta herramienta ha sido utilizada para reconstruir eventos con medidas in-situ simuladas creadas con los modelos CC y EC. Finalmente, la GSRT ha sido aplicada a la reconstrucción de un evento real observado por STEREO A, y usada para inferir las propiedades de campos magnéticos, densidades de corriente, distorsión y otros parámetros geométricos.

Acknowledgements

Contents

1. The Sun and Large Scale Structures

The Sun is our star. It is situated in the center of the Solar System at around 150 million kilometers from Earth. It has been an object of study for millennia since it is related to life on Earth in a very direct manner: it dictates the light hours, year seasons, weather, temperatures...

After the Sun, the nearest star system is Alpha Centauri, which is more than 4 light-years away from the Sun. This means that it is more than 250 thousand times further from Earth than the Sun. Even if the study of other stars may be very important, with the technology available nowadays it is impossible to study other stars as precisely as the Sun. This is why the Sun is the best representative of a star available to us, and unveiling its mysteries may help us learn more from further stars.

1.1 The Sun and the Heliosphere

The Sun has an internal structure, called the Solar interior. It can be divided into three different layers, from the innermost to the outermost part of the Sun:

- **Core**: it extends from the center to around $0.2R_s$. Thermonuclear reactions occur in this region, resulting in high density and high temperatures (around 15 million K). It is the densest zone, contributing to around 50% of the Sun's mass but only to around 2% of its volume.

- **Radiative zone**: it extends from the core to around $0.7R_s$. The energy from the core is transferred by photons to the external part of the radiative zone. This region is composed of high density plasma (mainly ionized hydrogen, helium and free electrons). Due to the high density of the plasma, photons are absorbed and re-emitted a large number of times.

- **Convective zone**: it extends from the radiative zone to 1 R_s. In this zone, the solar gas is no longer ionized and photons are absorbed easily. Thus, the energy transfer is no longer done by radiation but by convection. Heat is transferred in a non-homogeneous and turbulent manner. Buoyancy forces result in ups and downs motion of the solar gas, resulting in convection cells of many different sizes.

The Sun has its atmosphere, which can also be divided into multiple regions. From the lower layer to the uppermost one:

- **Photosphere**: it sits on the top part of the convective zone. It is an extremely thin layer, with a thickness of around 100 to 200 km. This layer is considered the Sun's surface when observed by a telescope. Due to the convective motion in the convective zone, hot gas is brought up to the photosphere where the excess of energy is radiated away. Thus the hot gas cools down, loses its buoyancy and, as a result, it sinks. This convective motion results in small-scale granular patterns, forming the so-called supergranular network. The Sun spots are thought to be regions of intense magnetic field. Sun spots usually come in pairs of opposite polarities and can last from one day to several weeks.
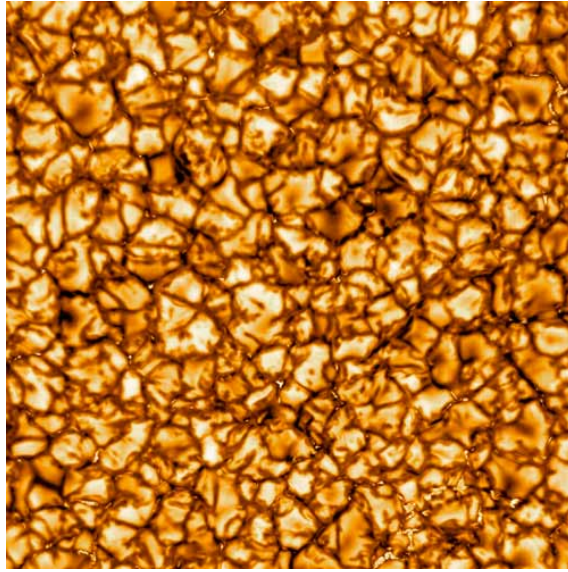
Figure 1.1: Details of the photosphere. Retrieved from Daniel K. Inouye Solar Telescope (Hawaii).

- **Chromosphere**: it is the layer above the photosphere, visibly more transparent. It is a region of rapid temperature rise. Its thickness is about 2000 km. The plasma density is much lower (around 1000 times) than in the photosphere. Given its low thickness and density, it is normally hidden from our view. However, it can be seen during an eclipse with special telescopes and satellites equipped with the proper optical filters. Its temperature is around 20.000°C.

- **Corona**: it is the Solar atmosphere's outermost layer. Its average temperature ranges from 1 to 2 million of degrees Celsius. This is a much higher temperature than the chromosphere. This thermal inversion is one of the main questions solar scientists try to explain.

Figure (1.2) shows a representation of the Sun interior and atmosphere.
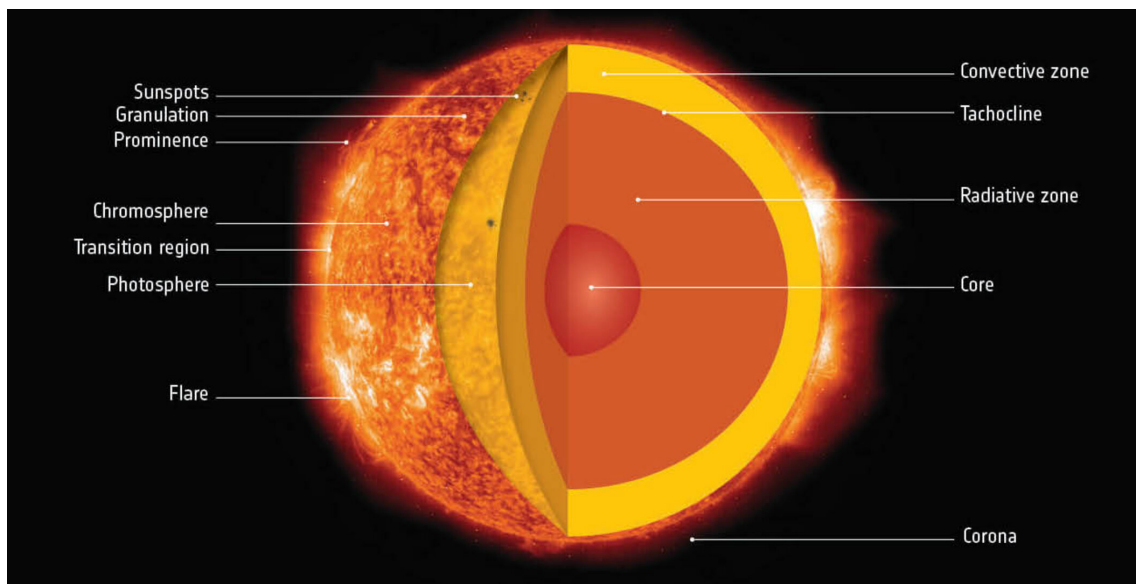
Figure 1.2: Scheme of the Sun structure.The core, radiative zone and convective zone can be distinguished. As fot the Sun's atmosphere, one can also tell apart the photosphere, chromosphere and corona. Retrieved from: https://www.esa.int/ESA_Multimedia/Images/2019/10/Anatomy_of_our_Sun.

Due to the Sun's core and it being composed of plasma, the Sun has a magnetic field. On a global scale, the Sun's magnetic field can be modeled approximately as a dipole, that is, being mainly a poloidal magnetic field. However, on local scales, the Sun's magnetic field can be highly complex. The Sun's magnetic field dynamics are governed by the interaction of the magnetohydrodynamics forces, which are detailed in section 2, with the gravitational and rotational forces. Due to the Sun's rotation, its external layers do not have the same rotational speed. The external layers from the poles to the equator lose synchronism with the rotation of the star. This asynchronism can produce an escape of Gauss force lines, producing sunspots. An increase in these can produce a Solar eruption. The magnetic field of the Sun flips, with the flip occurring when the number of sunspots is maximum. This is the so-called *Solar cycle* and its period is of around 11 years. The activity of the Sun (solar radiation, sunspots, solar flares...) exhibits a synchronized cycle following the Solar cycle.

The heliosphere is a region that extends from the Sun to the limits of the Solar System, beyond Pluto, at around 100 AU. This is the region where the Solar magnetic field has an influence. The heliosphere protects the Solar System from radiation coming from the interstellar medium.

1.2   Large scale structures

'Large scale structure' is a term used in heliophysics to refer to sufficiently large magnetic structures in the solar wind that can interact and deform Parker's spiral. These structures are caused by the Solar activity and have properties and markers recognizable at large distances in the heliosphere, as opposed to small-scale phenomena such as turbulence, magnetic reconnection...

The large scale structures can be classified in four different classes:

1. **Coronal Mass Ejections (CMEs)**: explained in detail in section 1.3.

2. **Corotating Interaction Regions (CIRs)**: they are structures formed when high-speed solar wind streams overtake slow solar wind streams as they propagate outward from the Sun. These structures produce regions of high density and magnetic field strength in the solar wind near the ecliptic plane Alves et al. (2006).

3. **Heliospheric current sheets**: it is the surface in the Solar System where the polarity of the Sun's magnetic field changes from north to south. This field extends throughout the Sun's equatorial plane in the heliosphere. This interplanetary large scale structure is caused by the rotating magnetic field of the Sun. This rotation is propagated through the heliosphere, twisting the magnetic field in a so-called *Parker spiral*, in honor of Eugene Parker, who first predicted the existence of such structure in his 1958 paper (Parker, 1958).

4. **Interplanetary shock waves**: are a type of collisionless shock, one where particles transfer energy through electromagnetic fields instead of directly bouncing into one another. These collisionless shocks are a phenomenon found throughout the universe, including in supernovae, black holes and distant stars. Interplanetary shocks start at the Sun, which continually releases streams of charged particles called the solar wind.

1.3   CMEs, ICMEs and Magnetic Clouds

Coronal Mass Ejections (CMEs) are expulsions of plasma from the corona of the Sun (its outer atmosphere) into the interplanetary medium. With the plasma, an accompanying magnetic field is released. CMEs are associated with solar flares and other forms of solar activity. A CME can contain a mass larger than 10^{13} kg and may achieve a speed of several thousand km/s. A typical CME has a mass of around 10^{11} to 10^{12} kg and has a speed between 400 and 1000 km/s (Howard, 2011).

Multiple CMEs can take place on a single day during the maximum of the Solar activity cycle. CMEs are multithermal structures, meaning they carry coronal material ($\sim$2 MK) in the front followed by cool prominence ($\sim$8000 K) material in some cases and hot flare-material ($\sim$10 MK) in others (Howard, 2011). When a CME erupts, it leaves behind hot post-eruption arcades or flare loops that mark the location of the eruption on the Sun. CMEs drive powerful interplanetary shocks, which accelerate electrons and ions. On the one hand, the accelerated electrons can produce radio bursts in the interplanetary medium. On the other hand, the protons and heavier ions accelerated by the shock near the Sun reach 1 AU in a few tens of minutes, and the shock arrives carrying locally accelerated energetic storm particles (named ESPs) (Howard, 2011).

CMEs can evolve and change substantially as time passes and travel through the heliosphere. These changes are due to the inherent nature of MHD equations (they are time-dependent) but also due to the interaction of CMEs with the solar wind and other large scale structures.

The spacecraft observations of plasma and magnetic field indicate that the structure is evolving as well as expanding Démoulin and Dasso (2009). Thus, CMEs in the interplanetary medium are called Interplaentary CMEs (ICMEs).
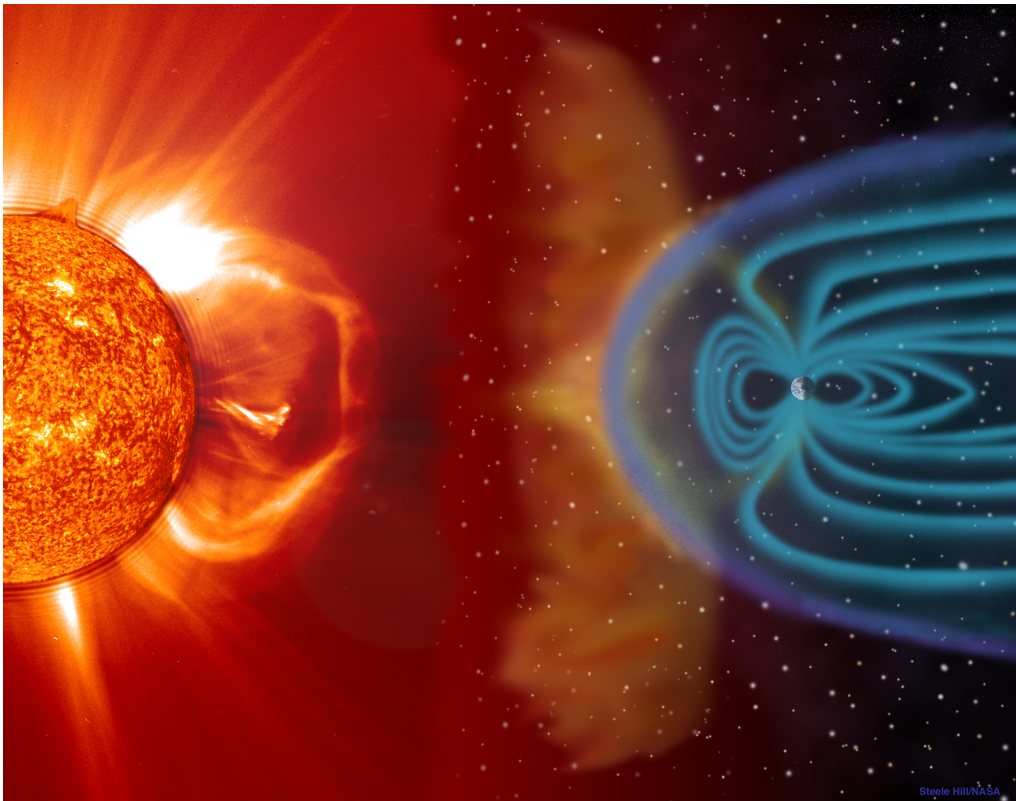
Figure 1.3: Illustration of a coronal mass ejection (CME) blast and subsequent impact at Earth. Retrieved from: https://www.esa.int/ESA_Multimedia/Images/2003/04/Coronal_mass_ejection_CME_blast_and_subsequent_impact_at_Earth.

1.4 CMEs and ICMEs Observatories

Over the years, the space science community has got increasingly interested in the study of the Sun, heliosphere, solar wind and large scale structures. This is why several missions and methods have been developed to obtain meaningful data that allow scientists to learn more about the mentioned topics.

The observations and measurements of CMEs and ICMEs can be classified into remote sensing and in-situ measurements. Most missions combine these two techniques.

1.4.1 Remote sensing observations

They use optical instruments, such as telescopes, to gain information about CMEs, sunspots, Sun's magnetic field... One of the most used remote sensing techniques is the coronagraph. Coronagraphs are designed to block out the direct light from a star's disk so that the corona structure can be resolved. Most coronagraphs are intended to view the corona of the Sun.
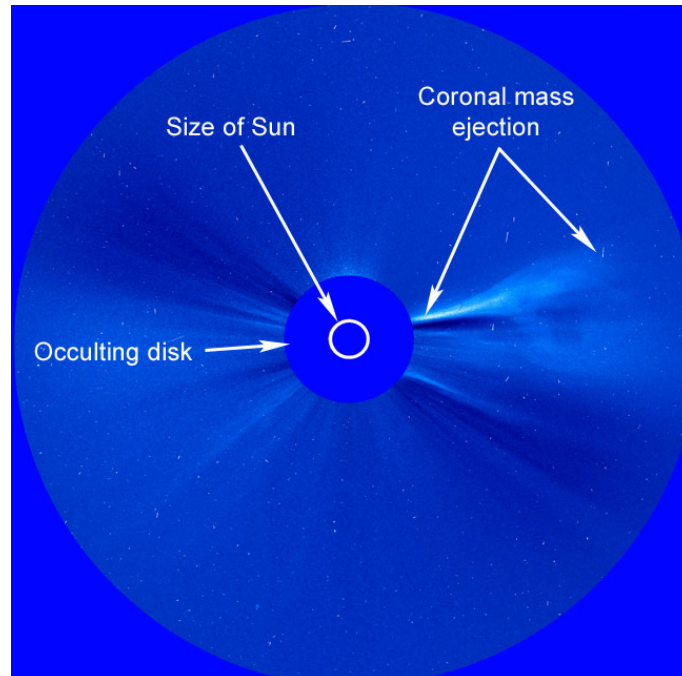
Figure 1.4: CME observed from the STEREO SECCHI's Cor2 coronagraph. Retrieved from: `https://stereo.gsfc.nasa.gov/classroom/coronagraphs.shtml`.

1.4.2 In-situ measurements

Magnetic field measurements of CMEs and ICMEs can only be made in-situ with the use of magnetometers. This is why in this work we will only be using in-situ measurements, not remote sensing. Apart from measuring magnetic fields, many other physical magnitudes can be measured such as plasma velocity, the energy of ions...

1.4.3 Spacecraft for the study of CMEs

NASA, ESA and other space agencies have designed several missions to unveil different secrets about the Sun and heliosphere. In this section we cover some of the most relevant for the study of CMEs and ICMEs.
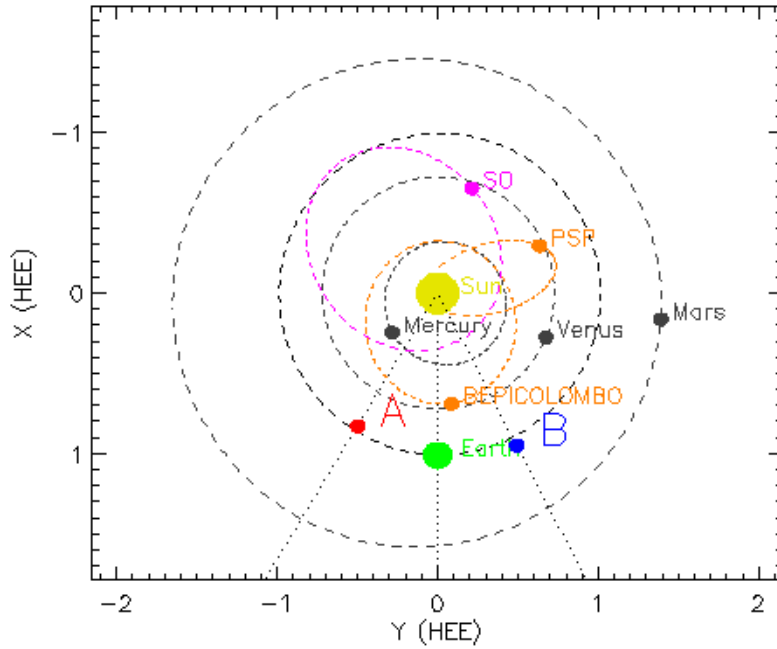
Figure 1.5: Position and orbit of the spacecrafts STEREO-A, STEREO-B, BepiColombo, Parker Solar Probe (PSP) and Solar Orbiter (SO) in the ecliptic plane of the solar system, on May 1, 2022 00:00:00 UT. Position and orbit of Mercury, Venus, Earth and Mars are also shown. Heliocentric Earth Ecliptic (HEE) coordinates are used. The axis show distances in astronomical units (AU). Image created using 'NASA's Science Center - Where is STEREO?' website: https://stereo-ssc.nascom.nasa.gov/cgi-bin/make_where_gif.

Solar TErrestial RElations Observatory (STEREO)

This mission was launched on October 25, 2006, from Cape Canaveral Air Force Station in Florida. The Solar Terrestrial Relations Observatory, (STEREO) is the third mission in NASA's Solar Terrestrial Probes Program. It has provided scientists with a unique view of the Sun-Earth system. It is composed of two nearly identical observatories, known as the *twin spacecraft*: one ahead of Earth in its orbit and the other trailing behind. They are names STEREO A and B. STEREO has traced the flow of energy and matter from the Sun to Earth. It provided the first-ever stereoscopic measurements to study the Sun and the nature of its CMEs. Mounted on each of the STEREO Spacecraft are four instrument packages:

- **SECCHI** (Sun Earth Connection Coronal and Heliospheric Investigation) has four instruments: an extreme ultraviolet imager, two white-light coronagraphs and a heliospheric imager.

- **SWAVES** (STEREO/WAVES): is an interplanetary radio burst tracker.

- **IMPACT** (In-situ Measurements of Particles and CME Transients) samples the 3D distribution and provide plasma characteristics of solar energetic particles and the local vector magnetic field.

- **PLASTIC** (PLAsma and SupraThermal Ion Composition): provides plasma characteristics of protons, alpha particles, and heavy ions.

On October 1, 2014, communications were lost with STEREO B after a planned reset of the spacecraft. All attempts to recover contact were in vain and it is thought that anomalies in the guidance and control system of the spacecraft might have rendered it powerless as a result of drift away from direct exposure of the Sun to its solar panels. STEREO-A is orbiting the Sun just inside of 1 AU, slowly catching up with Earth as it orbits around the Sun.

Solar Orbiter (SolO)

Solar Orbiter (SolO) is a mission developed by the European Space Agency (ESA) and NASA. It was launched on February 10, 2020, from Cape Canaveral Air Force Station, Florida.

It is a Sun-observing designed to obtain detailed measurements of the inner heliosphere and the nascent solar wind. It will also perform close observations of the polar regions of the Sun which is difficult to do from Earth.

Its first images were released in July 2020 and the routine science operations began in November 2021. The closest distance to the Sun is around 60 solar radii and it will go out of the ecliptic plane to reach latitudes up to $33°$. This is enabling SolO to take the closest-ever images of the Sun, the first-ever close-up images of the Sun's polar regions, measuring the composition of the solar wind and linking it to its area of origin on the Sun's surface.

It is equipped with 6 remote sensing and 4 in-situ instruments. The 4 instruments that take in-situ measurements are EPD (Energetic Particle Detector), MAG (magnetometer), SWA (Solar Wind Analyzer Suite) and RPW (Radio and Plasma Waves).
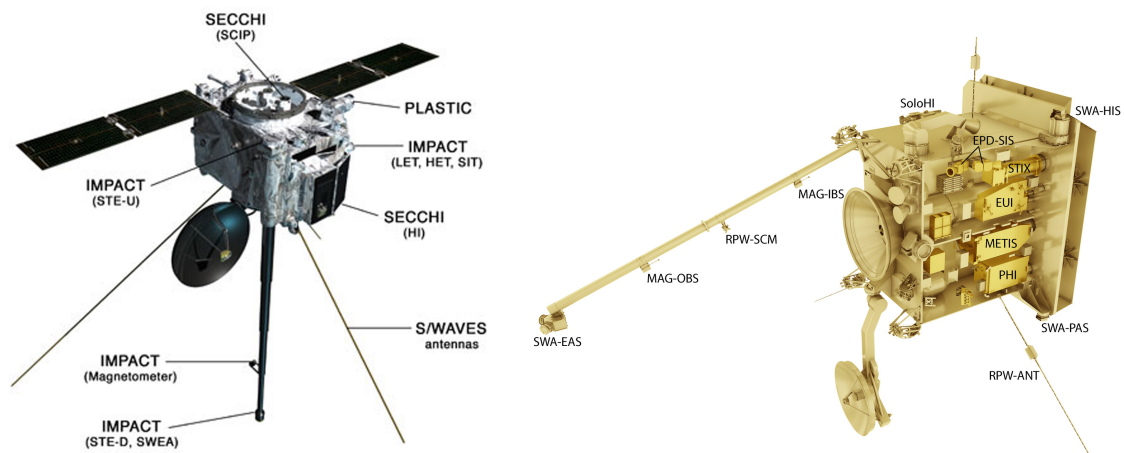
Figure 1.6: STEREO (left) and Solar Orbiter (right) spacecrafts and their corresponding instrument suites. Retrieved from: https://www.nasa.gov/mission_pages/stereo/spacecraft/index.html and https://www.esa.int/Space_in_Member_States/Spain/Los_instrumentos_de_Solar_Orbiter, respectively.

Parker Solar Probe (PSP)

Parker Solar Probe (PSP) is a NASA mission launched on August 12, 2018, from Cape Canaveral Air Force Station, Florida.

This mission aims to study the Sun's atmosphere, and it is doing it by gradually bringing its orbit closer to the Sun using Venus' gravity during seven flybys over nearly seven years. It will get as to the Sun's surface as 8.86 solar radii (Garner, 2021).

Flying into Sun's corona (the outermost part of the Sun's atmosphere) for the first time, PSP employs a combination of in situ measurements and imaging with the aim of deepening our knowledge and understanding of the corona and the origin and evolution of the solar wind.

PSP is equipped with the following instrumentation:

- **FIELDS** (The Electromagnetic Fields Investigation): makes direct measurements of electric and magnetic fields, radio waves, Poynting flux, absolute plasma density, and electron temperature. It consists of two flux-gate magnetometers, a search-coil magnetometer, and 5 plasma voltage sensors.

- **SWEAP** (Solar Wind Electrons Alphas and Protons): counts the electrons, protons and helium ions, and measures their properties such as velocity, density, and temperature.

- **WISPR** (Wide-field Imager for Solar Probe): optical telescopes that acquire images of the corona and inner heliosphere.

- **IS⊙IS** (Integrated Science Investigation of the Sun): measure energetic electrons, protons and heavy ions.
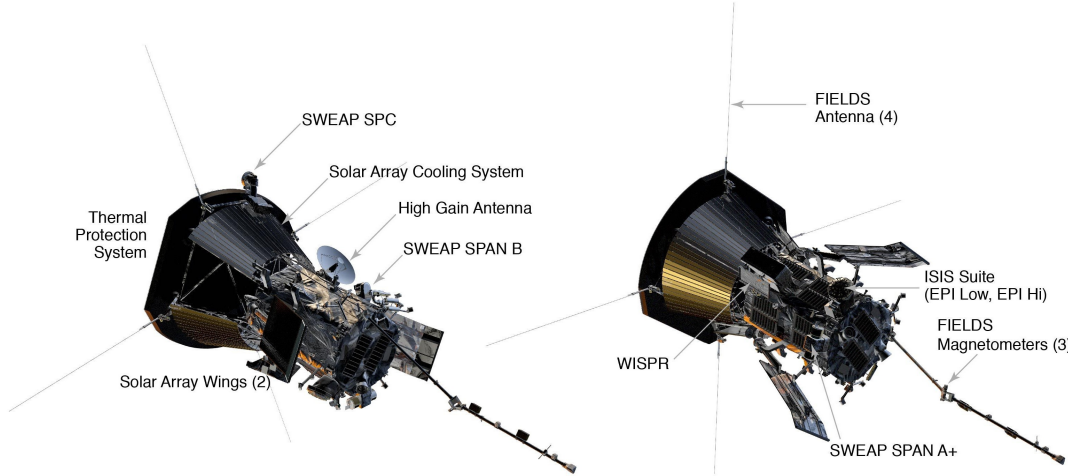
Figure 1.7: Two views of the Parker Solar Probe spacecraft and its instrument suite.

1.4.4 Heliospheric coordinate systems

The position of spacecraft in the heliosphere is measured with heliospheric coordinate systems. In this section we present two of the most used systems: RTN and GSE.

- **Radial Tangential Normal (RTN)**: this is a spacecraft-centered coordinate system. The R axis points from the Sun's center to the spacecraft, the T axis points in the direction of the cross product of the solar rotational axis $\boldsymbol{\omega}$ and R, and lies in the solar equatorial plane and the N axis completes the orthonormal triad.

$$\hat{\boldsymbol{e}}_{\boldsymbol{R}} = \hat{\boldsymbol{r}} \tag{1.1}$$

$$\hat{\boldsymbol{e}}_{\boldsymbol{T}} = \frac{\boldsymbol{\omega} \times \hat{\boldsymbol{r}}}{\|\boldsymbol{\omega} \times \hat{\boldsymbol{r}}\|} \tag{1.2}$$

$$\hat{\boldsymbol{e}}_{\boldsymbol{N}} = \hat{\boldsymbol{e}}_{\boldsymbol{R}} \times \hat{\boldsymbol{e}}_{\boldsymbol{T}} \tag{1.3}$$

- **Geocentric Solar Ecliptic System (GSE)**: this is an Earth-centered coordinate system. The $\hat{\boldsymbol{e}}_{\boldsymbol{x}}$ points from the center of Earth to Solar center. The $\hat{\boldsymbol{e}}_{\boldsymbol{z}}$ points to the north ecliptic pole and $\hat{\boldsymbol{e}}_{\boldsymbol{y}}$ completes the orthonormal triad.
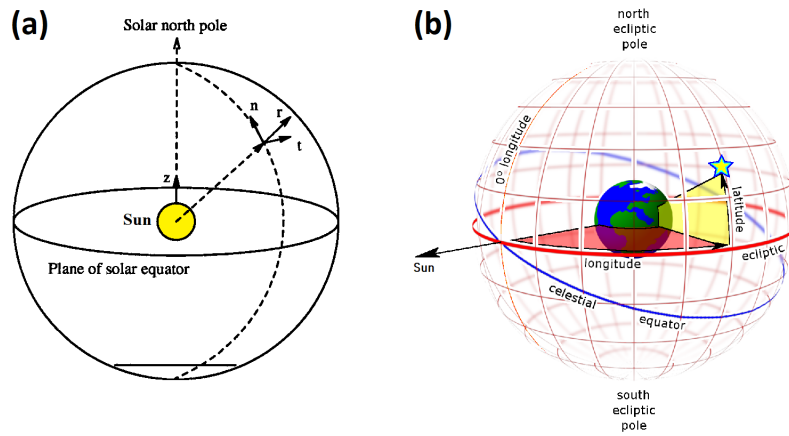
Figure 1.8: (Left) Representation of the RTN coordinate system. Retrieved from: (Villanueva, 1994). (Right) Representation of the GSE coordinate system. Retrieved from: `en.wikipedia.org/wiki/Ecliptic_coordinate_system`

2 . Fundamentals of magnetohydrodynamics (MHD)

Magnetohydrodynamics (MHD), also known as magnetofluid dynamics or hydromagnetics, is the study of the dynamics of electrically conducting fluids. Examples of such fluids include plasmas, liquid metals, and molten salts or electrolytes (Mohsen Sheikholeslami, 2018).

The fundamental concept behind MHD is that magnetic fields can induce currents in a moving conductive fluid, which in turn creates forces on the fluid and changes the magnetic field itself (Mohsen Sheikholeslami, 2018). Therefore, there is a coupling between the fluid motion and the magnetic field (Goedbloed and Poedts, 2004). To describe MHD, Maxwell's equations for electromagnetism are combined with Navier-Stokes equations for fluid dynamics.

The scope of MHD is very diverse: it can be applied to natural phenomena in fields such as astrophysics, planetary and solar physics and geophysics: the magnetism of the Earth and other planets, that of the Sun and other stars. Magnetohydrodynamics is key in astrophysical processes such as magneto-convection, magnetic flux emergence, flux ropes, spots, atmospheric heating, wind acceleration, flares, and eruptions (Daniel et al., 2021).

MHD also has multiple technological applications, which had a great impact on society: energy generation, levitation, processing of materials, energy storage and flow measurement (Goedbloed and Poedts, 2004). Another important technological application is nuclear reactors.

2.1 Fundamental MHD equations

Below we list the fundamental MHD equations. Note that, although gravity plays a prominent role in many fluid processes, the kinetic phenomena to which this analysis applies occur sufficiently far from planets or stars, rendering the effects of gravity negligible. gravity. This assumption is not true near the Sun (Massimo Materassi and Anthea J. Coster, 2020)) and gravity should be taken into account. During the course of this work, however, we will neglect any effect caused by gravity.

The fluid dynamics equations for an incompressible Newtonian fluid are:

$$\boldsymbol{\nabla} \cdot \boldsymbol{v} = 0 \qquad \text{(Mass conservation. Continuity eq.)}$$

$$\rho \left(\frac{\partial \boldsymbol{v}}{\partial t} + (\boldsymbol{v} \cdot \boldsymbol{\nabla}) \boldsymbol{v} \right) = -\boldsymbol{\nabla} p + \boldsymbol{j} \times \boldsymbol{B} + -\rho \boldsymbol{g} \quad \text{(Momentum balance. Navier-Stokes eq.)}$$

$$\rho c \left(\frac{\partial T}{\partial t} + (\boldsymbol{v} \cdot \boldsymbol{\nabla}) T \right) = k \boldsymbol{\nabla}^2 T + \Phi \qquad \text{(Energy conservation. Heat transfer eq.)}$$

$$(2.1)$$

$$(2.2)$$

$$(2.3)$$

Maxwell's equation in differential form are the following:

$$
\begin{aligned}
\boldsymbol{\nabla} \cdot \boldsymbol{E} &= \frac{\rho}{\epsilon_0} & \text{(Gauss's law for electricity)} & \quad (2.4) \\
\boldsymbol{\nabla} \cdot \boldsymbol{B} &= 0 & \text{(Gauss' law for magnetism)} & \quad (2.5) \\
\boldsymbol{\nabla} \times \boldsymbol{E} &= -\frac{\partial \boldsymbol{B}}{\partial t} & \text{(Faraday's law)} & \quad (2.6) \\
\boldsymbol{\nabla} \times \boldsymbol{B} &= \mu_0 \boldsymbol{j} + \mu_0 \epsilon \frac{\partial \boldsymbol{E}}{\partial t} & \text{(Ampère-Maxwell's law)} & \quad (2.7)
\end{aligned}
$$

Additional electromagnetic equations are:

$$
\begin{aligned}
\boldsymbol{F} &= q(\boldsymbol{E} + \boldsymbol{v} \times \boldsymbol{B}) & \text{(Lorentz force for a moving charge)} & \quad (2.8) \\
\boldsymbol{j} &= \sigma(\boldsymbol{E} + \boldsymbol{v} \times \boldsymbol{B}) & \text{(Ohm's law)} & \quad (2.9) \\
\boldsymbol{\nabla} \cdot \boldsymbol{j} + \frac{\partial \rho}{\partial t} &= 0 & \text{(Charge conservation)} & \quad (2.10)
\end{aligned}
$$

The combination of the above mentioned equations form the so-called MHD equations.

2.2 Ideal MHD

MHD equation are very complex. To simplify them, several assumptions are made. The resulting equations are named *Ideal MHD equations*:

1. Non-relativistic flows: $\|\boldsymbol{v}\| \ll c$, that is, the velocity of plasma is non-relativistic.

2. Low frequency phenomena: electromagnetic wave propagation is not considered.

3. Electric fields are of the order of induced effects (EMF): $\|\boldsymbol{E}\| \sim \|\boldsymbol{v} \times \boldsymbol{B}\|$

To simplify the MHD equations, we compare the order of magnitude of different terms in the electromagnetic equations. Let us assume the following characteristic scales:

$$
\text{Time: } \tau \qquad \text{Length: } L \qquad \text{Velocity: } V \sim \frac{L}{\tau} \qquad \text{Magnetic field: } B \qquad \text{Electric field: } E \sim VB
$$

$$(2.11)$$

We can make approximations in the following equations:

1. *Amperè-Maxwell's law*: Maxwell's displacement current is negligible. We calculate the quotient of the Maxwell's displacement current $\mu_0 \epsilon \frac{\partial \boldsymbol{E}}{\partial t}$ to the curl of $\boldsymbol{B}$ in Ampère-Maxwell's law (2.7).

$$
\frac{\mu_0 \epsilon \|\frac{\partial \boldsymbol{E}}{\partial t}\|}{\|\boldsymbol{\nabla} \times \boldsymbol{B}\|} \sim \frac{\mu_0 \epsilon V B/\tau}{B/L} \sim \frac{V^2}{c^2} \ll 1 \qquad (2.12)
$$

Therefore, under the previously mentioned conditions, we can neglect the second term in (2.7) and it simply becomes $\boldsymbol{\nabla} \times \boldsymbol{B} = \mu_0 \boldsymbol{j}$.

2. **The time variation of charge density ρ is negligible**.

From Gauss' law for electricity we find:

$$\rho \sim \epsilon \left| \boldsymbol{\nabla} \cdot \boldsymbol{E} \right| \sim \epsilon \frac{E}{L} \tag{2.13}$$

Similarly, from the simplified Ampère-Maxwell law we get:

$$\|\boldsymbol{j}\| = \frac{\|\boldsymbol{\nabla} \times \boldsymbol{B}\|}{\mu_0} \sim \frac{B}{\mu_0 L} \tag{2.14}$$

We can use the previous two approximations in order to compare the two terms of the charge conservation equation (2.10):

$$\frac{\left| \frac{\partial \rho}{\partial t} \right|}{\left| \boldsymbol{\nabla} \cdot \boldsymbol{j} \right|} \sim \frac{\epsilon E / L \tau}{B / \mu_0 L} \sim \frac{V^2}{c^2} \ll 1 \tag{2.15}$$

Therefore, under the previously mentioned conditions, we can neglect the second term in (2.10) and it becomes $\boldsymbol{\nabla} \times \boldsymbol{j} = 0$.

3. **Lorentz force**: the electric contribution of the Lorentz force is negligible.

$$\frac{\rho \|\boldsymbol{E}\|}{\|\boldsymbol{j} \times \boldsymbol{B}\|} \sim \frac{\epsilon V^2 / L}{B^2 / \mu_0 L} \sim \frac{V^2}{c^2} \ll 1 \tag{2.16}$$

We can then rewrite the electromagnetic equations in a reduced form:

$$\begin{aligned}
\boldsymbol{\nabla} \cdot \boldsymbol{E} &= \frac{\rho}{\epsilon_0} & \text{(Gauss's law for electricity)} & \quad (2.17) \\
\boldsymbol{\nabla} \cdot \boldsymbol{B} &= 0 & \text{(Gauss' law for magnetism)} & \quad (2.18) \\
\boldsymbol{\nabla} \times \boldsymbol{E} &= -\frac{\partial \boldsymbol{B}}{\partial t} & \text{(Faraday's law)} & \quad (2.19) \\
\boldsymbol{\nabla} \times \boldsymbol{B} &= \mu_0 \boldsymbol{j} & \text{(Reduced Ampère-Maxwell's law)} & \quad (2.20)
\end{aligned}$$

The additional electromagnetic equations become:

$$\begin{aligned}
\boldsymbol{F} &= \boldsymbol{j} \times \boldsymbol{B} & \text{(Reduced Lorentz force)} & \quad (2.21) \\
\boldsymbol{j} &= \sigma(\boldsymbol{E} + \boldsymbol{v} \times \boldsymbol{B}) & \text{(Ohm's law)} & \quad (2.22) \\
\boldsymbol{\nabla} \cdot \boldsymbol{j} &= 0 & \text{(Reduced Charge conservation)} & \quad (2.23)
\end{aligned}$$

Let us now combine some of the ideal MHD equations

2.2.1 The induction equation

By combining Faraday's law and Ohm's law:

$$\frac{\partial \boldsymbol{B}}{\partial t} = -\boldsymbol{\nabla} \times \boldsymbol{E} = -\boldsymbol{\nabla} \times \left(\frac{\boldsymbol{j}}{\sigma} - \boldsymbol{v} \times \boldsymbol{B} \right) = \boldsymbol{\nabla} \times (\boldsymbol{v} \times \boldsymbol{B}) - \frac{1}{\sigma} \boldsymbol{\nabla} \times \boldsymbol{j} \tag{2.24}$$

The last term can be rewritten using Ampère-Maxwell's law and the identity $\boldsymbol{\nabla} \times (\boldsymbol{\nabla} \times \boldsymbol{B}) = \boldsymbol{\nabla}(\boldsymbol{\nabla} \cdot \boldsymbol{B}) - \boldsymbol{\nabla}^2 \boldsymbol{B}$ together with Gauss' law for magnetism ($\boldsymbol{\nabla} \cdot \boldsymbol{B} = 0$) we get the induction equation for the magnetic field:

$$\frac{\partial \boldsymbol{B}}{\partial t} = \underbrace{\boldsymbol{\nabla} \times (\boldsymbol{v} \times \boldsymbol{B})}_{\text{Advection}} + \underbrace{\gamma \boldsymbol{\nabla}^2 \boldsymbol{B}}_{\text{Diffusion}} \tag{2.25}$$

where $\gamma = \frac{1}{\mu_0 \sigma}$ is the so-called *magnetic diffusivity*.

Similarly as before, we can compute the ratio of the diffusion and advective terms of equation (2.25).

$$\frac{|\boldsymbol{\nabla} \times (\boldsymbol{v} \times \boldsymbol{B})|}{|\gamma \boldsymbol{\nabla}^2 \boldsymbol{B}|} \sim \frac{VB/L}{\gamma B/L^2} = \frac{LV}{\gamma} \tag{2.26}$$

Motivated by the previous equation, we define the *magnetic Reynolds number* as:

$$R_m = \frac{LV}{\gamma} = \mu_0 \sigma L V \tag{2.27}$$

The magnetic Reynolds number is a dimensionless parameter. We can distinguish between two limits depending on the its value:

- **Ideal limit** ($R_m \gg 1$): convective transport dominates (dragging of field lines). We can neglect the advection term in equation (2.25) and the induction equation becomes:

$$\frac{\partial \boldsymbol{B}}{\partial t} = \boldsymbol{\nabla} \times (\boldsymbol{v} \times \boldsymbol{B}) \tag{2.28}$$

- **Diffusive limit** ($R_m \ll 1$): diffusive transport dominates (flow braking). We can neglect the convection term in equation (2.25) and the induction equation becomes:

$$\frac{\partial \boldsymbol{B}}{\partial t} = \gamma \boldsymbol{\nabla}^2 \boldsymbol{B} \tag{2.29}$$

2.2.2 Magnetic pressure and tension

Let us now introduce the concepts of magnetic pressure and tension. These concepts play an important role in the behavior of magnetic field lines.

Lorentz force can be expressed using Ampère's law as:

$$\boldsymbol{j} \times \boldsymbol{B} = \left(\boldsymbol{\nabla} \times \frac{\boldsymbol{B}}{\mu_0} \right) \times \boldsymbol{B} = -\boldsymbol{\nabla} \underbrace{\left(\frac{\|B\|^2}{2\mu_0} \right)}_{\text{Magnetic pressure}} + \underbrace{\frac{1}{\mu_0} \boldsymbol{B} \cdot \boldsymbol{\nabla} \boldsymbol{B}}_{\text{Magnetic tension}} \tag{2.30}$$

The first term corresponds to the gradient of magnetic pressure, $p_B = \frac{\|B\|^2}{2\mu_0}$. This term is irrotational. The second term corresponds to the so-called magnetic tension. It is rotational and can be further decomposed into its tangential and normal components:

$$\frac{1}{\mu_0} \boldsymbol{B} \cdot \boldsymbol{\nabla} \boldsymbol{B} = \frac{\partial}{\partial s} \left(\frac{\|B\|^2}{2\mu_0} \right) \hat{\boldsymbol{e}}_{\boldsymbol{t}} - \frac{\|B\|^2}{\mu_0 R} \hat{\boldsymbol{e}}_{\boldsymbol{n}} \tag{2.31}$$

Magnetic field lines can be visualized as being in tension, exerting a force on the fluid, as shown in figure (2.1). Magnetic pressure tends to stretch the field lines whereas magnetic tension tends to compensate for their curvature.
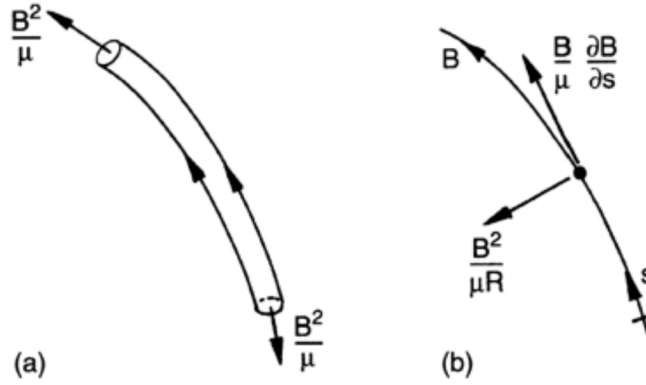
Figure 2.1: Representation of magnetic pressure and tension in a magnetic field line. Retrieved from: (Davidson, 2017)

The *gas pressure* of plasma is defined in terms the density and temperature of the particles composing it:

$$p = \sum_j n_j k_B T_k \tag{2.32}$$

Where j runs through all the different sorts of particles that compose the plasma. This pressure may vary throughout the plasma as the density of particles and their temperatures may not be homogeneous.

A very important magnitude for plasmas, derived from the hydrostatic and magnetic pressures, is the so-called *beta* parameter of a plasma. It is defined as the ratio of plasma thermal pressure to the magnetic pressure:

$$\beta = \frac{p}{p_B} = \frac{p}{\|B\|^2 / 2\mu_0} \tag{2.33}$$

The large scale structures in the heliosphere are complex plasma in which magnetic and plasma pressure play interchanging roles for dominance. The dominating force is described by the plasma β (Gary, 2001). A large plasma beta indicates that hydrostatic forces are greater than magnetic forces whereas a low beta parameter indicates the opposite.

2.2.3   Magnetic helicity

We now introduce the concept of helicity. This is a term originally defined in fluid dynamics, which has a magnetic counterpart. In fluid dynamics, *hydrodynamical helicity* is a magnitude whose topological interpretation is to measure of linkage and/or knottedness of vortex lines in the flow. Given a close volume V, it is defined as:

$$H_{\text{hydro}} = \int_V \boldsymbol{v} \cdot (\boldsymbol{\nabla} \times \boldsymbol{v}) \, dV \tag{2.34}$$

where v is the velocity of the fluid. In a similar manner, we the *magnetic helicity* of a magnetic configuration can be defined as:

$$H = \int_V \boldsymbol{A} \cdot (\boldsymbol{\nabla} \times \boldsymbol{A}) \, dV = \int_V \boldsymbol{A} \cdot \boldsymbol{B} \, dV \tag{2.35}$$

However, if the volume V is not magnetically closed, that is, and the magnetic field lines enter or exit the volume, the magnetic helicity is not gauge invariant. This means that if we change $\boldsymbol{A}$ by $\boldsymbol{A} + \boldsymbol{\nabla}\Phi_A$ (where Φ_A is a generic function), the magnetic helicity changes. This fact motivates the definition of a new but related magnitude called *relative magnetic helicity* H_r. The relative magnetic helicity is gauge invariant even if the volume is not magnetically closed. This definition was proposed by (Berger and Field, 1984). The expression for the relative magnetic helicity is:

$$H_r = \int_V (\boldsymbol{A} \cdot \boldsymbol{B} - \boldsymbol{A_0} \cdot \boldsymbol{B_0}) \, dV \tag{2.36}$$

where $\boldsymbol{B_0} = \boldsymbol{\nabla} \times \boldsymbol{A_0}$ and satisfies $\boldsymbol{B_0} \cdot \hat{\boldsymbol{n}} = \boldsymbol{B} \cdot \hat{\boldsymbol{n}}$ on the surface S that encloses the volume V. Similarly, $\boldsymbol{A_0}$ is defined by imposing $\boldsymbol{A_0} \times \hat{\boldsymbol{n}} = \boldsymbol{A} \times \hat{\boldsymbol{n}}$ on S. It is thought that the relative magnetic helicity is an important magnitude for the study of expanding MFRs since it is a conserved magnitude.

2.3   Ideal MHD equilibrium

Ideal MHD equilibrium conditions assume ideal MHD and equilibrium, that is, there is no variation in time of the fields (time independence, $\frac{\partial}{\partial t} = 0$).

$$
\begin{aligned}
\boldsymbol{\nabla} \cdot \boldsymbol{E} &= \frac{\rho}{\epsilon} && \text{(Gauss's law for electricity)} & (2.37)\\
\boldsymbol{\nabla} \cdot \boldsymbol{B} &= 0 && \text{(Gauss' lar for magnetism)} & (2.38)\\
\boldsymbol{\nabla} \times \boldsymbol{E} &= 0 && \text{(Faraday's law)} & (2.39)\\
\boldsymbol{\nabla} \times \boldsymbol{B} &= \mu_0 \boldsymbol{j} && \text{(Ampère-Maxwell's law)} & (2.40)
\end{aligned}
$$

The plasma velocities are then constant and the force equation (Navier-Stokes) becomes:

$$\rho\left(\cancelto{0}{\frac{\partial \boldsymbol{v}}{\partial t} + (\boldsymbol{v} \cdot \boldsymbol{\nabla})\boldsymbol{v}}\right) = -\boldsymbol{\nabla}p + \boldsymbol{j} \times \boldsymbol{B} + \cancelto{0}{-\rho \boldsymbol{g}} \implies \boldsymbol{\nabla}p = \boldsymbol{j} \times \boldsymbol{B} \tag{2.41}$$

We will call this equation the *momentum equation for plasma in equilibrium.*

3. Magnetic Flux Rope (MFR) models

Magnetic Flux Ropes (MFRs) are magnetic structures that confine the plasma. They have a topology that reminds of a rope, thus its name. MFRs can be found in all the structures mentioned before. They are usually found in CMEs and ICMEs. This is the reason why the focus of this work is on this kind of large scale structures.

In the MFR found within the ICMEs, there are some features in the physical qualities that characterize the structures. These are called MFR signatures:

1. Increment in the magnitude of the magnetic field.

2. Rotation in the magnetic field direction.

3. Decrease in the bulk speed (expanding MFR).

4. Proton temperature drops.

5. Increase in the pressure and low plasma β (the definition of which can be found in section 2.2.2).

At least three of these signatures should simultaneously appear to define an ICME and signatures 1, 2 and 3 to indicate the MFR within the ICME.

Figure 3.1 displays measurements from NASA's WIND mission between March 19 and March 21, 2001. It shows the three components of the magnetic field as well as its magnitude, the plasma speed v_p, the proton's density N_p and the proton's temperature T_p. The plasma beta parameter and transverse pressure are also shown. The magnetic obstacle is measured between the 'b' and 'c' temporal tags (vertical dashed lines). One can see an increment of the magnetic field magnitude (from around 15 nT to 20 nT), corresponding to signature 1. A change of sign in the y and z components of $\boldsymbol{B}$ is also observed, corresponding to a magnetic field rotation (signature 2). The plasma speed v_p decreases from around 475 km/s to around 300 km/s (signature 3). The proton's temperature decreases during the magnetic obstacle (notice logarithmic scale is used), corresponding to signature 4. Finally, the beta parameter is low throughout the magnetic obstacle ($\beta < 1$), corresponding to signature 5.
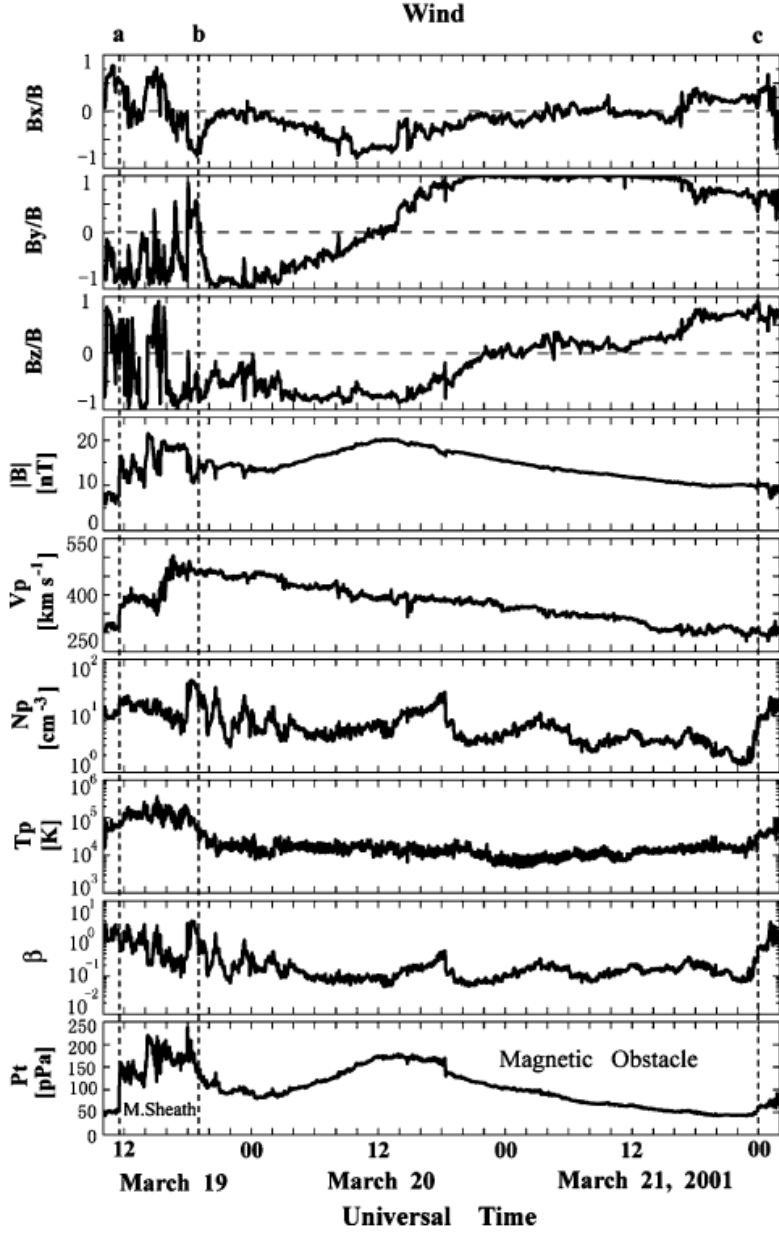
Figure 3.1: WIND measurements from March 19 to March 21, 2001. The measurements include magnetic field, plasma velocity, density and temperature as well as proton beta and transverse pressure observations. Retrieved from: (Jian et al., 2006)

MFRs can be modeled in various manners. The approach we take in this work is one of the most extended ones, which assumes that the axis of the rope is straight (see figure 3.2). This turns out to be good approximation for ICMEs, which have grown in time and whose axis curvature is then small. Under this consideration, it is assumed that magnitudes do not vary in the direction of the flux-rope axis.
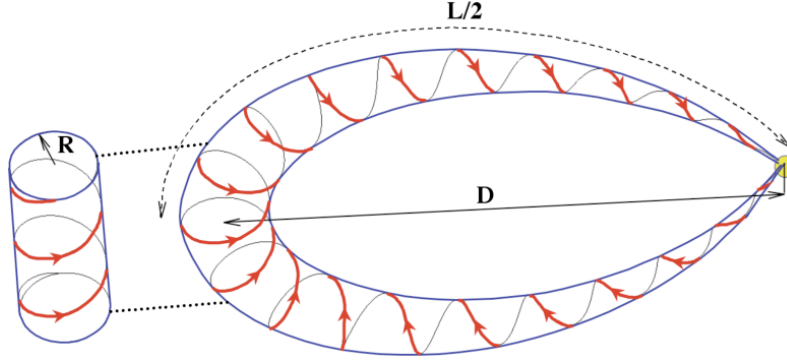
Figure 3.2: Scheme of an ICME, with its ends attached to the Sun (in yellow, at the right). Retrieved from: (Démoulin and Dasso, 2009)

In this work, we will encounter many situations where geometry and symmetry play a very important role. This is why we define the following three geometries:

- **Cylindrical geometry**: no dependencies on one of the axis (we choose it to be the z axis), that is $\frac{\partial}{\partial z} = 0$. It can be also called planar geometry.

- **Circular geometry**: no dependencies on the poloidal angle φ in cylindrical coordinates.

- **Elliptical geometry**: after scaling of one of the axis we obtain circular geometry.

Derived from these geometries we have circular-cylindrical and elliptical-cylindrical symmetries, which are going to be the ones used to describe MFRs.

3.1 Circular-cylindrical symmetric models for MFRs

Given the shape of a MFR, circular-cylindrical symmetry is usually used to model them. These models cannot account for any distortion in the flux-rope cross-section, but still, usually give good results.

3.1.1 Coordinates and operators

We will use standard cylindrical coordinates (r, φ, z), with $r \in (0, \infty)$, $\varphi \in [0, 2\pi)$ and $z \in (-\infty, \infty)$, whose relation with Cartesian coordinates is:

$$x_c = r \cos \varphi, \quad y_c = r \sin \varphi, \quad z_c = z \tag{3.1}$$

The unit vectors of the corresponding orthonormal basis are:

$$\begin{cases} \hat{\boldsymbol{e}}_{\boldsymbol{r}} &= \cos \varphi \hat{\boldsymbol{u}}_{\boldsymbol{x}} + \sin \varphi \hat{\boldsymbol{u}}_{\boldsymbol{y}} \\ \hat{\boldsymbol{e}}_{\boldsymbol{\varphi}} &= -\sin \varphi \hat{\boldsymbol{u}}_{\boldsymbol{x}} + \cos \varphi \hat{\boldsymbol{u}}_{\boldsymbol{y}} \\ \hat{\boldsymbol{e}}_{\boldsymbol{z}} &= \hat{\boldsymbol{u}}_{\boldsymbol{z}} \end{cases} \tag{3.2}$$

From the expression of the divergence and curl in cylindrical coordinates we can apply the circular-cylindrical symmetry to simplify it, resulting in:

$$\boldsymbol{\nabla} \cdot \boldsymbol{A} = \frac{1}{r}\frac{\partial(rA_r)}{\partial r} + \frac{1}{r}\frac{\partial A_\varphi}{\partial \varphi}^{\,0} + \frac{\partial A_z}{\partial z}^{\,0} = \frac{1}{r}\frac{\partial(rA_r)}{\partial r} \tag{3.3}$$

Similarly, the curl operator is:

$$\boldsymbol{\nabla} \times \boldsymbol{A} = \left(\frac{1}{r}\frac{\partial A_z}{\partial \varphi}^{\,0} - \frac{\partial A_\varphi}{\partial z}^{\,0}, \frac{\partial A_r}{\partial z}^{\,0} - \frac{\partial A_z}{\partial r}, \frac{1}{r}\frac{\partial(rA_\varphi)}{\partial r} - \frac{\partial A_r}{\partial \varphi}^{\,0} \right) = \left(0, -\frac{\partial A_z}{\partial r}, \frac{1}{r}\frac{\partial(rA_\varphi)}{\partial r} \right)$$

$$\tag{3.4}$$

Both the divergence and curl operators are important since they appear in Maxwell's equations.

3.1.2 General equations

The magnetic field has to fulfill Gauss' law for magnetism, which in cylindrical coordinates takes the following form:

$$\boldsymbol{\nabla} \cdot \boldsymbol{B} = \frac{1}{r}\frac{\partial(rB_r)}{\partial r} = 0 \tag{3.5}$$

The solutions of such differential equation are of the form $B_r(r) = \frac{C}{r}$ with $C \in \mathbb{R}$. As we want the magnetic field to be well defined for $r \to 0$, it is necessary that $C = 0$, leading to $B_r(r) = 0$. This is a general result: for circular-cylindrical flux ropes, the magnetic field does not have a radial component. Therefore the expression for the magnetic field is:

$$\boldsymbol{B}(r) = (0, B_\varphi(r), B_z(r)) \tag{3.6}$$

which only has poloidal and axial components.

Imposing now Ampère-Maxwell's law leads to a relation between the current density and magnetic field components:

$$\boldsymbol{j} = (j_r, j_\varphi, j_z) = \frac{1}{\mu_0}\boldsymbol{\nabla} \times \boldsymbol{B} = \frac{1}{\mu_0}\left(0, -\frac{\partial B_z}{\partial r}, \frac{1}{r}\frac{\partial(rB_\varphi)}{\partial r} \right) \tag{3.7}$$

The components of the current density $\boldsymbol{j}$ can be directly determined from the previous equation:

$$
\begin{cases}
j_r = 0 \\
j_\varphi = -\dfrac{1}{\mu_0}\dfrac{\partial B_z}{\partial r} \\
j_z = \dfrac{1}{\mu_0 r}\dfrac{\partial (r B_\varphi)}{\partial r}
\end{cases}
\tag{3.8}
$$

Note that the radial current density is also zero in the circular-cylindrical configuration. Integrating the previous equations in the radial component from 0 to r leads to an expression of the components of the magnetic field in terms of the current density.

$$
\begin{cases}
B_r = 0 \\
B_\varphi = \dfrac{\cancel{B_\varphi^0}^{\,0}}{r} + \dfrac{\mu_0}{r}\displaystyle\int_0^r r' j_z(r')\,\mathrm{d}r' \\
B_z = B_z^0 - \mu_0 \displaystyle\int_0^r j_\varphi(r')\,\mathrm{d}r'
\end{cases}
\tag{3.9}
$$

As we want the magnetic field not to diverge for $r \to 0$ we need $B_\varphi^0 = 0$.

With the previous equations, we can calculate the magnetic field generated from a given current density.

Similarly, from the magnetic field $\boldsymbol{B}$ we can calculate the magnetic potential $\boldsymbol{A}$ from $\boldsymbol{B} = \boldsymbol{\nabla} \times \boldsymbol{A}$, which leads to:

$$
\begin{cases}
A_r = 0 \\
A_\varphi(r) = \dfrac{1}{r}\displaystyle\int_0^r r' B_z(r')\,dr' \\
A_z(r) = -\displaystyle\int_0^r B_\varphi(r')\,dr'
\end{cases}
\tag{3.10}
$$

The relative magnetic helicity, defined in section 2.2.3, of a circular-cylindrical MFR is given by the following expression, derived by S. Dasso (2003).

$$
\frac{H_r}{L} = 4\pi \int_0^R A_\varphi B_\varphi r\,dr.
\tag{3.11}
$$

In flux ropes, magnetic lines tend to turn around the axis in a helix-like manner. The pitch is the axial distance it takes for a magnetic field line to complete a complete helix turn. A related magnitude is the twist or twist angle. We define the *total twist angle* (Φ) of a field line as the angle turned around an axis. For the circular-cylindrical geometry we are studying in this section, the twist of a magnetic field line going from one end to the other of a MFR with length L is given by:

$$
\Phi(r) = \frac{L B_\varphi(r)}{r B_z(r)}
\tag{3.12}
$$

The above expression is easily interpreted when unfolding the flux rope, as shown in the following figure.
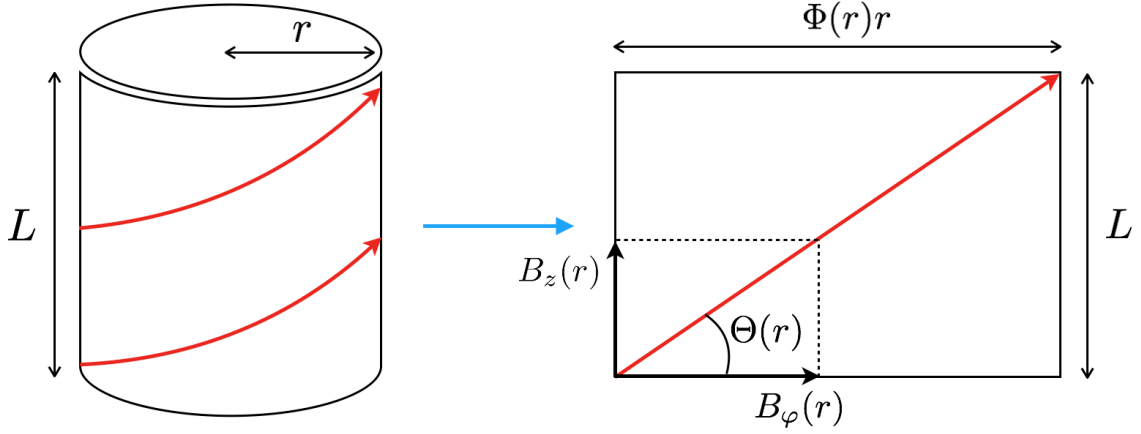
Figure 3.3: Scheme of a circular-cylindrical MFR magnetic field lines and twist. Retrieved from: (Florido-Llinàs, 2020).

The number of turns done by a magnetic field line around the MFR axis is thus given by: $N = \frac{\Phi}{2\pi}$. Finally, the *twist* (Q) of a MFR is defined as the total twist angle per unit length:

$$Q(r) = \frac{\Phi(r)}{L} = \frac{B_\varphi(r)}{r B_z(r)} \qquad (3.13)$$

The twist is a magnitude thought to be related to the stability of the MFR.

3.1.3 Force-free models

Force-free (FF) models are those in which the Lorentz force vanishes throughout the MFR, that is, $\boldsymbol{j} \times \boldsymbol{B} = \boldsymbol{0}$. From the properties of the cross product, this means that the current density and magnetic field are collinear at every point of space, that is, $\exists \alpha(r)$ such that $\mu_0 \boldsymbol{j} = \alpha(r)\boldsymbol{B}$. Therefore, Ampère's law becomes:

$$\boldsymbol{\nabla} \times \boldsymbol{B} = \alpha(r)\boldsymbol{B} \qquad (3.14)$$

Taking the divergence of (3.14) leads to the condition $\boldsymbol{B} \cdot \nabla \alpha(r) = 0$, which means that the function $\alpha(r)$ is constant along field lines.

The Lundquist model

If we set $\alpha(r) = \alpha$ constant in equation (3.14) and solve the resulting differential equation we get the so-called Lundquist solution.

$$B_\varphi = B_z^0 J_1(\alpha r), \qquad B_z = B_z^0 J_0(\alpha r) \qquad (3.15)$$

where J_0 and J_1 are the Bessel functions of first kind.

The Lundquist model has been the reference model to reconstruct the in-situ measurements of flux ropes since the 1990s Lepping et al. (1990).

The following figure displays the poloidal and axial components of the magnetic field for different

values of α.
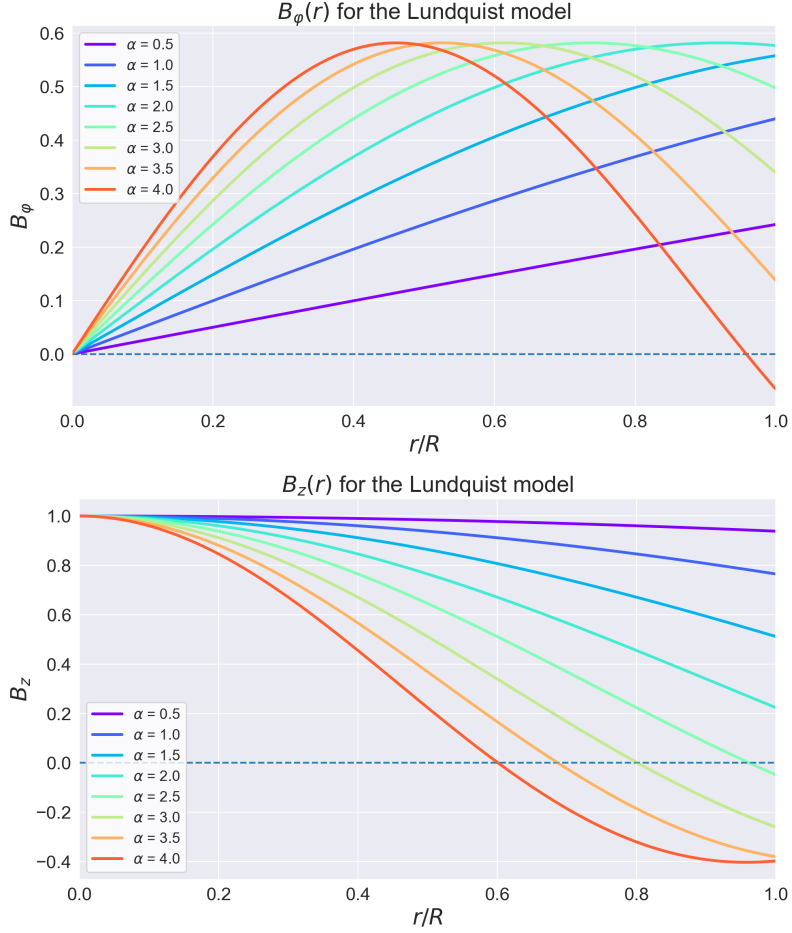
Figure 3.4: Axial and poloidal magnetic field components of the Lundquist model for α ranging from 0.5 to 4. The parameter B_z^0 is set to 1.

3.1.4 Circular-cylindrical (CC) model

This model was developed by Nieves-Chinchilla et al. (2016) and does not impose any force-free conditions on the MFR. It supposes both cylindrical and circular symmetries, that is, the quantities depend neither on φ nor z. Therefore, all the dependencies the radial component r. It is assumed that the MFR axis is the y axis. We assume the axis of the flux rope is aligned with the z. Note that the results presented by Nieves-Chinchilla et al. (2016) assume that the flux rope is lying in the y axis and non-conventional cylindrical coordinates are used (r, y, φ). While this does not has any physical significance, some mathematical expressions can very in a sign or subscript.

As we have previously shown, the cylindrical geometry implies that j_r and B_r are zero. The model assumes that the φ and z current density components have a generic series expansion of the form:

$$\boldsymbol{j}(r) = (j_r(r), j_\varphi(r), j_z(r)) = \left(0, \sum_{n=1}^{\infty} \alpha_n r^n, \sum_{m=0}^{\infty} \beta_m r^m\right) \tag{3.16}$$

where α_n, β_m are constant real coefficients (positive or negative). It is assumed that the current density components do not change sign, and that the poloidal component is positive. This means that the sign of the axial current density determines the *chirality* of the flux rope, which is defined

to be right-handed (or positive) is $j_z > 0$ and left-handed (or negative) if $j_z < 0$. This can be seen graphically in the following figure.
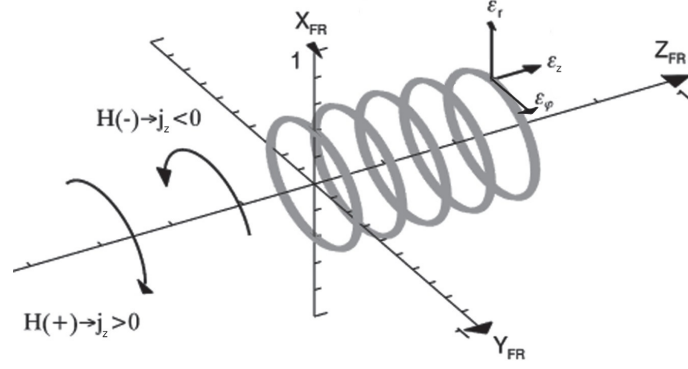
Figure 3.5: Scheme of the density currents inside the a flux rope described by the CC model.

Plugging the expression of $\boldsymbol{j}(r)$ in equation (3.9) and integrating the power series term by term leads to an expression for the magnetic field:

$$
\begin{cases}
B_r = 0 \\
B_\varphi = \mu_0 \sum_{m=0}^{\infty} \frac{\beta_m}{m+2} r^{m+1} \\
B_z = B_z^0 - \mu_0 \sum_{n=1}^{\infty} \frac{\alpha_n}{n+1} r^{n+1}
\end{cases}
\tag{3.17}
$$

Also, we will always assume $B_z^0 > 0$ since we will assume that the axial magnetic field is positive at the MFR axis. If this was not the case, we could invert the z axis (and the rest of the axis accordingly) to obtain a positive axial magnetic field at the center.

The Lorentz force is given by:

$$
\boldsymbol{j} \times \boldsymbol{B} = \left[\sum_{n,n'=1}^{\infty} \left[B_y^0 \alpha_{n'} r^{n'} - \mu_0 \alpha_n \alpha_{n'} \frac{r^{n+n'+1}}{n+1} \right] - \mu_0 \sum_{m,m'=0}^{\infty} \left[\beta_m \beta_{m'} \frac{r^{m+m'+1}}{m+2} \right] \right] \hat{\boldsymbol{e}}_{\boldsymbol{r}}
$$

$$
\tag{3.18}
$$

Notice that the Lorentz force is radial.

Simplification of the model: only 1 term

We can simplify the CC model by keeping just one term of the infinite power series. We call this model the simplified CC model which is indexed by the numbers n and m. This way the model is much simpler and the field components can be determined by only 3 parameters: α_n, β_m and B_z^0.

In this case, the current density is:

$$\boxed{\boldsymbol{j}(r) = (j_r(r), j_\varphi(r), j_z(r)) = (0, \alpha_n r^n, \beta_m r^m)}$$ (3.19)

In this case $\alpha_n > 0$ and the sign of β_m determines the chirality. The magnetic field is:

$$\boxed{\begin{cases} B_r = 0 \\ B_\varphi = \mu_0 \beta_m \dfrac{r^{m+1}}{m+2} \\ B_z = B_z^0 - \mu_0 \alpha_n \dfrac{r^{n+1}}{n+1} \end{cases}}$$ (3.20)

We can reparametrize the magnetic field using two parameters τ and C_{nm} instead of α_n and β_m. These are adimensional parameters that are easier to work with and to compare. We define τ as the ratio of the axial magnetic field at the center of the MFR to the difference of axial magnetic fields at the center and at its boundary. Similarly, we define the C_{nm} parameter as the ratio of the poloidal and axial components of the current density.

$$\boxed{\tau = \frac{B_z(0)}{B_z(0) - B_z(R)} = \frac{B_z^0}{\mu_0 \alpha_n \frac{R^{n+1}}{n+1}}, \qquad C_{nm} = \frac{j_\varphi(R)}{j_z(R)} = \frac{\alpha_n}{\beta_m} R^{n-m}}$$ (3.21)

Note that $\tau > 0$ since B_z^0 and α_n are strictly positive. Furthermore, if we want the axial magnetic field to not change the sign, we need $\tau > 1$. On the other hand, C_{nm} has the same sign as β_m, that is, the chirality of the MFR.

The magnetic fields are:

$$\boxed{\begin{cases} B_r = 0 \\ B_\varphi = \dfrac{B_z^0}{\tau C_{nm}} \dfrac{n+1}{m+2} \left(\dfrac{r}{R}\right)^{m+1} \\ B_z = B_z^0 \left(1 - \dfrac{1}{\tau} \left(\dfrac{r}{R}\right)^{n+1}\right) \end{cases}}$$ (3.22)

Notice that the parameter B_z^0 (axial magnetic field at $r = 0$ has the effect of scaling the magnetic field and does not interfere with the shape of its profile. Also, the factor $\dfrac{n+1}{m+2}$ is just a constant (once n and m are fixed). This constant can be included in the definition of C_{nm}, by defining $\tilde{C}_{nm} = \dfrac{m+2}{n+1} C_{nm}$. Also, by introducing the reduced radius $\bar{r} = \dfrac{r}{R} \in (0, 1]$ we can further simplify the expression of the magnetic field:

$$\boxed{\begin{cases} B_r = 0 \\ B_\varphi = \dfrac{B_z^0}{\tau \tilde{C}_{nm}} \bar{r}^{m+1} \\ B_z = B_z^0 \left(1 - \dfrac{1}{\tau} \bar{r}^{n+1}\right) \end{cases}}$$ (3.23)

The twist $Q(r)$ can be evaluated using equation 3.13 and leads to:

$$Q(\bar{r}) = \frac{B_\varphi(\bar{r})}{r B_z(\bar{r})} = \frac{1}{R\tilde{C}_{nm}} \frac{\bar{r}^m}{\tau - \bar{r}^{n+1}} \tag{3.24}$$

The parameter $\tilde{C}_{nm}$ does not affect the twist profile, it just scales it, where τ is the one that determines the shape of the twist profile. Figure 3.6 shows the twist profiles for $n = 1, m = 0$ and $n = 1, m = 1$.
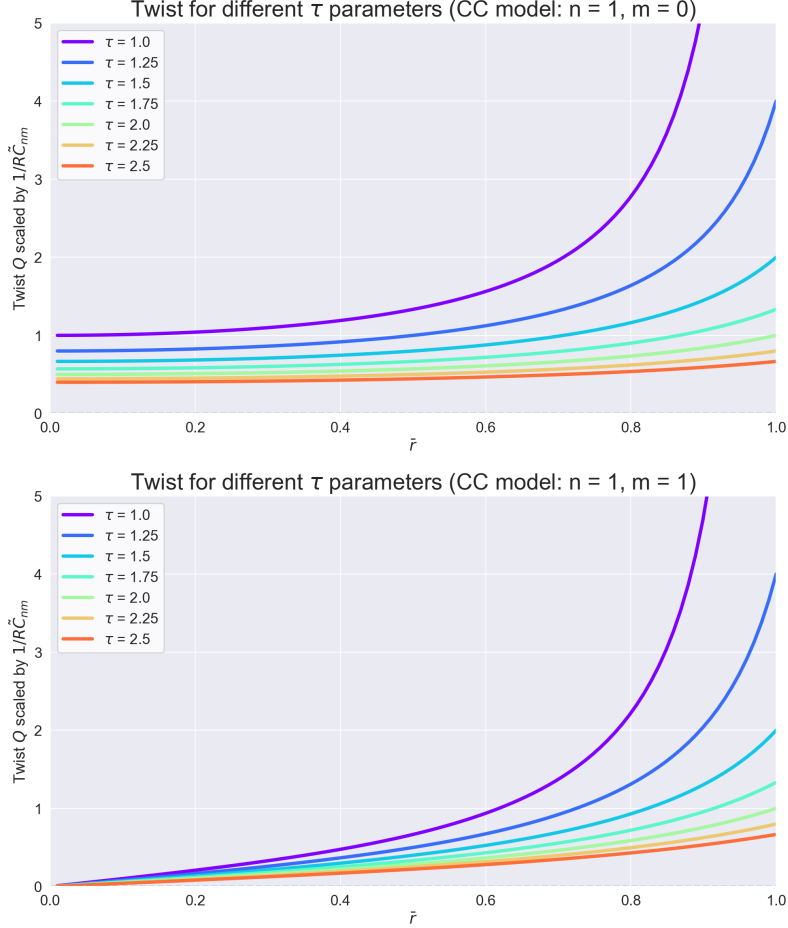
Figure 3.6: Twist profiles for the CC model for [n, m] = [1, 0] and [n, m] = [1, 1].

Note that $Q(0) = \frac{1}{R\tilde{C}_{nm}\tau}$ for $m = 0$ and $Q(0) = 0$ for $m \geq 1$. Also notice that $Q(1) = \frac{1}{R\tilde{C}_{nm}} \frac{1}{1-\tau}$.

Let's further analyze the twist expression. The denominator of equation (3.24) could be zero for some $\bar{r}$ and thus, we would have infinite twist for some radial distance (since the numerator will not be zero unless $\bar{r} = 0$):

$$\tau - \bar{r}^{n+1} = 0 \iff \tau = \bar{r}^{n+1} \tag{3.25}$$

Therefore, if we have $\tau \in (0, 1]$ we have a divergence of the twist. Note that for $\tau = 1$, the twist becomes infinite at the boundary of the MFR ($r = R$).

The magnetic potential of the CC model will be important for its use in the Grad-Shafranov Reconstruction Technique in section 5. We can calculate the magnetic potential from equation (3.10), which results in:

$$
\begin{cases}
A_r = 0 \\
A_\varphi(r) = -\dfrac{1}{r}\displaystyle\int_0^r r' B_z(r')dr' = A_\varphi^0 + \dfrac{B_z^0 r}{2} - \mu_0 \alpha_n \dfrac{r^{n+2}}{(n+1)(n+3)} \\
A_z(r) = -\displaystyle\int_0^r B_\varphi(r')dr' = A_z^0 - \mu_0 \beta_m \dfrac{r^{m+2}}{(m+2)^2}
\end{cases}
\tag{3.26}
$$

It will be of special interest to know the z-component of the magnetic vector potential, and that it only depends on the value of m and β_m but not n and α_n.

If we are interested in the hydrostatic pressure, it is reasonable to assume that the flux rope is in equilibrium and therefore use the momentum equation for a plasma in equilibrium to calculate it. For that, we need the Lorentz force, which we can determine from equation (3.18). In this simplified case, the Lorentz force turns out to be:

$$
\boldsymbol{\nabla} p = \boldsymbol{j} \times \boldsymbol{B} = \left(\alpha_n B_z^0 r^n - \frac{\mu_0 \alpha_n^2}{n+1} r^{2n+1} - \frac{\mu_0 \beta_m^2}{m+2} r^{2m+1} \right) \hat{\boldsymbol{e}}_{\boldsymbol{r}}
\tag{3.27}
$$

Therefore, integrating the previous expression with respect to the radial distance r we obtain the pressure:

$$
p(r) = p_0 + \frac{\alpha_n B_z^0}{n+1} r^{n+1} - \frac{\mu_0 \alpha_n^2}{2(n+1)^2} r^{2n+2} - \frac{\mu_0 \beta_m^2}{(m+2)(2m+2)} r^{2m+2}
\tag{3.28}
$$

Where $p_0 = p(0)$ is the pressure at the center of the MFR and cannot be determined since, given the gradient of p, one can know p unless constants. However, what we know is that the pressure should always be positive and, therefore p_0 should be greater than a threshold value (that depends on the model parameters) to guarantee $p(r) \geq 0$ for $r \in [0, R]$.

3.2 Elliptical-cylindrical symmetric models for MFRs

The elliptical geometry introduces more geometrical complexity to the model compared to circular-cylindrical models. In this case, the cross-section of the flux rope is distorted in an elliptical manner. Elliptical geometry is a non-orthogonal geometry. This is why operators such as the gradient, divergence, curl, and cross product must be generalized to nonorthogonal curved spaces, where the covariant and contravariant coordinates are distinguished in order to preserve the physical quantities independent of the coordinate system chosen (Nieves-Chinchilla et al., 2018).

3.2.1 Elliptical-cylindrical (EC) model

This model was developed by Nieves-Chinchilla et al. in 2018 (Nieves-Chinchilla et al., 2018), two years after the publication of the CC model. The EC model constitutes the first level of complexity above that of a circular-cylindrical geometry. The model describes the MFR geometry with a distorted cross-section with an elliptical shape. The distortion could be a possible consequence of the MFR with the solar wind (Nieves-Chinchilla et al., 2018).

The new geometrical parameters of this model with respect to the CC model are:

1. **The distortion** (or ellipticity): $\delta = \frac{a}{b} \in (0, 1]$, defined as the ratio of the minor to major axis, named a and b, respectively. The major semiaxis b is also sometimes referred as the

radius R and, therefore, the minor axis is $a = \delta \cdot R$. Note that for $\delta = 1$ the ellipse becomes a circumference. The distortion parameter δ is closely related to the eccentricity of the ellipse, this being: $e = \sqrt{1 - \left(\frac{a}{b}\right)^2} = \sqrt{1 - \delta^2}$.

2. **The ellipse rotation angle**: $\xi \in [0, \pi)$. To develop the equations that describe this model we will assume $\xi = 0$. A rotation of angle ξ can be performed afterward to obtain the desired rotation of the ellipse.
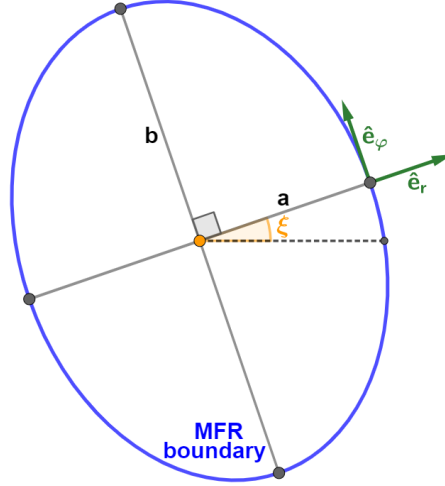
Figure 3.7: Scheme of the cross-section of an elliptical-cylindrical magnetic flux rope, as the EC model. The minor axis is a, the major axis is b and the ellipse rotation angle is ξ. The radial and poloidal unit vectors $\hat{\boldsymbol{e}}_r$ and $\hat{\boldsymbol{e}}_\varphi$ are also shown.

The use of a non-orthogonal coordinate system is needed, which brings a certain level of complexity to the mathematical formulation. The coordinate system used is (r, φ, z), whose relation with Cartesian coordinates is the following:

$$x_c = \delta r \cos \varphi, \quad y_c = r \sin \varphi, \quad z_c = z \tag{3.29}$$

with $r \in [0, R]$, $\varphi \in [0, 2\pi)$ and $z \in (-\infty, \infty)$.

Let us introduce two convenient parameters χ and h, which are both functions of φ:

$$h(\varphi) = \sqrt{\delta^2 \sin^2(\varphi) + \cos^2(\varphi)}, \qquad \chi(\varphi) = \frac{\delta^2 + 1}{h(\varphi)^2} \tag{3.30}$$

It is worth noticing that when $\delta = 1$ (circumference), the previously mentioned parameters do not depend on φ and have the following values $h = 1$ and $\chi = 2$.

The simplified model (only 1 term) expressions for the current density and magnetic field are the following:

$$\boldsymbol{j}(r, \varphi) = (j_r(r, \varphi), j_\varphi(r, \varphi), j_z(r, \varphi)) = \left(0, h\alpha_n r^n, h^2 \beta_m \frac{(\chi + m)}{(\delta^2 + m + 1)} r^m\right) \tag{3.31}$$

And the corresponding magnetic fields are:

28

$$\begin{cases} B_r = 0 \\ B_\varphi = \mu_0 h \delta \beta_m \dfrac{r^{m+1}}{\delta^2 + m + 1} \\ B_z = B_z^0 - \delta \mu_0 \alpha_n \dfrac{r^{n+1}}{n+1} \end{cases} \tag{3.32}$$

Notice that when $\delta = 1$ (circumference), we recover the same current density and magnetic field equations as in (3.19) and (3.20).

Similarly as we did with the CC model, we can define the parameter τ in the same way:

$$\tau = \frac{B_z(0)}{B_z(0) - B_z(R)} = \frac{B_z^0}{\delta \mu_0 \alpha_n \frac{R^{n+1}}{n+1}} = \frac{\tau^{CC}}{\delta} \tag{3.33}$$

We would like to define C_{nm} also as in the CC model:

$$\frac{j_\varphi(R)}{j_z(R)} = \frac{\delta^2 + m + 1}{h(\chi + m)} \frac{\alpha_n}{\beta_m} R^{n-m} = \frac{\delta^2 + m + 1}{h(\chi + m)} C_{nm}^{CC} \tag{3.34}$$

However, the problem with the previous definition is that depends on φ since h and χ depend on the poloidal coordinate. Therefore it is not a constant and the C_{nm} parameter is defined as in the CC model:

$$C_{nm} = \frac{\alpha_n}{\beta_m} R^{n-m} \tag{3.35}$$

The previous equation gives an expression for the parameters τ and C_{nm} as a function of α_n, β_m. It is of interest to know the inverse relationship between these parameters:

$$\begin{cases} \alpha_n = \dfrac{B_z^0(n+1)}{\delta \mu_0 \tau R^{n+1}} \\ \beta_m = \dfrac{B_z^0(n+1)}{\delta \mu_0 \tau R^{m+1} C_{nm}} \end{cases} \tag{3.36}$$

Similarly as with Nieves-Chinchilla's CC model, the plasma pressure of the EC model can be calculated. To do so we apply the momentum equation for plasma in equilibrium $\boldsymbol{\nabla} p = \boldsymbol{j} \times \boldsymbol{B}$. Taking into account the non-orthogonal expression for the cross product, one obtains:

$$p(r) = p_0 + h \left[\frac{\alpha_n B_z^0}{n+1} r^{n+1} - \frac{\mu_0 \delta \alpha_n^2}{2(n+1)^2} r^{2n+2} - \frac{\mu_0 \delta h^2 \beta_m^2 (\chi + m)}{(\delta^2 + m + 2)(2m + 2)} r^{2m+2} \right] \tag{3.37}$$

Using the previous expression for the pressure, the pressure profile in a straight line across a MFR described by the EC model has been determined. Figure 3.8 depicts the behavior of the pressure for different values of the distortion.
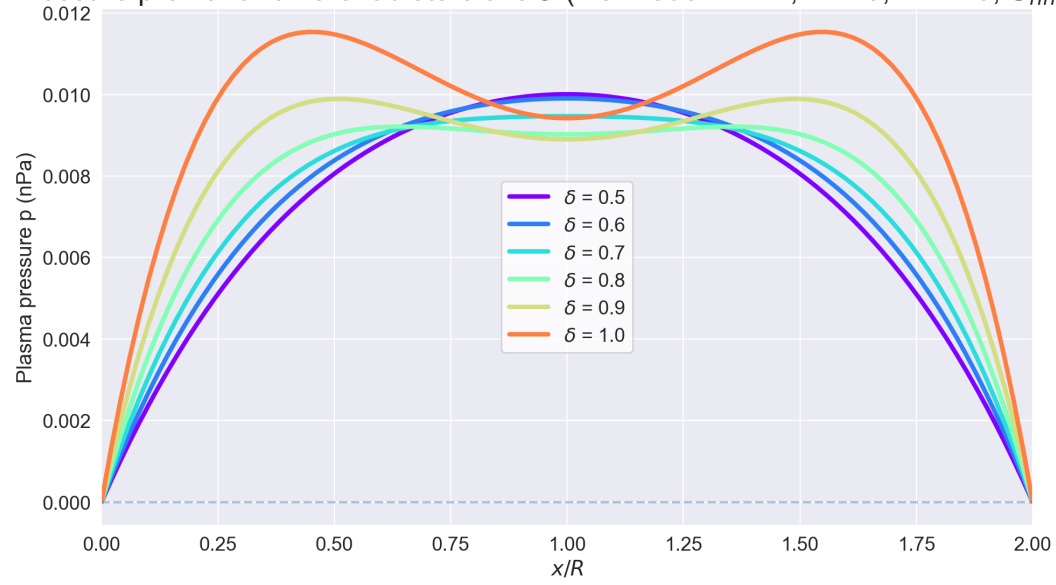
Figure 3.8: Pressure profiles in a straight line through the center of a MFR described by the EC model.

4. The Grad-Shafranov equation and reconstruction technique

In this chapter, we provide a detailed explanation of the Grad-Shafranov equation and the reconstruction technique. From the fundamental equations from which it is derived and the assumptions made to one of its applications: the so-called Grad-Shafranov Reconstruction Technique.

4.1 Fundamentals

The Grad-Shafranov (GS) equation (Grad and Rubin, 1958), (Shafranov, 1966) is the equilibrium equation in ideal magnetohydrodynamics (MHD) for a two-dimensional plasma, for example, the axisymmetric toroidal plasma in a tokamak. The GS equation takes the same form as Hick's equation from fluid dynamics. It is a 2-dimensional, nonlinear, elliptic partial differential equation obtained from the reduction of the ideal MHD equations to two dimensions (Daniel et al., 2021).

We assume ideal MHD equilibrium (section 2.3), that is ideal MHD with no time variation.

The GS equation is derived from the following three equations, which involve the magnetic field, current density and pressure:

1. Gauss' law for magnetism:

$$\boldsymbol{\nabla} \cdot \boldsymbol{B} = 0 \tag{4.1}$$

2. Ampère's law:

$$\boldsymbol{\nabla} \times \boldsymbol{B} = \mu_0 \boldsymbol{j} \tag{4.2}$$

3. The momentum equation for a plasma in equilibrium:

$$\boldsymbol{\nabla} p = \boldsymbol{j} \times \boldsymbol{B} \tag{4.3}$$

The fundamental equilibrium condition is that the forces are zero at all points. Assuming the absence of plasma resistance, that is, ideal MHD conditions, we require that the magnetic and pressure forces balance at all points.

4.2 GS equation in cylindrical geometry

It is assumed that the system has as the invariant axis (z axis), that is, $\frac{\partial}{\partial z} = 0$ for all quantities. It is common to name this a 2.5-dimensional configuration since even if the fields are 3-dimensional, variations of them occur only on 2 of them.

The magnetic vector potential is $\boldsymbol{A}(x, y) = A_x(x, y)\hat{\boldsymbol{e}}_{\boldsymbol{x}} + A_y(x, y)\hat{\boldsymbol{e}}_{\boldsymbol{y}} + A_z(x, y)\hat{\boldsymbol{e}}_{\boldsymbol{z}}$. Therefore, the magnetic field is related to the magnetic potential vector in the following manner:

$$\boldsymbol{B} = (B_x, B_y, B_z) = \boldsymbol{\nabla} \times \boldsymbol{A} = \left(\frac{\partial A_z}{\partial y}, -\frac{\partial A_z}{\partial x}, \frac{\partial A_y}{\partial x} - \frac{\partial A_x}{\partial y} \right) \tag{4.4}$$

where we have used that $\frac{\partial A}{\partial z} = 0$ to simplify the curl expression. Note that $\boldsymbol{B}$ can be rewritten as:

$$\boldsymbol{B} = \boldsymbol{B}_\perp + \boldsymbol{B_z} = \boldsymbol{\nabla} A_z \times \hat{\boldsymbol{e}}_{\boldsymbol{z}} + B_z \hat{\boldsymbol{e}}_{\boldsymbol{z}} \tag{4.5}$$

From the previous expression we see that $\boldsymbol{\nabla} A_z$ is perpendicular to $\boldsymbol{B}$ at all points since:

$$\boldsymbol{\nabla} A_z \cdot \boldsymbol{B} = \boldsymbol{\nabla} A_z \cdot (\boldsymbol{\nabla} A_z \times \hat{\boldsymbol{e}}_{\boldsymbol{z}}) + \boldsymbol{\nabla} A_z \cdot (B_z \hat{\boldsymbol{e}}_{\boldsymbol{z}}) = 0 + 0 = 0 \tag{4.6}$$

We will now show that the pressure is only a function of A_z. First, we observe that the gradient of pressure is perpendicular to the magnetic field:

$$\boldsymbol{B} \cdot \boldsymbol{\nabla} p = \boldsymbol{B} \cdot (\boldsymbol{j} \times \boldsymbol{B}) = 0 \tag{4.7}$$

From this equation, expanding the magnetic field in its perpendicular and axial components:

$$0 = \boldsymbol{B} \cdot \boldsymbol{\nabla} p = (\boldsymbol{B}_\perp + \boldsymbol{B_z}) \cdot \boldsymbol{\nabla} p = (\boldsymbol{\nabla} A_z \times \hat{\boldsymbol{e}}_{\boldsymbol{z}}) \cdot \boldsymbol{\nabla} p \tag{4.8}$$

From where we conclude that $\boldsymbol{\nabla} p \parallel \boldsymbol{\nabla} A_z$ and therefore, that the pressure is only a function of A_z. A similar procedure shows that B_z is also only a function of A_z.

From Ampère's law we can calculate the current density as:

$$\boldsymbol{j} = \frac{1}{\mu_0} \boldsymbol{\nabla} \times \boldsymbol{B} = \frac{1}{\mu_0} \left(\frac{\partial B_z}{\partial y}, -\frac{\partial B_z}{\partial x}, \frac{\partial B_y}{\partial x} - \frac{\partial B_x}{\partial y} \right) \tag{4.9}$$

Note that the second derivatives of A_z are related to the x and y component of the magnetic field:

$$\frac{\partial^2 A_z}{\partial x^2} = -\frac{\partial}{\partial x}\left(-\frac{\partial A_z}{\partial x} \right) = -\frac{\partial B_y}{\partial x} \tag{4.10}$$

$$\frac{\partial^2 A_z}{\partial y^2} = \frac{\partial}{\partial y}\left(\frac{\partial A_z}{\partial y} \right) = \frac{\partial B_x}{\partial y} \tag{4.11}$$

And then:

$$j_z = \frac{1}{\mu_0}\left(\frac{\partial B_y}{\partial x} - \frac{\partial B_x}{\partial y} \right) = \frac{1}{\mu_0}\left(-\frac{\partial^2 A}{\partial x^2} - \frac{\partial^2 A}{\partial y^2} \right) = -\frac{1}{\mu_0} \boldsymbol{\nabla}_\perp^2 A \tag{4.12}$$

From we can rewrite $j_z = -\frac{1}{\mu_0} \boldsymbol{\nabla}_\perp^2 A_z$. Also note that similarly as we did before with the magnetic field, we can write the perpendicular component of the current density as $j_\perp = \frac{1}{\mu_0} \boldsymbol{\nabla} B_z \times \hat{\boldsymbol{e}}_{\boldsymbol{z}}$.

With this, plugging the expressions for $\boldsymbol{j}$ and $\boldsymbol{B}$ in the momentum equation for plasma in equilibrium leads to:

$$\boldsymbol{\nabla} p = (\boldsymbol{j}_\perp + \boldsymbol{j}_{\boldsymbol{z}}) \times (\boldsymbol{B}_\perp + \boldsymbol{B}_{\boldsymbol{z}}) = \boldsymbol{j}_\perp \times \boldsymbol{B}_\perp + \boldsymbol{j}_\perp \times \boldsymbol{B}_{\boldsymbol{z}} + \boldsymbol{j}_{\boldsymbol{z}} \times \boldsymbol{B}_\perp + \boldsymbol{j}_{\boldsymbol{z}} \times \boldsymbol{B}_{\boldsymbol{z}}$$

(4.13)

Since $\frac{\partial p}{\partial z} = 0$ we have that $\boldsymbol{j}_\perp \times \boldsymbol{B}_\perp = 0$, meaning that $\boldsymbol{j}_\perp$ and $\boldsymbol{B}_\perp$ are parallel. Also since $\boldsymbol{j}_{\boldsymbol{z}} = j_z \hat{\boldsymbol{e}}_{\boldsymbol{z}}$ and $\boldsymbol{B}_{\boldsymbol{z}} = B_z \hat{\boldsymbol{e}}_{\boldsymbol{z}}$, this implies that $\boldsymbol{j}_{\boldsymbol{z}} \times \boldsymbol{B}_{\boldsymbol{z}} = 0$. Therefore the previous expression for $\boldsymbol{\nabla} p$ reduces to only 2 terms, that involve the cross product of the perpendicular and axial component of the current density and magnetic field:

$$\boldsymbol{\nabla} p = \boldsymbol{j}_\perp \times \boldsymbol{B}_{\boldsymbol{z}} + \boldsymbol{j}_{\boldsymbol{z}} \times \boldsymbol{B}_\perp$$

(4.14)

The first term can be expressed as:

$$\boldsymbol{j}_\perp \times \boldsymbol{B}_{\boldsymbol{z}} = \left(\frac{1}{\mu_0} \boldsymbol{\nabla} B_z \times \hat{\boldsymbol{e}}_{\boldsymbol{z}} \right) \times (B_z \hat{\boldsymbol{e}}_{\boldsymbol{z}}) = \frac{B_z}{\mu_0} (\boldsymbol{\nabla} B_z \times \hat{\boldsymbol{e}}_{\boldsymbol{z}}) \times \hat{\boldsymbol{e}}_{\boldsymbol{z}} = -\frac{B_z}{\mu_0} \boldsymbol{\nabla} B_z$$

(4.15)

where we have used the triple cross product identity: $(\boldsymbol{u} \times \boldsymbol{v}) \times \boldsymbol{w} = (\boldsymbol{w} \cdot \boldsymbol{u})\boldsymbol{v} - (\boldsymbol{w} \cdot \boldsymbol{v})\boldsymbol{u}$.

Similarly, the second term simplifies to:

$$\boldsymbol{j}_{\boldsymbol{z}} \times \boldsymbol{B}_\perp = -\frac{1}{\mu_0} \nabla_\perp^2 A_z \hat{\boldsymbol{e}}_{\boldsymbol{z}} \times (\boldsymbol{\nabla} A_z \times \hat{\boldsymbol{e}}_{\boldsymbol{z}}) = -\frac{1}{\mu_0} \nabla_\perp^2 A_z \boldsymbol{\nabla} A_z$$

(4.16)

Combining the previous two expressions into equation (4.14) leads to:

$$\boldsymbol{\nabla} p = -\frac{B_z}{\mu_0} \boldsymbol{\nabla} B_z - \frac{1}{\mu_0} \nabla_\perp^2 A_z \boldsymbol{\nabla} A_z$$

(4.17)

Now, using the fact that p and B_z are only functions of A_z we can write $\boldsymbol{\nabla} p = \frac{dp}{dA_z} \boldsymbol{\nabla} A_z$ and $\boldsymbol{\nabla} B_z = \frac{dB_z}{dA_z} \boldsymbol{\nabla} A_z$, we can rewrite equation (4.17):

$$\frac{dp}{dA_z} \boldsymbol{\nabla} A_z = -\frac{B_z}{\mu_0} \frac{dB_z}{dA_z} \boldsymbol{\nabla} A_z - \frac{1}{\mu_0} \nabla_\perp^2 A_z \boldsymbol{\nabla} A_z$$

(4.18)

Canceling out the $\boldsymbol{\nabla} A_z$ from the 3 terms and rearranging leads to the Grad-Shafranov equation:

$$\boldsymbol{\nabla}_\perp^2 A_z(x, y) = \frac{\partial^2 A_z}{\partial x^2} + \frac{\partial^2 A_z}{\partial y^2} = -\mu_0 \frac{d}{dA_z} \left(p + \frac{B_z^2}{2\mu_0} \right)$$

(4.19)

The term $p + \frac{B_z^2}{2\mu_0}$ is defined as the *transverse pressure* p_t. It is standard to simply use A to denote its z component, A_z. In this work we have decided to explicitly keep the subscript.

A similar derivation of the GS equation for circular geometry ($\frac{\partial}{\partial \varphi} = 0$) can be found in the annex

33

4.2.1 Theory on the cylindrical GS equation PDE

The cylindrical GS equation (equation 4.19) is a partial derivative equation (PDE). The unknown function is the z component of the magnetic potential $A_z(x, y)$. As it is common in PDEs, we will call the unknown function $u(x, y)$. It is a PDE of 2nd order since the greatest order of the derivatives is 2. The right hand side of the GS equation 4.19 is a function of u. Let's call this function f.

$$f : \mathbb{R} \longrightarrow \mathbb{R} \tag{4.20}$$
$$u \longmapsto f(u) \tag{4.21}$$

With the previous definitions, the GS equation takes the form:

$$\Delta u = f(u) \tag{4.22}$$

This equation reminds us of the 2-dimensional Poisson's equation $\Delta u(x, y) = g(x, y)$. However, they are not the same. The non-homogeneous part of Poisson's equation is a function that depends on the spatial coordinates $g(x, y)$. However, in our case, the non-homogeneous term is a function $f(u)$ that depends on the unknown function. Of course the unknown function $u(x, y)$ is a function of x and y and we could, in theory, define $h(x, y) := f(u(x, y))$. The problem here is that we do not know $u(x, y)$ as it is the unknown function.

If we do a Taylor expansion of degree N of f around $u = 0$, we can approximate our function f by its Taylor polynomial of degree N:

$$f(u) \simeq P_N(u) = \sum_{k=0}^{N} \frac{f^{(k)}(0)}{k!} u^k \tag{4.23}$$

Therefore the GS equation can be approximated by:

$$\Delta u \simeq \sum_{k=0}^{N} \alpha_k u^k, \qquad \alpha_k := \frac{f^{(k)}(0)}{k!} \tag{4.24}$$

For our application in the Grad-Shafranov Reconstruction Technique (section 4.4) we have usually set $N = 1$. To be precise, it is common to approximate f as a degree 1 polynomial for a range of u and exponential tails outside this interval. Therefore, it may be interesting to study the analytical behavior of equation 4.22 when the function f is linear in u and when it is of the form e^u.

Boundary conditions are crucial to PDEs. Since the GS equation is an elliptical equation, it is common for it to be accompanied by a certain boundary condition in the border of the domain. However, as we will detail in section 4.4, the crossing of a spacecraft through a MFR only provides a boundary condition for A_z in a line inside the reconstruction domain.

4.3 Connection of the GS equation CC and EC models

In section 3 we have introduced the CC and EC models while in this section the GS equation was presented. What the differences and similarities between them are is the question we aim to answer in this section.

On the one side, the GS equation is a fundamental equation (not a model) derived from three basic equations of magnetohydrodynamics, as explained in section 4.1. These are:

1. Gauss's law for magnetism

2. Ampère's law

3. The momentum equation for a plasma in equilibrium

As we have seen, the GS equation can take different forms depending on the geometry and symmetries of the system where it is applied. As for its form in cylindrical geometry, no assumption is made on the angular or other dependence of the fields.

On the other side, both the CC and EC models rely on on two fundamental equations:

1. Gauss's law for magnetism (which implies $B_r = 0$)

2. Ampère's law (to relate the current density and magnetic field)

We notice that the CC and EC models do not use the momentum equation for plasma in equilibrium while the GS equation does. This is because the CC and EC models do not need the pressure to be defined. If equilibrium is assumed, the pressure of these models is calculated as $\boldsymbol{\nabla} p = \boldsymbol{j} \times \boldsymbol{B}$ as well.

As for the geometrical assumptions, the CC model has both cylindrical and circular symmetry whereas the EC model has cylindrical and elliptical symmetry. This means that, geometrically, the GS equation is less constrained than the CC and EC models.

With this, we conclude that the CC and EC models agree with the GS equation and their corresponding A_z must be a solution to the GS equation provided that the pressure is calculated as $\boldsymbol{\nabla} p = \boldsymbol{j} \times \boldsymbol{B}$.

4.4 The Grad-Shafranov Reconstruction Technique (GSRT)

The Grad-Shafranov Reconstruction Technique (GSRT) is a method to infer 2.5-dimensional magnetic structures based on measurements taken by a single spacecraft crossing the MFR.

This method was first introduced by Sonnerup and Guo (1996), being tested on a magnetopause crossing of the tangential-discontinuity type by the spacecraft AMPTE/IRM. The magnetopause is the abrupt boundary between a magnetosphere and the surrounding plasma. The technique was rapidly tested and improved by other researchers Hau and Sonnerup (1999), Hu and Sonnerup (2000), Hu and Sonnerup (2001) and Hu and Sonnerup (2002), who started applying the GSRT to magnetic flux ropes in the solar wind. Multiple reviews of the method have been made over the years, being the most relevant: Sonnerup et al. (2006) and Hu et al. (2017). The GSRT has been actively used since its invention to analyze magnetic structures in the heliosphere. It is, thus, a very powerful tool that we believe should be easy to use and accessible to all researchers. For instance, in the recent paper by (Hu et al., 2021) the GSRT is applied to measurements of the novel NASA mission Solar Orbiter and also WIND spacecraft.

The method may be summarized in the following three steps, each of them with several substeps:

1. Frame determination

2. Numerical solution of the GS equation in the cross-section

3. Derived physical magnitudes and geometrical parameters

We organize the following sections according to the above-mentioned steps. The GSRT can be thought of as a machine that has an input and outputs the results:

- **Input**: a time series with containing the magnetic field components (usually in RTN coordinates), pressure and solar wind velocity.

- **Output**: a matrix with the values of $A_z(x,y)$ in the MFR cross-section.

From the recovered $A_z(x,y)$ one can determine the magnetic field profiles and other magnitudes inside the structure.
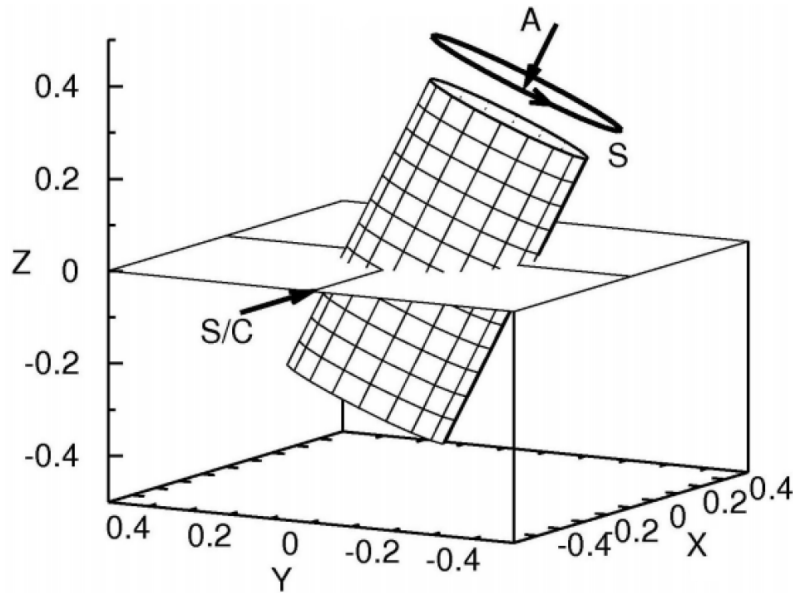

Figure 4.1: Scheme of the crossing of a spacecraft (s/c) through a magnetic flux rope and subsequent analyse using the Grad-Shafranov Reconstruction Technique. Retrieved from: Skan (2019).

4.4.1 Frame determination

The deHoffmann-Teller frame

The deHoffmann-Teller (HT) frame is a Galilean frame of reference in which the electric field vanishes in the plasma. It is named after F. De Hoffmann and E. Teller, who first applied this concept to MHD shock waves in their original work (F. De Hoffmann, 1950).

The existence of an HT frame indicates that a coherent quasi-stationary pattern of magnetic field and plasma velocity such as a wave or current layer, is present (Paschmann and Daly, 1998). The avail of a HT frame is that it allows one to identify the passage of such a moving quasi-static structure and that facilitates further analysis and interpretation of the data.

The procedure of identifying a HT frame is usually referred as HT analysis. It aims to find the frame velocity vector (HT velocity), $\boldsymbol{v_{HT}}$, that best agrees with the set of measured values of magnetic field, $\boldsymbol{B}$, and electric field, $\boldsymbol{E}$. In the case there are no measurements of the electric field (this is the case for most of the in-situ measurements) the convection electric field $-\boldsymbol{v} \times \boldsymbol{B}$ can be used as a proxy for $\boldsymbol{E}$ (Paschmann and Daly, 1998).

In this frame of reference, the structure appears static and time-stationary. It moves at a constant velocity $\boldsymbol{v_{HT}}$ such that the residue electric field due to remaining plasma flow is minimized, that

is, $E' = (v - v_{HT}) \times B \simeq 0$. The minimization of the electric field is performed in a minimum squares sense, that is, by minimizing the mean square of the convection electric field in the moving frame for the given set of M measurements:

$$D(v_F) = \frac{1}{M} \sum_{m=1}^{M} |E'(m)|^2 = \frac{1}{M} \sum_{m=1}^{M} \left| (v^{(m)} - v_F) \times B^{(m)} \right|^2 \qquad (4.25)$$

When $v_F = v_{HT}$ the quantity D is a minimum.

As a function of its vector argument v_F (frame velocity), the quantity D is a non-negative quadratic form which therefore must have a unique minimum. The minimisation condition is $\nabla_{v_F} D(v_F) = 0$ and leads to a linear equation for v_F. This minimization can also be done numerically.

The first step of the reconstruction is, therefore, to determine the HT frame. By subtracting the HT velocity to the measured velocities by the spacecraft, we set the frame of reference as co-moving with the MFR $v' = v - v_{HT}$. The quality of an HT frame can be measured by a correlation coefficient (cc) between the electric field components of $v \times B$ and $v_{HT} \times B$. Another test that can be done is the so-called *Walén test*, as described by Paschmann and Sonnerup (2008).

Orientation of the MFR

As can be seen in figure 4.1, the MFR can have multiple orientations in space. We denote the angle of the MFR with the standard spherical angles: $\varphi \in [0, 2\pi)$ (angle in the x-y plane) and $\theta \in [0, \pi]$ (angle with the z-axis).

Multiple methods have been widely used to determine the orientation of the MFR axis. Next, we summarize two of the most used.

1. **Intermediate variance**: consists in performing a variance analysis on the measured magnetic field vectors $B^{(m)}$. The magnetic variance matrix $\mathcal{M} = \langle B_\mu B_\nu \rangle - \langle B_\mu \rangle \langle B_\nu \rangle$ is calculated where the subscripts $\mu, \nu = x, y, z$ denote RTN components and the brackets $\langle \cdot \rangle$ denote the arithmetic average of the quantity within the chosen data set. The eigenvalues $\{\lambda_1, \lambda_2, \lambda_3\}$ (in descending order) and the corresponding normalized eigenvectors $\{\hat{x}_1, \hat{x}_2, \hat{x}_3\}$ of $\mathcal{M}$ are found. We take $\hat{x}_2$, the eigenvector with intermediate eigenvalue, as being the MFR axis $\hat{e}_z$. This analysis is usually called *Minimum Variance Analysis on the measured magnetic field* (MVAB).

   The same analysis can also be done with the unitary measured magnetic field: $\hat{B}^{(m)}$, in such case it is called *Minimum Variance analysis on the Unit magnetic field* (MVUB).

The reason for choosing the intermediate variance axis is the following: assume a spacecraft crosses a MFR with its trajectory aligned with the x-axis and MFR axis aligned with the z-axis. In such a case, given the magnetic topology of flux ropes, the y component of the magnetic field will change sign (have maximum variance), the x component will remain quite constant (have minimum variance) and the z component will not change sign but will increase near the center of the MFR (will have intermediate variance).

2. **Minimum residue**: The axis orientation of a cylindrical magnetic flux rope is determined by finding the direction, for which the data plot of $p_t(x_i, 0)$ versus $A_z(x_i, 0)$ displays minimal scatter. The theoretical background behind this fact is that the transverse pressure should be only a function of A_z and therefore the function describing the relation of the transverse pressure as a function of A_z should be single-valued.

When a spacecraft crosses a flux rope, A_z increases up to a maximum value near the center of the flux rope and then decreases to approximately the same value as the initial one. Therefore, when

plotting the transverse pressure vs A_z we observe two branches: corresponding to the 1st and 2nd halves of the trajectory of the spacecraft.

Figure 4.3 shows the two branches behaviour for an incorrect z axis. To be more precise, it if off the correct axis by only 3 degrees.
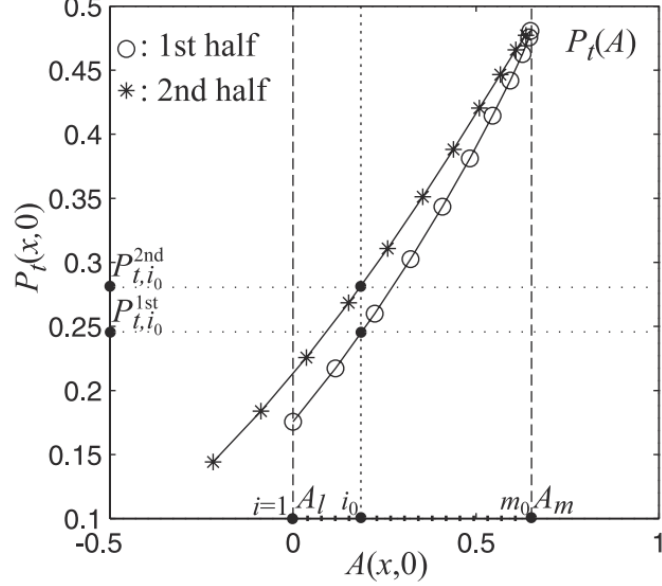

Figure 4.2: Illustration of behavior of $p_t(A)$ for an incorrect z axis orientation. Retrieved from: Hu and Sonnerup (2002).

In order to quantify the separation between the two branches, a residue of the scatter plot is calculated. It is a dimensionless parameter that can be assigned to every orientation of the axis (φ, θ).

$$\mathcal{R} = \frac{\sqrt{\sum\limits_{i=0}^{m_0} \left(P_{t,i}^{in} - P_{t,i}^{out}\right)^2}}{|\max(P_t) - \min(P_t)|} \tag{4.26}$$

Where the *in* and *out* superscripts correspond to the 1st and 2nd halves of the trajectory, respectively. Using this expression for the residue, a trial-and-error strategy is adopted, for which the residue is calculated for multiple orientations, that is, values of (φ, θ). The selected axis is the one with minimum residue.

Properly speaking, the technique used to determine the orientation of the MFR should be the minimum residue approach. However, it is usually useful to compare it to the MVAB and MVUB orientations. Both methods determine the MFR axis, which is to be set to the z-axis. However, there is an ambiguity with its sign. This ambiguity is solved by choosing the sign that provides a positive axial field B_z.

Once we have the axis orientation (φ, θ) we can proceed to complete the reconstruction frame. The x unit vector is chosen to be the normalized projection of $-\mathbf{v_{HT}}$ onto the plane perpendicular to $\hat{z}$ and the y unit vector completes the orthonormal triad:

$$\hat{\boldsymbol{z}} = (\cos\varphi\sin\theta, \; \sin\varphi\sin\theta, \; \cos\theta) \tag{4.27}$$

$$\hat{\boldsymbol{x}} = \frac{-\boldsymbol{v_{HT}} + (-\boldsymbol{v_{HT}} \cdot \hat{\boldsymbol{z}})\hat{\boldsymbol{z}}}{|-\boldsymbol{v_{HT}} + (-\boldsymbol{v_{HT}} \cdot \hat{\boldsymbol{z}})\hat{\boldsymbol{z}}|} \tag{4.28}$$

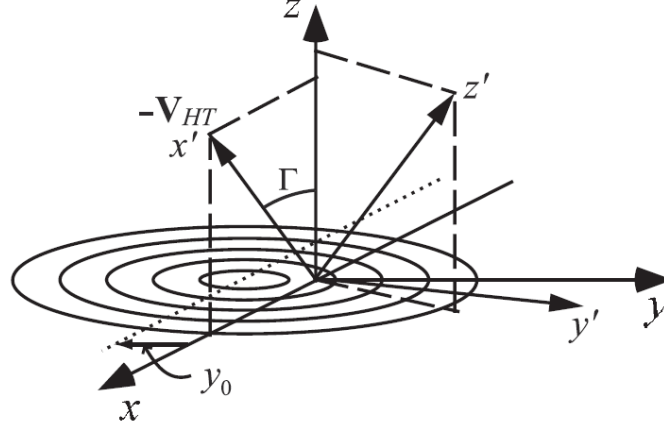$$\hat{\boldsymbol{y}} = \hat{\boldsymbol{z}} \times \hat{\boldsymbol{x}} \tag{4.29}$$

Figure 4.3: Sketch of the reconstruction frame (x, y, z) and the temprary frame (x', y', z') in which the residue is calculated. The x axis is determined as the projection of $-\boldsymbol{v_{HT}}$ onto the plane permendicular to $\hat{\boldsymbol{z}}$. Retrieved from: Hu and Sonnerup (2002)

With this, time elapsed can be converted to distance travelled by the spacecraft with the relation $\Delta x = -\boldsymbol{v_{HT}} \cdot \hat{\boldsymbol{x}} \; \Delta t$. This relation gives the distance travelled by the spacecraft inside the flux rope as $x_{max} = -\boldsymbol{v_{HT}} \cdot \hat{\boldsymbol{x}} \; t_{max}$.

4.4.2 Numerical solution of the GS equation

The domain in which the cross-section of the flux rope is to be recovered is a rectangular domain $[0, x_{max}] \times [-y_{max}, y_{max}]$. The domain is discretized in the x-direction with a step Δx and so it is in the y-direction with a step Δy, in a grid or matrix shape of dimensions $n_x \times n_y$. For numerical stability of the solver, the vertical step is taken to be around 10 times smaller than the horizontal one, that is: $\Delta y = 0.1\Delta x$.

The numerical derivatives in the grid are computed using $N = 5$ points:

$$\left(\frac{\partial A}{\partial x}\right)_i = \frac{2(A_{i+1} - A_{i-1}) + A_{i+2} - A_{i-2}}{8\Delta x} \tag{4.30}$$

which is a noise-robust differentiator Holoborodko (2008). The derivatives at the edges of the domain can be computed using the standard forward, central or backward difference scheme.

The second derivative is as computed as:

$$\left(\frac{\partial^2 A}{\partial x^2}\right)_i = \frac{A_{i+1} - 2A_i + A_{i-1}}{(\Delta x)^2}, \quad i \in \{1, n_x - 2\} \tag{4.31}$$

In the edges of the domain they can be calculated as:

39

$$\left(\frac{\partial^2 A}{\partial x^2}\right)_0 = \frac{2A_0 - 5A_1 + 4A_2 - A_3}{(\Delta x)^2} \tag{4.32}$$

A symmetric expression is used to calculate the second derivative at the right end point $\left(\frac{\partial^2 A}{\partial x^2}\right)_{n_x-1}$. As for the numerical integrals, they are done using the trapezoidal rule.

The steps towards the reconstruction of the cross-section are:

1. Obtain the value of $A(x,0)$ from $\boldsymbol{B} = (\frac{\partial A}{\partial y}, -\frac{\partial A}{\partial x}, B_z(A))$ by integration of the measured $B_y(x,0)$ values along the x axis.

$$A(x,0) = \int_0^x \frac{\partial A}{\partial \xi} d\xi = -\int_0^x B_y(\xi,0)d\xi \tag{4.33}$$

   The space increment along the x axis is obtained from the time increment via the constant HT frame velocity $d\xi = -\boldsymbol{v_{HT}} \cdot \boldsymbol{\hat{x}_R} \, dt$, as mentioned.

2. A scatterplot of the transverse pressure $p_t(x,0) = p(x,0) + \frac{B_z^2(x,0)}{2\mu_0}$ versus $A_z(x,0)$ is prepared. This is the one used to determine the axis orientation. Then, a combination of polynomials and/or exponential functions is used to fit this plot. Typically a polynomial of degree f_p is fitted into the scatter plot. Then, for the values of A_z lower and higher than the minimum and maximum measured values, exponential tails are added. These tails have the form $f(A_z) = Be^{Cx}$ with B and C determined so that the exponential and polynomial connect in a continuous and differentiable manner. Finally, the resulting function $p_t(A)$ is then differentiated to obtain the right-hand side of the GS equation.

3. Solve the GS equation, using the numerical GS solver, to reconstruct the transverse magnetic field map, that is, the contour plot of $A(x,y)$ in a rectangular domain.

   The numerical GS solver is based on the Taylor expansion of 2nd order of the magnetic potential $A_z(x,y)$ along y:

$$A_z(x, y \pm \Delta y) \simeq A_z(x,y) \pm \left(\frac{\partial A_z}{\partial y}(x,y)\right)\Delta y + \frac{1}{2}\left(\frac{\partial^2 A_z}{\partial y^2}(x,y)\right)(\Delta y)^2 \tag{4.34}$$

We note that $\frac{\partial A_z}{\partial y}(x,y) = B_x(x,y)$, which is initially known over the spacecraft trajectory. Plus, we can Taylor expand $B_x(x,y)$ and we obtain:

$$B_x(x, y \pm \Delta y) \simeq B_x(x,y) \pm \left(\frac{\partial^2 A_z}{\partial y^2}(x,y)\right)\Delta y \tag{4.35}$$

We observe that the two previous Taylor expansions depend on $\left(\frac{\partial^2 A_z}{\partial y^2}(x,y)\right)$, which we do not know a priori. We are not able to compute derivatives in the y-direction since initially we only know the magnetic field in the x-direction. The trick is to use the Grad-Shafranov equation:

$$\frac{\partial^2 A_z}{\partial x^2} + \frac{\partial^2 A_z}{\partial y^2} = -\mu_0 \frac{dP_t}{dA_z} \implies \frac{\partial^2 A_z}{\partial y^2} = -\frac{\partial^2 A_z}{\partial x^2} - \mu_0 \frac{dP_t}{dA_z} \qquad (4.36)$$

In this way, we know all the unknowns and can proceed to recover $A_z(x, \pm\Delta y)$, and then $A_z(x, \pm 2\Delta y)$ and so on until the whole domain is covered.

Since B_z is only a function of A, the axial field distribution, can be obtained by evaluating a fitting function $B_z(A)$ of the measured $B_z(x, 0)$ versus $A(x, 0)$, over the whole domain.

Numerical issues

If no filtering is applied to the numerical scheme to solve for $A_z(x, y)$ described in section 4.4.2, the reconstructed magnetic potential $A(x, y)$ diverges for increasing values of $|y|$. In order to get rid of this problem, we will filter the reconstructed magnetic potential at each iteration. As proposed (Hau and Sonnerup, 1999), we filter the solution A_z using the following 3-point average filter:

$$\bar{A}_i = w(y)A_i + \frac{1}{2}(1 - w(y))(A_{i-1} + A_{i+1}) \qquad (4.37)$$

The same filter is applied to B_x and $\frac{\partial^2 A_z}{\partial x^2}$ at every iteration.

The used weight function is:

$$w(y) = 1 - \alpha \left| \frac{y}{y_{max}} \right| \qquad (4.38)$$

Notice that $w(0) = 1$ and $w(y_{max}) = 1 - \alpha$. We choose α such that $w(y_{max}) \geq \frac{1}{3}$, that is, $0 \leq \alpha \leq \frac{2}{3}$. The case $\alpha = \frac{2}{3}$ would imply that for $y = \pm y_{max}$, the averaging filter would weight the neighbours of A_i with the same weight as itself: $\frac{1}{3}$.

The frequency response of such a filter is:

$$H(e^{j\Omega}) = \frac{1}{2}(1 - w(y))e^{j\Omega} + w(y) + \frac{1}{2}(1 - w(y))e^{-j\Omega} \qquad (4.39)$$

We are especially interested in the modulus of the transfer function on the filter. We have plotted it for different values of $w(y)$. We have also plotted the cutoff frequency (frequency at which $H(e^{j\Omega}) = \frac{1}{\sqrt{2}}$ as a function of the weight $w(y)$.
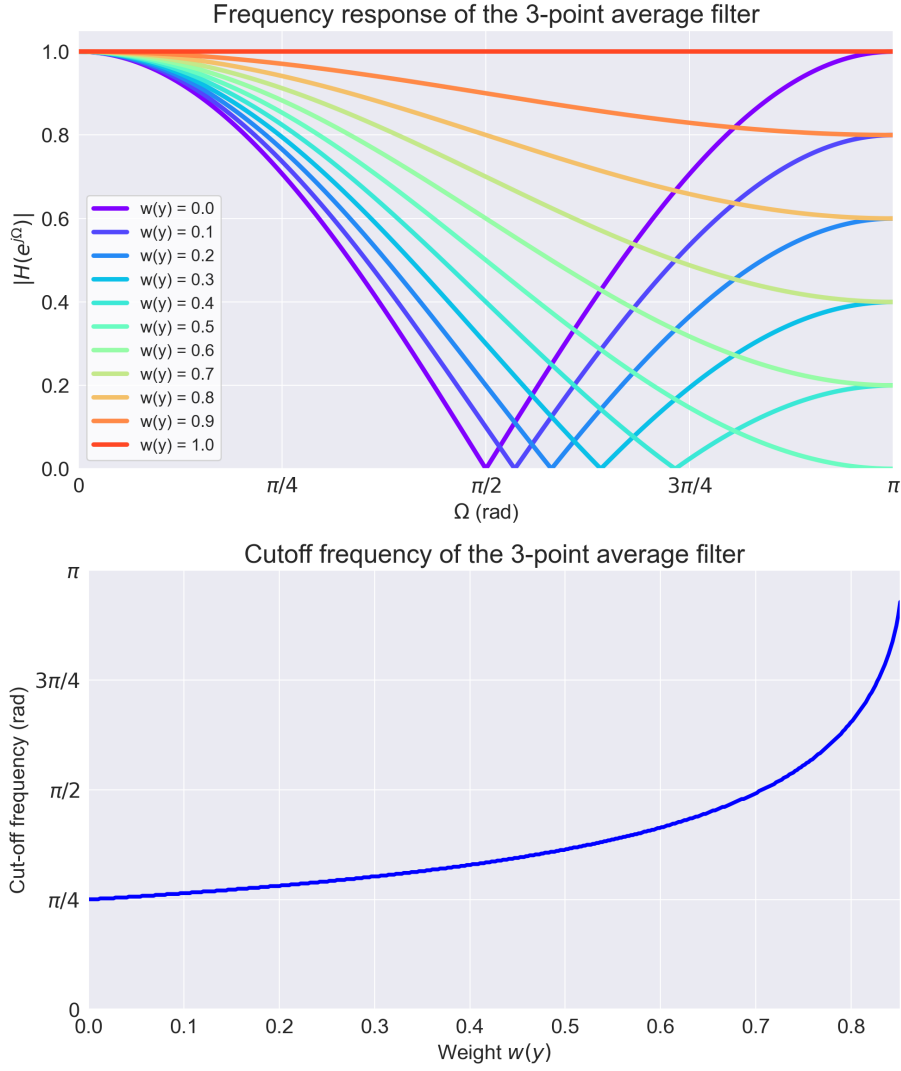
Figure 4.4: (Above) Frequency response (Fourier transform) of the 3-point average filter described in equation (4.37). (Below) Cutoff frequency for the different weights $w(y)$.

4.4.3   Derived physical magnitudes and geometrical parameters

Once the value of $A_z(x, y)$ has been reconstructed in the whole domain, we can calculate derived physical magnitudes in the cross-section of the MFR.

Magnetic field

The x component of the magnetic field $B_x(x, y)$ is calculated at each iteration of the numerical solving of the GS equation (see equation 4.35). The y component is calculated by taking the derivative of $A_z(x, y)$ with respect to x (and changing the sign), relation that can be seen in equation (4.4), that is, $B_y(x, y) = -\frac{\partial A_z}{\partial x}(x, y)$. Finally, the z component of the magnetic field is determined by evaluating the fitting function $B_z(A_z)$ in the solution $A_z(x, y)$.

From the three components of $\boldsymbol{B}(x, y)$ we can, of course, calculate its magnitude from: $\|\boldsymbol{B}\|(x, y) = \sqrt{B_x^2(x, y) + B_y^2(x, y) + B_z^2(x, y)}$.

Current density

We can calculate the current density using Ampère-Maxwell's law. In the exact same manner as in equation (4.4):

$$\boldsymbol{j} = (j_x, j_y, j_z) = \frac{1}{\mu_0} \boldsymbol{\nabla} \times \boldsymbol{B} = \frac{1}{\mu_0} \left(\frac{\partial B_z}{\partial y}, -\frac{\partial B_z}{\partial x}, \frac{\partial B_y}{\partial x} - \frac{\partial B_x}{\partial y} \right) \qquad (4.40)$$

We calculate the x and y components of the current density as:

$$\begin{cases} j_x(x,y) = \dfrac{1}{\mu_0} \dfrac{\partial B_z}{\partial y}(x,y) \\ j_y(x,y) = -\dfrac{1}{\mu_0} \dfrac{\partial B_z}{\partial x}(x,y) \end{cases} \qquad (4.41)$$

To numerically calculate the axial current density in the cross-section, we could use the expression given by (4.40). However we can use that $j_z(A_z) = \frac{dP_t}{dA_z}$ as has been shown in equation (4.12). Therefore, once we solve the GS equation and obtain $A_z(x,y)$ in the cross-section grid, we just have to evaluate $\frac{dP_t}{dA_z}$ in $A_z(x,y)$ to obtain $j_z(x,y)$. In short:

$$j_z(x,y) = \frac{dP_t}{dA_z}\left(A_z(x,y)\right) \qquad (4.42)$$

Lorentz force

The Lorentz force is calculated by doing the cross product of the current density $\boldsymbol{j}$ and the magnetic field $\boldsymbol{B}$ reconstructed in the MFR cross-section. As it can be deduced from equation (4.14), the Lorentz force should lay in the cross-section plane and does not have an axial component.

Radial, poloidal and axial components of the fields

Once we have the center of the MFR, we can define the cylindrical coordinates as defined in (3.1)) and the corresponding unit vectors as defined in (3.2).

For every point in the grid (x,y) we calculate its distance to the center (x_c, y_c), that is, $r = \sqrt{(x-x_c)^2 + (y-y_c)^2}$. Then $\hat{\boldsymbol{e}}_r = (\cos\varphi, \sin\varphi, 0) = \left(\dfrac{x-x_c}{r}, \dfrac{y-y_c}{r} \right)$ and similarly, $\hat{\boldsymbol{e}}_\varphi = (-\sin\varphi, \cos\varphi, 0) = \left(-\dfrac{y-y_c}{r}, \dfrac{x-x_c}{r} \right)$.

Then, for each of the fields: $\boldsymbol{B}$, $\boldsymbol{j}$ and $\boldsymbol{F}$ we can perform a change of coordinates from Cartesian to cylindrical, as shown below for the magnetic field:

$$\begin{cases} B_r = \boldsymbol{B} \cdot \hat{\boldsymbol{e}}_r = B_x \cos\varphi + B_y \sin\varphi \\ B_\varphi = \boldsymbol{B} \cdot \hat{\boldsymbol{e}}_\varphi = -B_x \sin\varphi + B_y \cos\varphi \\ B_z = B_z \end{cases} \qquad (4.43)$$

Twist

The twist per unit length, that is, the angle a magnetic field line turns around the MFR axis per unit of axial length, cannot be calculated as in equation (3.13). This expression is only valid in a circular-cylindrical configuration. To calculate the twist per unit length we will follow these steps:

1. Select an initial point of the cross section (x_0, y_0).

2. Calculate the magnetic field at this point: $\boldsymbol{B}(x_0, y_0)$.

3. Use the normalized magnetic field at this point $\hat{\boldsymbol{B}} = \frac{\boldsymbol{B}}{\|\boldsymbol{B}\|}$ and a step Δl to calculate a new point $(x_0 + \hat{B}_x \Delta l, y_0 + \hat{B}_y \Delta l, \hat{B}_z \Delta l)$.

4. Project this point into the x-y plane to calculate the magnetic field at this point.

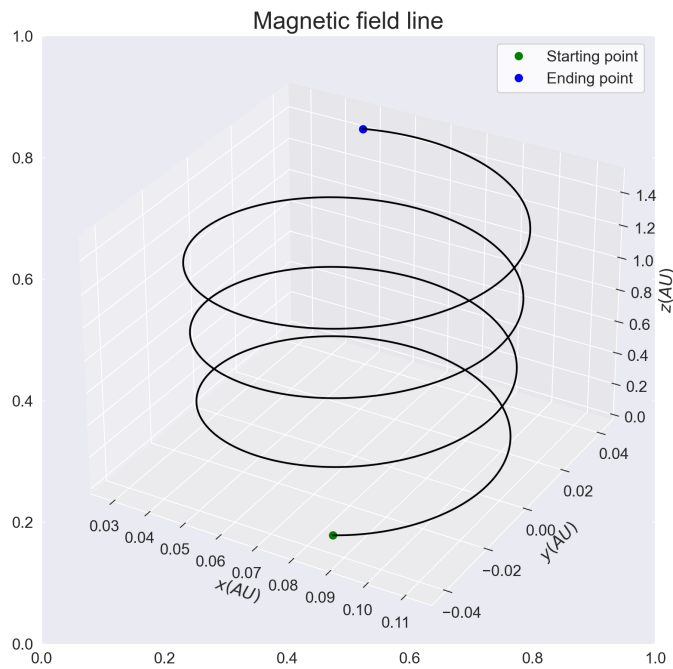5. Repeat step 3 and 4 a given number of iterations.

Figure 4.5: Reconstructed magnetic field line from the reconstructed cross-section of the CC model. The twist can be calculated from the number of turns and distance travelled in the z direction.

In this way, we can recover the magnetic field line starting at the point (x_0, y_0) and determine the angle turned around the MFR axis. Finally, we have to divide this angle by the total axial distance covered.

Center of the MFR and impact parameter

We define the center of the MFR as the position of the maximum of the axial magnetic field B_z. We define the impact parameter y_0 as the distance in the y-direction from the center to the spacecraft trajectory.

Distortion and rotation

The reconstructed cross-section, in real event analysis, is not circular. It tends to be distorted, more like an ellipse. Usually, this distortion is in the direction of propagation of the ICME. In

order to quantify the distortion, we fit ellipses to the level curves of the $B_z(x, y)$ plot. We do this for different B_z values, resulting in ellipses of various dimensions.

Each fitting of an ellipse provides a minor and major semiaxis, from which we can calculate a distortion $\delta = \frac{a}{b}$. It also provides the angle of rotation of the ellipse ξ.
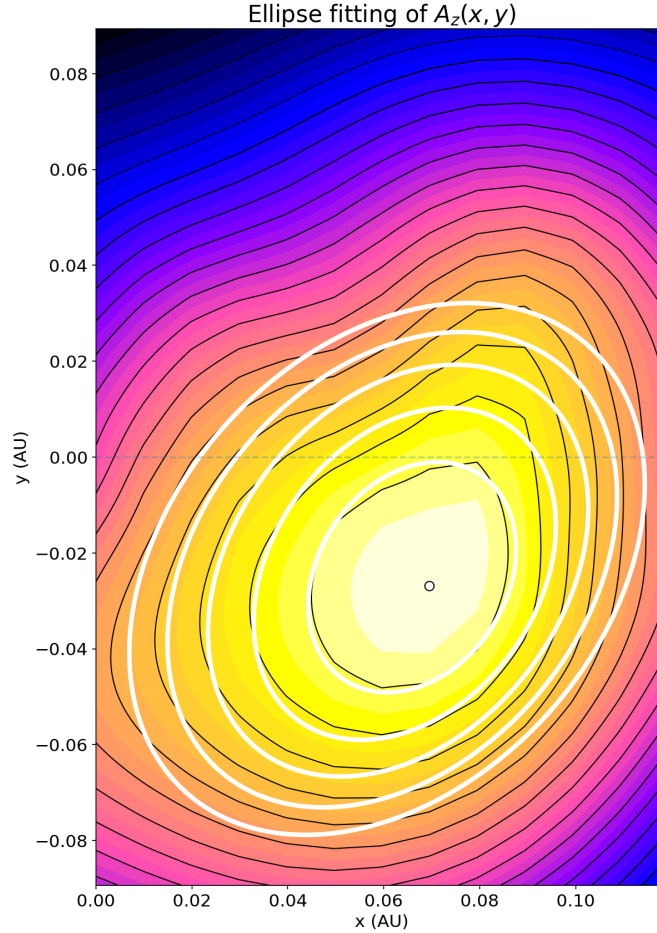

Figure 4.6: Ellipse fitting (white) of the cross-section of $A_z(x, y)$ for the 23 May, 2007 event analysed in chapter 6.

4.5   Python implementation

GSRT tools have been previously developed by other scientists. The most relevant one was coded using `Matlab` and included a GUI (Graphical User Interface). It was created by Christian Möstl and Charles J. Farrugia, based on the code of Qiang Hu. This code can be found in the following GitHub repository: C. Möstl's GitHub repository.

As we mentioned, the code was written in `Matlab`, which is not an open source programming language. We could never get this code working, even after numerous attempts. We also found the programs to be unnecessarily complex and long, making the task of understanding the code almost impossible.

Recently, the scientific community is switching to `Python`, for it being very powerful, easy-to-use and open-source. This is why we decided to implement our own GSRT using `Python`. The aim was to provide the Heliophysics Science Department (HSD) of NASA GSFC with a tool to analyze events. This tool has been made public in order to be used by any member of the scientific community.

Most of the time and effort dedicated to this thesis has been into coding the reconstruction technique. Our implementation of the GSRT can be found in Jordi Jumilla's GitHub repository.

The code automatically downloads all the generated plots and writes the results in a log file.

4.6   Benchmark

In order to test the GSRT and determine the optimal parameters for the reconstruction, we will study different benchmark cases.

4.6.1   Exponential benchmark

This benchmark case was first presented by (Hau and Sonnerup, 1999). The laplatian of A_z is:

$$\nabla_\perp^2 A_z = \frac{\partial^2 A_z}{\partial x^2} + \frac{\partial^2 A_z}{\partial y^2} = e^{-2A_z} \tag{4.44}$$

The right-hand side of the previous equation, according to the GS equation, should be equal to $-\mu_0 \frac{d}{dA}(p + \frac{B_z^2}{2\mu_0})$, and therefore we obtain the following expression relating the z-component of the magnetic field B_z and the pressure:

$$\frac{B_z^2(A)}{2} = \frac{e^{-2A}}{2} - \mu_0 p(A) \tag{4.45}$$

In principle we could choose whatever $B_z(A)$ and $p(A)$ functions that fulfill the previous relation. However, we have to impose that the pressure is non-negative. By doing this we obtain the following inequalities that must be fulfilled for every value of A:

$$\begin{cases} 0 \leq p(A) < \frac{e^{-2A}}{2\mu_0} \\ 0 < |B_z(A)| < e^{-A} \end{cases} \tag{4.46}$$

Any dependence of the pressure and z component of the magnetic field that fulfills equation (4.45) and the previous conditions (4.46) will have the following solution

$$A(\tilde{x}, \tilde{y}) = \ln\left(\alpha \cos(\tilde{x}) + \sqrt{1 + \alpha^2} \cosh(\tilde{y})\right) \tag{4.47}$$

We can compare the results of the GSRT to the above equation that describes the analytical solution of the GS equation.

4.6.2   CC and EC models as benchmark

The CC and EC models have been used as benchmarks to test the validity of our implementation of the GSRT. These models have also been used to test the performance and limitations of the GSRT in section 5.

4.7 GSRT for multi-spacecraft measurements

In some cases, the same ICME is crossed by more than one spacecraft. These kind of events are ideal since more information can be extracted from them. The GSRT as described here only allows for single spacecraft measurements as a boundary condition of the GS equation. Much effort has been put into generalizing the GSRT to allow for multi-spacecraft measurements.

A common approach is to perform the reconstruction using just the data from one of the spacecraft, and obtain multiple reconstructions of the cross-section of the MFR, for different parameters of the reconstruction. For each reconstructed cross-section, we can calculate the magnetic field that the second spacecraft would have measured according to that reconstruction. By selecting the parameters that provide a better fitting for the measured magnetic fields of the second spacecraft we can take into consideration the measurements of both spacecraft.

An example of this happened on 23 May 2007 event, which was measured by STEREO A and Wind simultaneously. A reconstruction combining the measurements of the two spacecraft was made by (Möstl et al., 2009).
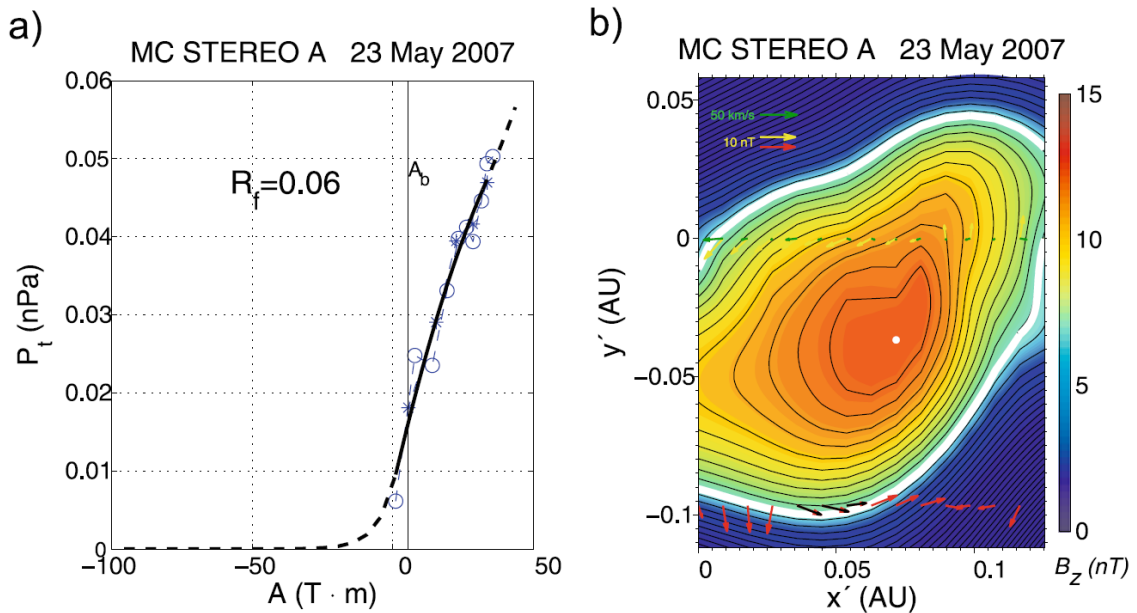

Figure 4.7: Reconstruction results for the 23 May 2007 event. (Left) Plot of the transverse pressure p_t vs $A(x, 0)$. (Right) Reconstructed axial magnetic field B_z in the MFR cross-section. The trajectory of STEREO A is at $y' = 0$ and the one of Wind spacecraft is at around $y' \simeq -0.1$ AU. Retrieved from: Möstl et al. (2009).

Figure 4.7 (right) shows the reconstructed axial magnetic field B_z in the MFR cross-section. The yellow and green arrows at $y' = 0$ correspond to the measured magnetic field and plasma velocity of STEREO A; whereas the red arrows at $y' \simeq -0.1$ AU correspond to the measured magnetic field of Wind. As it can be appreciated, the Wind mission slightly crossed the ICME near its boundary. The magnetic field measurements of Wind were used to optimize the reconstruction made using STEREO A measurements.

This event is analysed using our implementation of the GSRT and measurements of STEREO A in section 6 using only the measurements from STEREO A.

Another interesting application of GSRT for multi-spacecraft measurements is for the *Cluster* mission. This mission is composed of 4 spacecraft orbiting the Sun together with inter-spacecraft distances ranging from 600 to 20000 km. In this direction, we have collaborated with Marcel Ayora, doing his Bachelor's thesis at NASA GSFC as well, in his work to calculate current densities profiles inside MFRs using a 4-spacecraft configuration like Cluster. We provided him with the

reconstructed parameters using our GSRT from simulated data of a MFR crossed by 4 spacecraft in a tetrahedral configuration, which he then used in his research.

4.8   GSRT for toroidal geometry

New variations and improvements of the GSRT have been carried out in the recent years. In 2017, Dr. Qiang Hu presented a significant variation using toroidal geometry instead of cylindrical (Hu, 2017a), (Hu, 2017b). Some work was also done in the same direction by (Skan, 2019).

The use of toroidal geometry opens the possibility of the MFR axis to be curved. However, it assumes that there is no azimuthal variation $\frac{\partial}{\partial \varphi} = 0$. Following the notation introduced in chapter 3, it corresponds to circular-toroidal geometry.
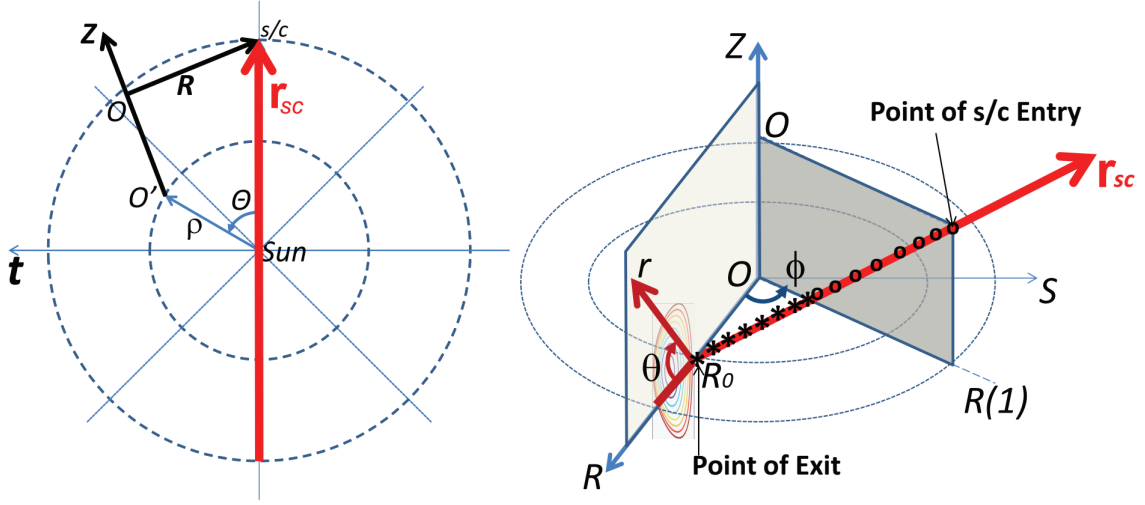

Figure 4.8: Scheme of the crossing of a spacecraft (s/c) through the toroidal magnetic flux rope. Retrieved from: Hu (2017a).

The toroidal GSRT is capable of analyzing the data for cases that the straight MFR axis cannot be assumed, such as CMEs with a radius so small that their curved geometry cannot be ignored or if the spacecraft passes the ICME through its leg Skan (2019). The toroidal GS equation originally comes from tokamak plasma theory and takes the following form (using cylindrical coordinates):

$$r \frac{\partial}{\partial r} \left(\frac{1}{r} \frac{\partial \Psi}{\partial r} \right) + \frac{\partial^2 \Psi}{\partial z^2} = -\mu_0 r^2 \frac{dp}{d\Psi} - F \frac{dF}{d\Psi} \tag{4.48}$$

Where p is the plasma pressure, Ψ is the poloidal flux function and $F = rB_\varphi$ is the poloidal current. The derivation of equation (4.48) can be found in the Annex.

5. GSRT performance and limitations

After testing our code with the different benchmarks presented in section 4.6, we proposed three different cases in order to study the performance and limitations of the GSRT. We simulated the crossing of a spacecraft through a magnetic flux rope whose fields are described by the CC and EC models (studied in detail in sections 3.1.4 and 3.2.1, respectively). We processed the synthetic data, analyzed it with the GSRT and compared the reconstructed fields and parameters with the ones used for the simulation (input parameters).
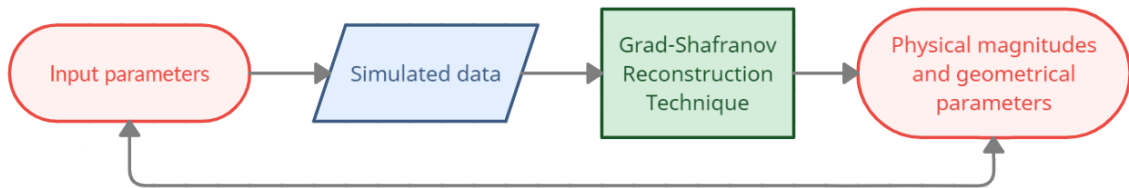

Figure 5.1: Flowchart of the simulation process we follow in the three cases presented in this section.

In all three cases, $n_x = 21$ magnetic field measurements were used and no noise was added to the simulated data. For this reason, the use of the filter detailed in section 4.4.2 was not needed. Also, on all three cases, the solution of the GS equation in the cross-section is calculated without adding the exponential tails in the transverse pressure p_t vs A_z plot (even if we show them in the plots). The reason for this is that the pressure for the CC and EC model can be determined except for an offset. Therefore, it makes no sense to add the exponential tails, especially the lower one.

The code used to simulate the magnetic field measurements can be found in Jordi Jumilla's GitHub repository under the name `ec_model.py`.

5.1 Case 1: Circular MFR with impact parameter

In this first case, we assumed that the MFR, with magnetic field distribution given by the CC model, was circular and its axis was lying on the y axis. A spacecraft then crossed such MFR with an impact parameter $y_0 = 35\%$ of its radius. The simulation aimed to determine the influence of the impact parameter on the quality of the reconstruction. A scheme of the trajectory of the spacecraft across the MFR is shown in figure 5.2.
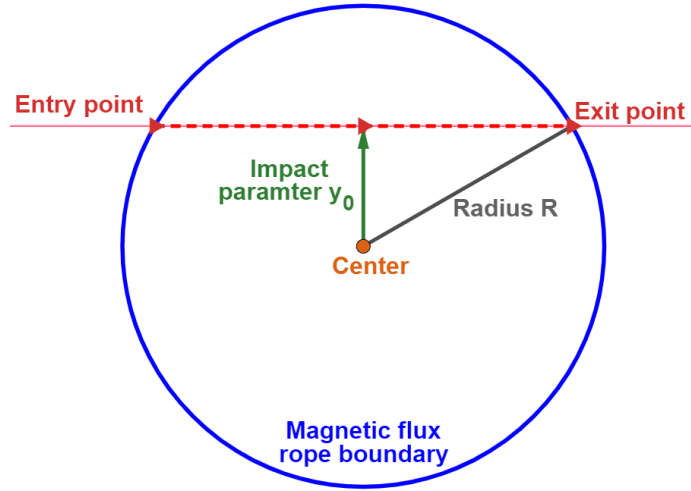
Figure 5.2: Scheme of the crossing of the spacecraft through the circular MFR, with a certain impact parameter y_0.

The parameters of the CC model used in the simulation are the following:

1. **Input parameters (CC model)**

Field parameters	Geometrical parameters
$n = 1$, $m = 0$. $\tau = 1.3$, $C_{10} = 1$, $B_z^0 = 10$ nT. - Chirality: left-handed (-1).	- Orientation $\phi = 90°$, $\theta = 90°$ (MFR laying on the y axis). - Radius $R = 0.07$ AU. - Impact parameter $y_0 = 35\%$ of the radius. - Relative speed spacecraft-MFR: $u_s = 450.$ km/s

2. **Simulated data**

Figure 5.3 shows the simulated synthetic data of the magnetic field strength and components. Based on the parameters selected, the duration is 12.1 hours and the B_n component displays the full rotation from south (negative values) to north (positive values). The maximum in the magnetic field strength is $\sim$9 nT since the spacecraft does not cross the MFR through the center. This corresponds to the MFR signatures 2 and 1, respectively, introduced in chapter 3.
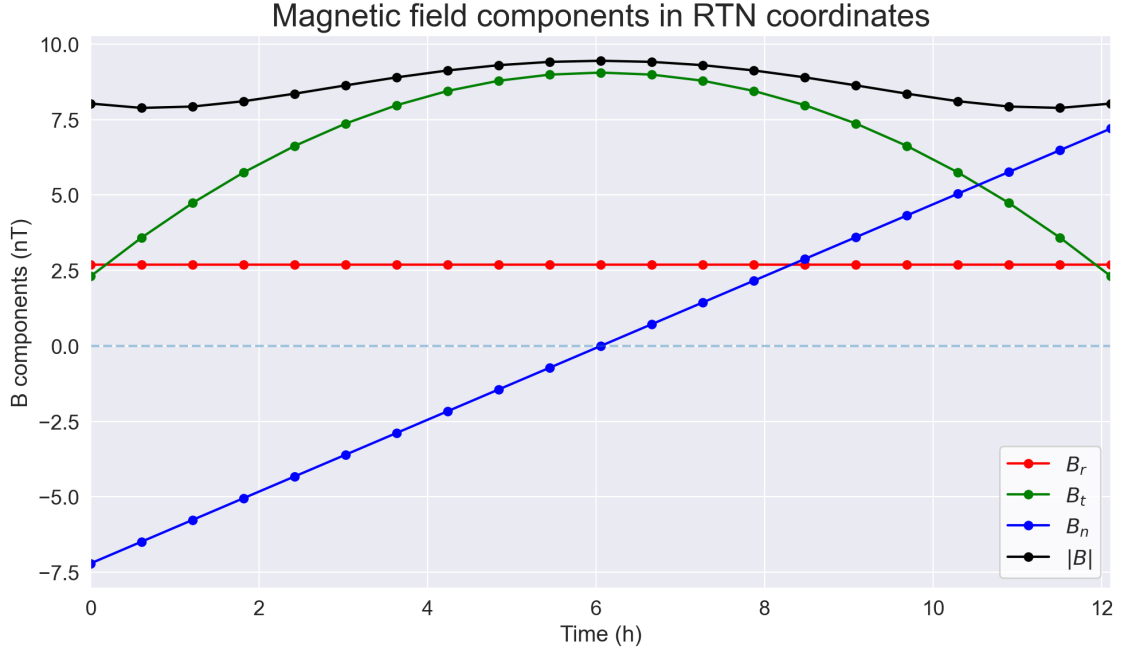
Figure 5.3: Simulated magnetic field strength and components measured by the spacecraft inside the MFR given by the CC model.

3. **Grad-Shafranov Reconstruction Technique:**

Figure 5.4 displays, from the top, the pressure profiles, magnetic potential, fitting of B_z vs A_z and p_t vs A_z. These plots are needed for the GSRT. In the first plot, the pressure profiles inside the MFR along the spacecraft trajectory are shown. One can distinguish between the plasma pressure (in red), the total magnetic pressure (in blue), the transverse magnetic pressure (in green) and the total transverse pressure, which is the sum of the plasma pressure and the transverse magnetic pressure (in black). As expected, pressures are maximum at the point of the closest approach to the axis. In the second plot, $-B_y(x,0)$ is integrated to obtain $A_z(x,0)$ against x. The obtained profile corresponds to a parabola, which is in agreement with equation 3.26. In the third plot, the fitting of the axial magnetic field $B_z(x,0)$ against $A_z(x,0)$ is done. The relation is linear since B_z grows with $r^{n+1} = r^2$ and A_z depends on $r^{m+2} = r^2$ (see equations 3.20 and 3.26). Finally, the fourth plot shows the dependence of the transverse pressure p_t versus A_z. A fitting is done and exponential tails added. This plot is then differentiated and used to calculate the non-homogeneous part (right-hand side) of the GS equation (equation 4.19).
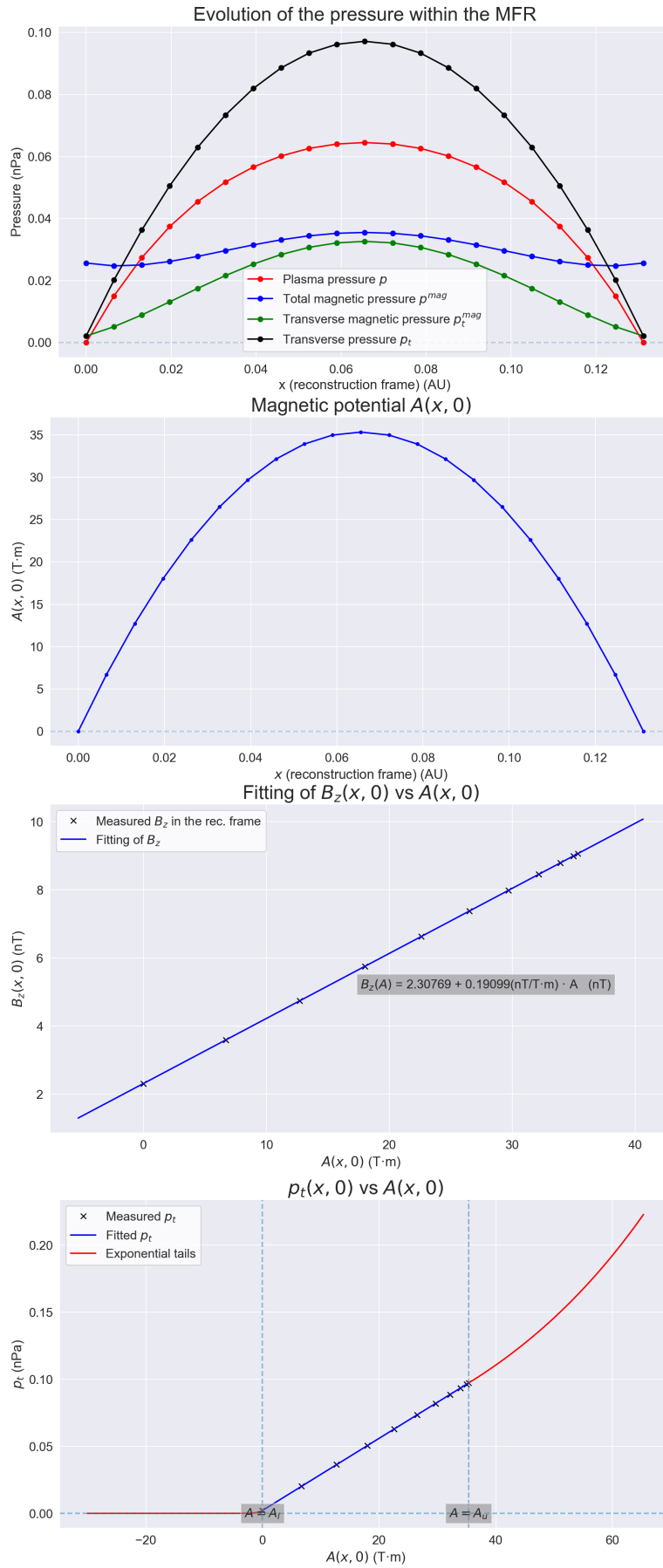
Figure 5.4: From the top: pressure profiles, magnetic potential, fitting of B_z vs A_z and p_t vs A_z for the case 1 study.

4. **Results of the GSRT applied to the CC model**

The reconstruction of the magnetic fields can be seen in figure 5.5. At a glance, the reconstructed magnetic field is circular and is in agreement with the used CC model. The error in the magnetic field components is less that 0.1% inside the MFR boundaries.

Output parameters:

- Axis orientation: $\varphi = 90°$, $\theta = 90°$.

- Maximum axial field: $\tilde{B}_z^0 = 9.9999$ nT.

- Impact parameter: $\tilde{y}_0 = 0.02393$ AU, corresponding to 34.191% of the radius R.

- Axial current density: $J_z(x, y)$ was constant and equal to 1.169 pA/m^2.

The recovery of the orientation of the MFR axis was done using the minimum residue method recovered the MFR axis orientation with total exactitude. The residue map has a very distinguished minimum at the mentioned angular coordinates. The axial field at the center (or maximum axial field) of the reconstructed cross-section turned out to be less than 0.0001% off the correct value of 10 nT. As for the impact parameter, the reconstruction gave a minimum distance of the spacecraft to the axis of around 34.2% of the radius, which is very close to the 35% used as an input parameter. Finally, as for the axial current density, the result matched almost perfectly the theoretical value.
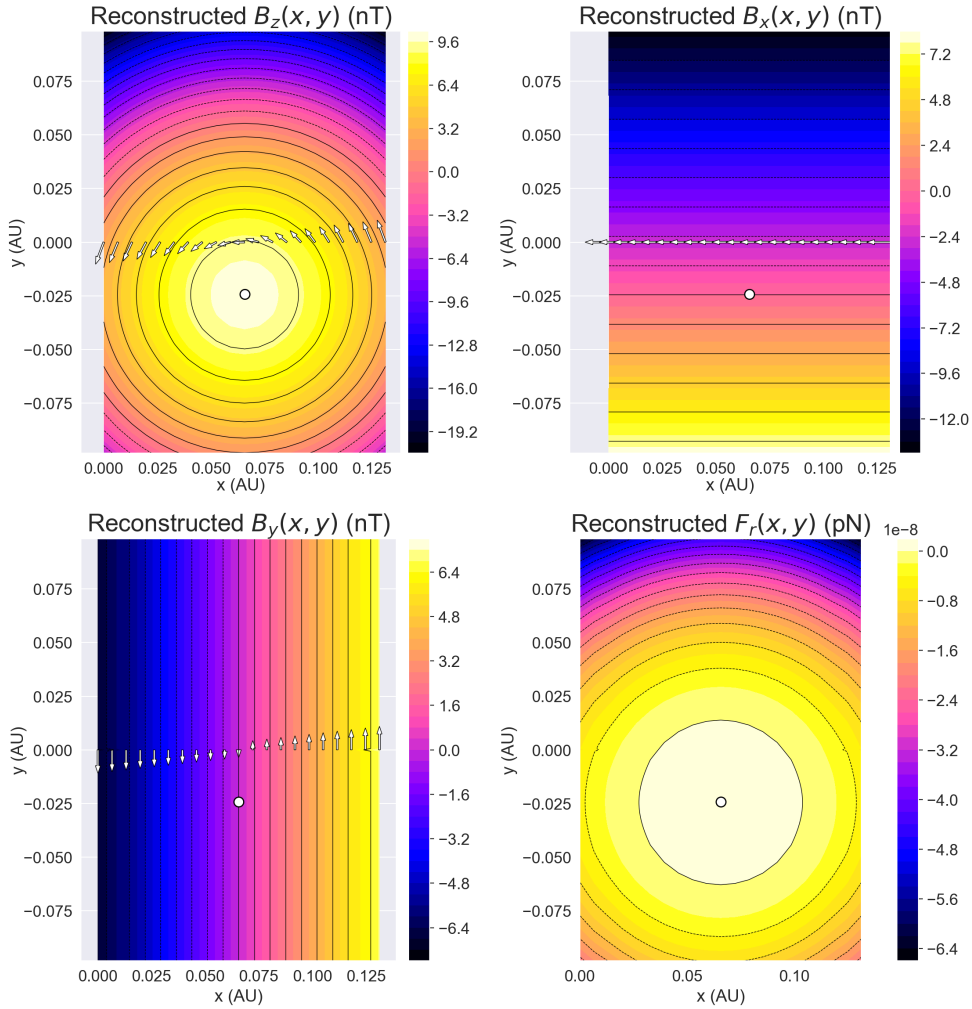

Figure 5.5: At the top-left, the reconstructed magnetic field B_z, at the top-right, B_x, at the bottom-left B_y and at the bottom-right, the radial Lorentz force F_r in the MFR cross-section.

5.2 Case 2: EC with distortion

In this second case, we also assumed that the MFR was circular and its axis was lying on the y axis. A spacecraft then crossed such MFR through its center (with an impact parameter $y_0 = 0$). The aim of this simulation was to determine whether the GSRT could account for distortion in the perpendicular direction of its motion. A scheme of the trajectory of the spacecraft across the MFR is shown in figure 5.6.
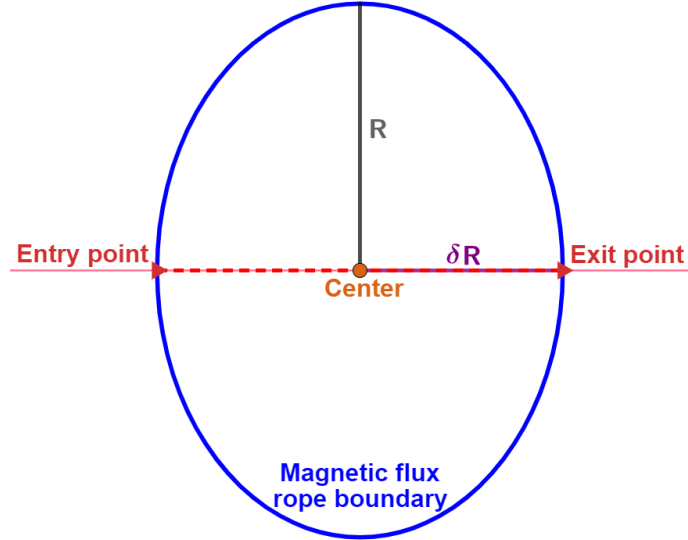

Figure 5.6: Scheme of the crossing of the spacecraft through the center of an elliptical MFR.

The parameters of the EC model used in the simulation are the same as the ones used in Case 1, except for the highlighted geometrical parameters.

1. **Input parameters (EC model)**

Field parameters	Geometrical parameters
 • $n = 1$, $m = 0$. • $\tau = 1.3$, $C_{10} = 1$, $B_z^0 = 10$ nT. • Chirality: left-handed (-1).	 • Orientation $\phi = 90°$, $\theta = 90°$ (MFR laying on the y axis). • Distortion $\delta = 0.75$, ellipse rotation angle $\xi = 0$ • Radius $R = 0.07$ AU. • Impact parameter $y_0 = 0$ • Relative speed spacecraft-MFR: $u_s = 450.$ km/s

2. **Simulated data**

Figure 5.7 depicts the simulated synthetic data of the magnetic field strength and components. Based on the parameters selected, the duration is 13 hours and the B_n component displays the full rotation from south (negative values) to north (positive values). The maximum in the magnetic field strength is ∼10 nT since the spacecraft crosses the MFR through the center. This corresponds to the MFR signatures 2 and 1, respectively, introduced in chapter 3.

Figure 5.7 depicts the simulated synthetic data that the spacecraft would measure when crossing a MFR with magnetic configuration given by Nieves-Chinchilla's EC model and the parameters indicated above. We can see that the radial component of the magnetic field B_r is constant and equal to zero. This is the case because the radial component is zero B_r and we cross the MFR through its center. The tangential component B_t has a maximum of 10 nT at 6.5 hours. As for the normal component B_n, it changes its sign from negative to positive.
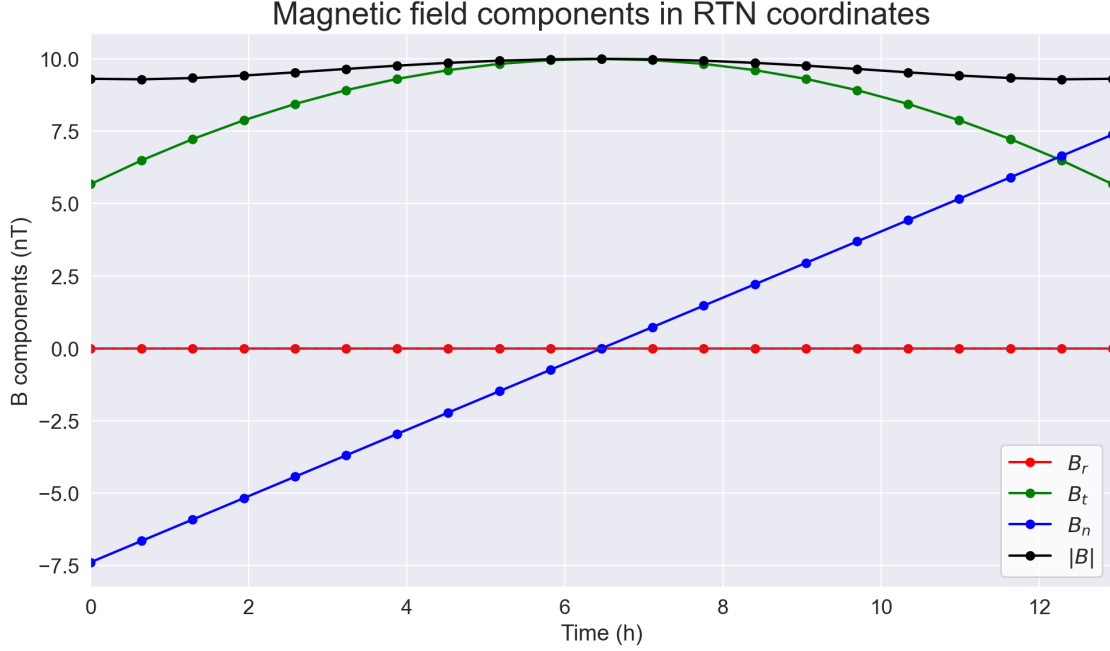

Figure 5.7: Simulated magnetic field strength and components measured by the spacecraft inside the MFR given by the EC model.

3. **Grad-Shafranov Reconstruction Technique**

The GSRT was applied in the exact same manner as in case 1.

4. **Results of the GSRT applied to the EC model**:

The reconstruction of the magnetic fields can be seen in figure 5.8. At a glance, the reconstructed magnetic field is elliptical and is in agreement with the used EC model. After a more detailed analysis, it is checked that the error in the magnetic field components is less that 0.1% inside the MFR boundaries.

Output parameters:

- Axis orientation: $\varphi = 90°$, $\theta = 90°$.
- Axial magnetic field at the center: $\tilde{B}_z^0 = 10.000$ nT.
- Impact parameter: $\tilde{y}_0 = 0$ AU.
- Axial current density: 0.885 pA/m^2.

The recovery of the orientation of the MFR axis was, again, done using the minimum residue method recovered the MFR axis orientation with total exactitude. The residue map has a very distinguished minimum at the mentioned angular coordinates. The axial field at the center (or maximum axial field) of the reconstructed cross-section gives the exact value 10 nT, since the impact

parameter is now zero. Finally, as for the axial current density, the result matched perfectly the theoretical value.
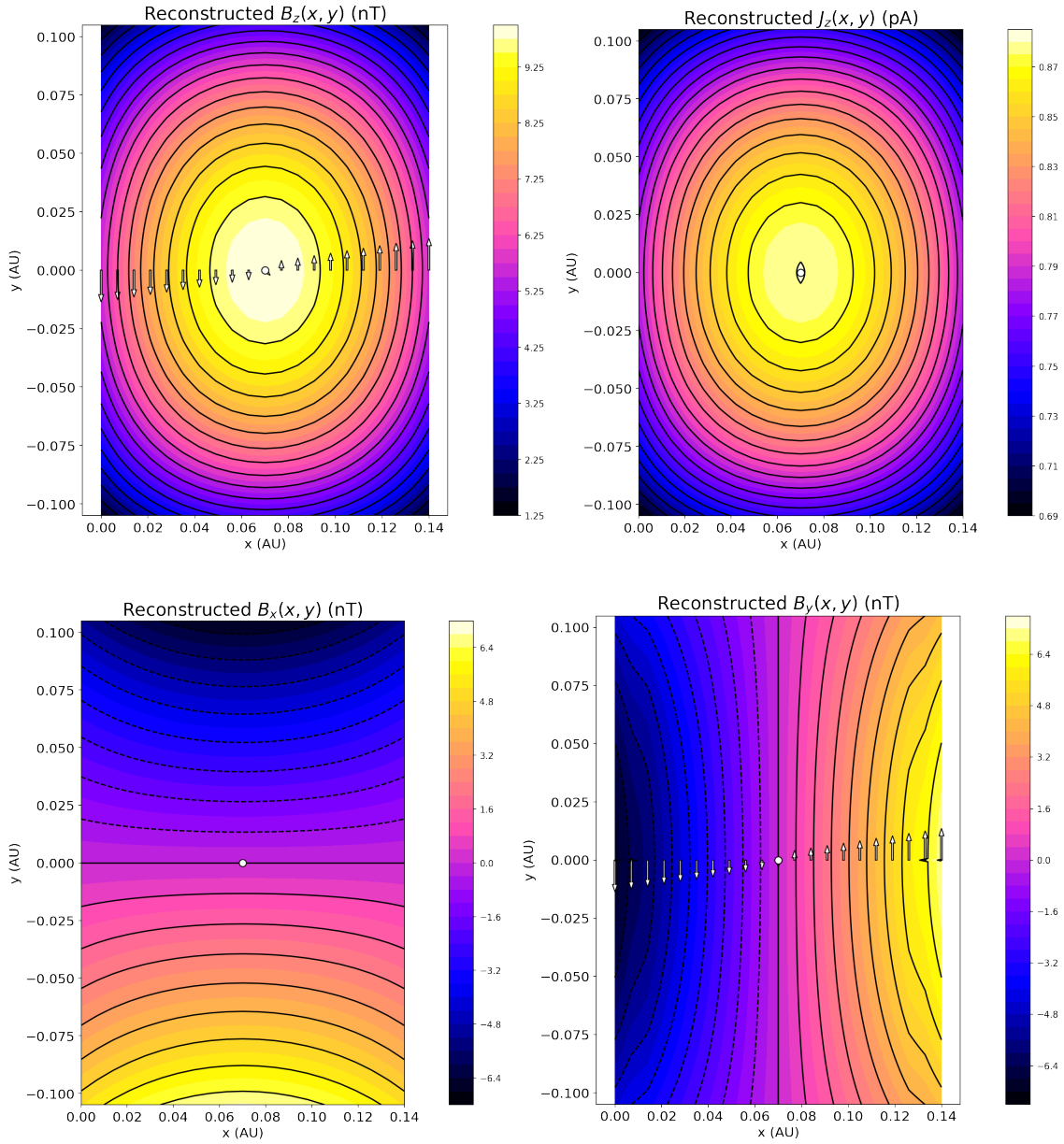
Figure 5.8: At the top-left, the reconstructed magnetic field B_z, at the top-right, the axial current density J_z, at the bottom-left B_x and at the bottom-right, B_y in the MFR cross-section.

5.3 Analysis of the distortion

The aim of this section is to determine whether the GSRT is able to reconstruct with fidelity flux ropes with distortion. In order to do so, we have repeated case 2 for values of the distortion δ ranging from 0.5 (elongated ellipse) to 1 (circle), as seen in the following figure.

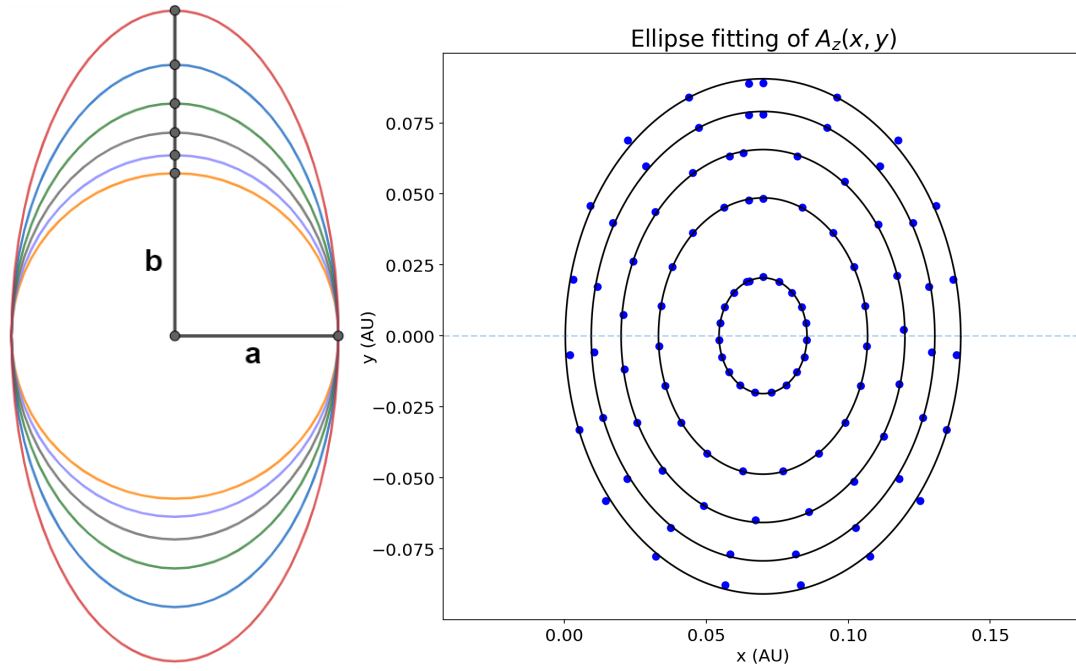**Figure 5.9:** (Left) Ellipses with distortions ranging from $\delta = 1$ (circumference) up to $\delta = 0.5$ (most elongated ellipse). (Right) Exapmle of ellipse fitting of the contour plot of $A_z(x, y)$.

We applied the GSRT to different flux ropes with distortion from 0.5 to 1 in steps of 0.05. The estimation is very good for $\delta = 0$, with a standard deviation of 0.1%. As we increment the distortion (decrease δ), the accuracy in the determination of δ decreases. Still for $\delta = 0.6$, the relative error is $(5.8 \pm 1.8)\%$. For a distortion of 0.5, the error in the distortion is more than 20%.
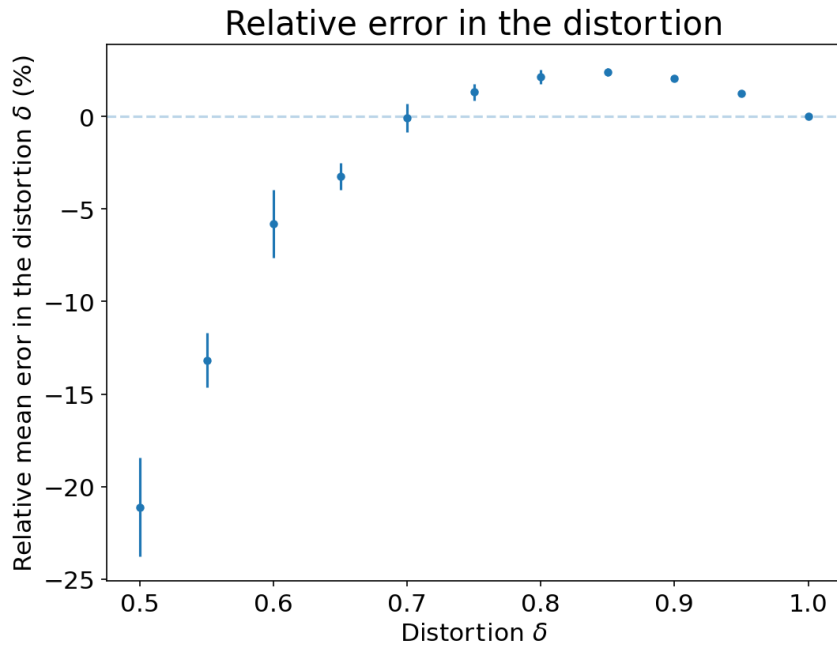

Figure 5.10: Relative error in the estimation of the ellipse distortion for different δ parameters of the EC model.

Therefore, we conclude that the GSRT is capable of determining the distortion of MFR with accuracy, up to distortions of $\delta = 0.6$.

6. Real Event Analysis

6.1 Magnetic Clouds Classification

There are multiple ways of cataloging MFR or Magnetic Clouds. In this section, we present the classification as according to Jian et al. (2006). This classification is based on the total transverse pressure profile inside the MC.

$$P_t = P_{mag}^\perp + P_{plasma} = \frac{B_z^2}{2\mu_0} + \sum_j n_j k_B T_{j\perp} \tag{6.1}$$

where the j index runs through all the different sorts of particles that compose the plasma. MCs were divided into three groups depending on the shape of the pressure profile along the spacecraft trajectory inside the magnetic cloud:

- **Group 1**: with a well-determined peak
- **Group 2**: with a plateau observed
- **Group 3**: characterized by decreasing pressure

These three groups correspond to a small, medium, and large impact parameters.

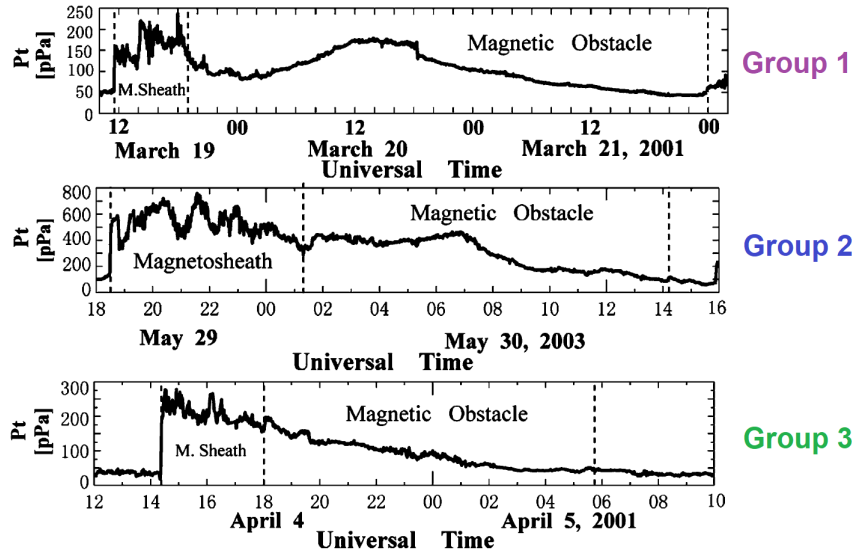**Figure 6.1:** Example of magnetic clouds of group 1 to 3, according to (Jian et al., 2006). Group 1 events present a well-determined peak, group 2 events present a plateau and group 3 a decreasing pressure profile. Adapted from: (Jian et al., 2006).

6.2 Analysis of the STEREO-A Event on 23 May 2007

In this section, we analyse the STEREO-A Event on 23 May 2008. This event has been previously analyzed by Christian Möstl et. al (Möstl et al., 2009). The Sun was in a period of low activity (solar minimum) at the date of the measurement of this magnetic cloud.

The start and end times of this event were determined by looking for flux-rope signatures in the measured data.

- Start time: 00:50:00 h

- End time: 12:14:00 h

- Total elapsed time: 11h 23 min

The measured data was resampled to $n_x = 13$ measurements using an averaging filter. In the reconstruction done by Möstl et al. (2009), the data is resampled to 15 points.
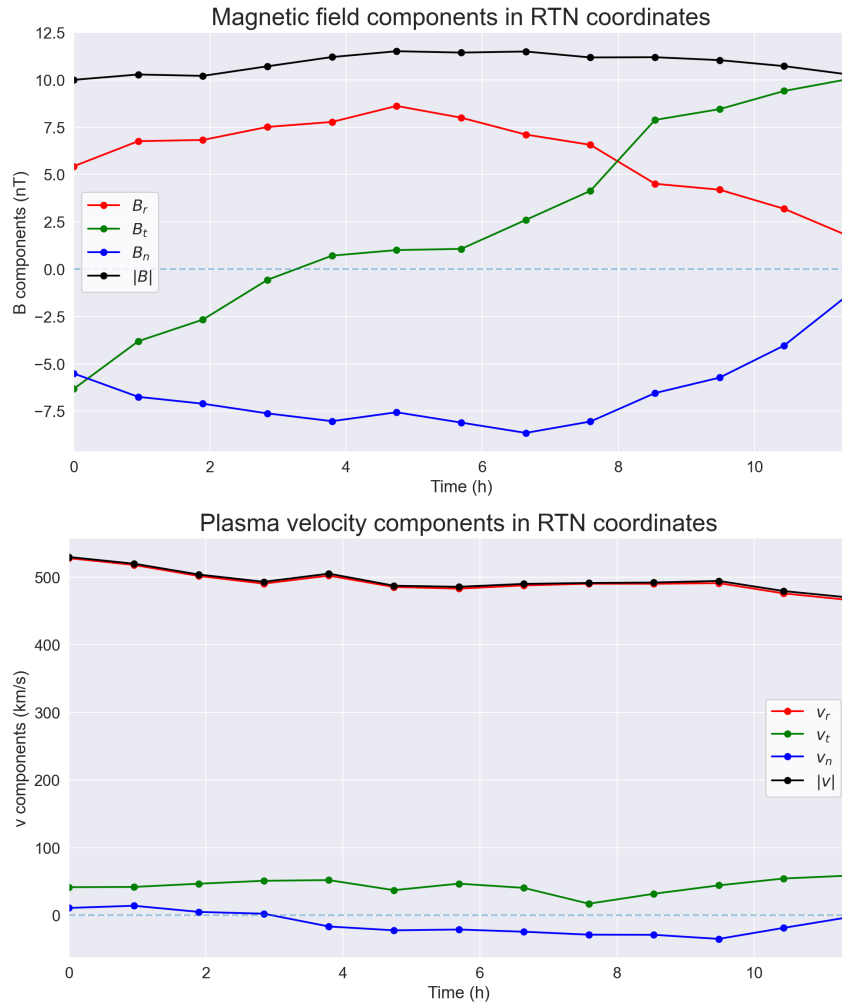

Figure 6.2: Magnetic field and plasma velocity measures by STEREO A during the event.

In figure 6.2 the measured magnetic field and plasma velocity in RTN coordinates are shown, as a function of the elapsed time. In the upper plot, we can see an increase in the magnitude of the magnetic field and a change of sign of the tangential coordinate. These correspond to MFR signatures.

59

In figure 6.2 (lower) we observe that the plasma velocity is mostly radial. We also observe that the plasma speed decreases over time. The first measurements that the spacecraft performs correspond to the leading edge of the IMCE whereas the last measurements correspond to the trailing edge. Since the leading edge speed is greater than the trailing edge speed, we conclude that the ICME is expanding. From figure 6.2 it is clear that this difference is small. The expansion speed is calculated as the speed difference divided by 2. This measures the speed at which each edge of the ICME is moving away from its center.

- Leading edge speed: $\|\boldsymbol{v_l}\| = 529.7$ km/s

- Trailing edge speed: $\|\boldsymbol{v_t}\| = 469.8$ km/s

- Expansion speed: $v_{exp} = \dfrac{\|\boldsymbol{v_l} - \boldsymbol{v_t}\|}{2} = 32.76$ km/s

The first step is to determine the DeHoffmann-Teller frame velocity. We did this by minimizing the modulus square of the convection electric field (4.25). We obtained a deHoffmann-Teller frame velocity (in RTN coordinates) of:

$$\boldsymbol{v}_{HT} = (487.4,\ 38.89,\ -11.27)\ \text{km/s} \tag{6.2}$$

It corresponds to a deHoffmann-Teller speed of $\|\boldsymbol{v}_{HT}\| = 491.20$ km/s, which is in agreement with the results of Möstl et al. (2009), where a speed of 493 km/s was obtained. The ratio of the expansion speed to the deHoffmann-Teller speed turns out to be: $v_{exp}/v_{HT} = 0.06669$, which makes evident the expansion of the flux rope mentioned previously.

The quality factor of the frame velocity is: $D(\boldsymbol{v}_{HT})/D(0) = 0.003341 \ll 1$, which is much smaller than one. A scatter plot of the components of the convection electric field calculated using the measured plasma velocity and using the HT velocity is done. A linear regression is performed, which gives a slope of 1.002 and an intercept of $3.323 \cdot 10^{-6}$ V/m. The correlation coefficient (cc) is of $R^2 = 0.9954$, which is very close to 1. Therefore, this confirms the existence and good quality of the HT frame.
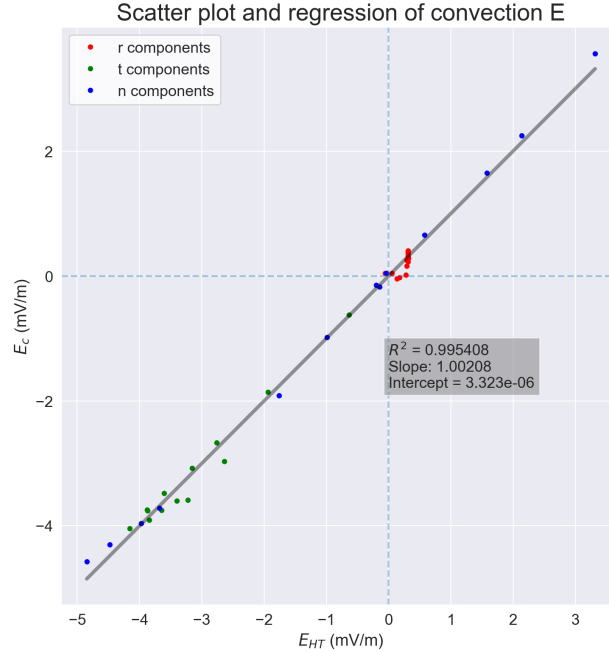

Figure 6.3: Plot of the convection electric field (calculated with the measured plasma velocity) versus the HT convection electric field. A linear regression is performed.

Once we know the frame velocity, we proceed to calculate the residual plasma velocity $\boldsymbol{v_{res}} = \boldsymbol{v} - \boldsymbol{v_{HT}}$. This represents the plasma speed as measured in the HT frame of reference. In figure 6.4, the evolution of this residual plasma velocity is shown as a function of time. One can see that most of the time the residual plasma speed is under 6% of the HT speed, which again shows the quality of the HT frame. One can also observe that the radial residual velocity is positive at first and then it becomes negative. This proves the fact that the ICME is expanding. An accelerating HT frame could be determined, which could account for the expansion of the ICME.
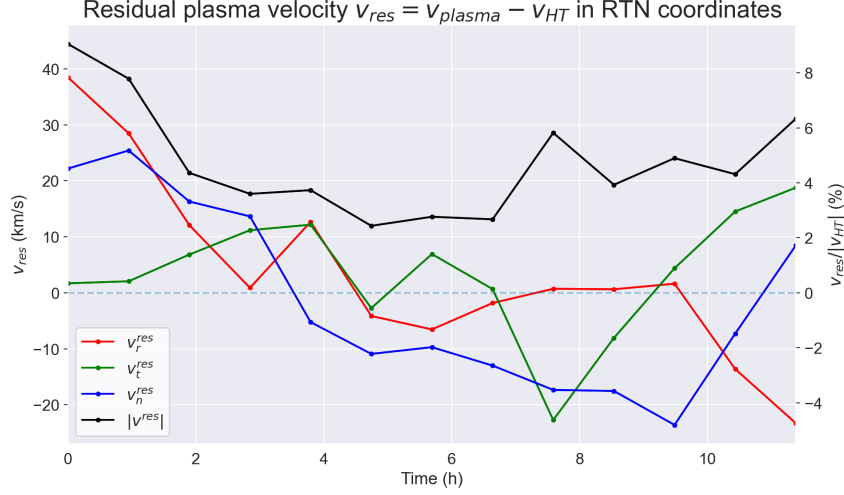
Figure 6.4: Residual velocity in RTN coordinates.

After calculating the deHoffmann-Teller velocity of the frame, the MFR axis orientation is determined. First, a minimum-variance analysis of the measured magnetic is done, which results in the following orientations.

- MVAB: $\varphi = 220.0°$, $\theta = 41.8°$

- MVUB: $\varphi = 221.0°$, $\theta = 39.7°$

The angle between the axis determined with the MVAB and MVUB is 2.2°, which denotes that both methods provide a very similar axis.

The minimum residue method is also applied and a residue map is created. The minimum residue direction corresponds to:

- Minimum residue direction: $\varphi = 220.0°$, $\theta = 32.0°$

The angle between the minimum residue direction and the MVAB or MVUB is less than 10°, meaning that the three methods agree on the axis orientation. The vector used as the axis for the reconstruction is the one given by the minimum residue, changing its sign to make the axial magnetic field positive.

With this, the length travelled by the spacecraft across the MFR is $x_{max} = 0.1201$ AU. The step between measurements in the x axis is $\Delta x = 0.0100$ AU.

A basis change is performed to the magnetic field vector. The magnetic field profile can be seen in the figure 6.5:
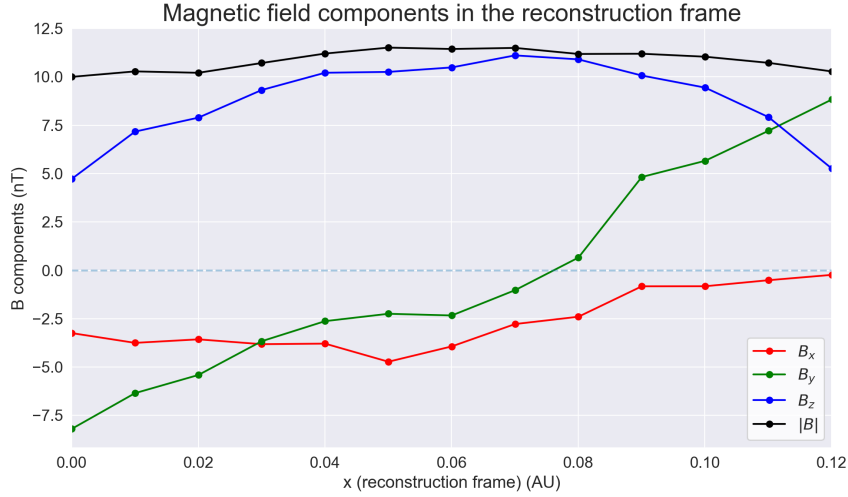
Figure 6.5: Magnetic field strength and components in the reconstruction frame.

We observe that the magnitude has not changed, the axial component has a maximum in between the center and the right end of the MFR. As for the y component, it has a sign change, as expected. Finally, the x component is small and remains negative and quite constant over time.

From the previous plot, as B_y changes from negative to positive while B_z is always positive, we conclude that the chirality of this flux rope is positive (right-handed). This is in agreement with Möstl et al. (2009).

Once we have the complete reconstruction frame, we proceed to calculate some of the magnitudes needed to numerically solve the GS equation in the cross-section. We start by taking a look at the z component of the magnetic potential, $A_z(x, 0)$. This has a maximum towards the right-hand side of the MFR and has a parabola-like shape. This is going to serve as a boundary condition to solve the GS equation.
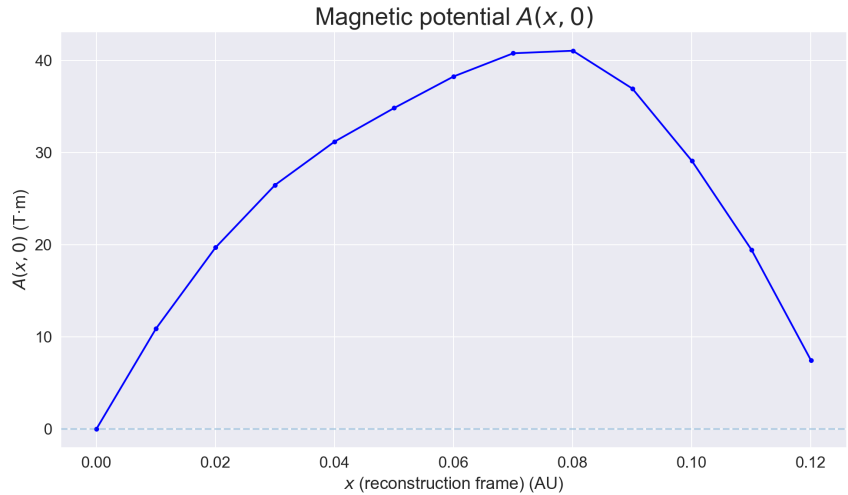
Figure 6.6: Axial component of the magnetic potential $A_z(x, 0)$ along the spacecraft trajectory.

After that, we proceeded to determine the relationship between the axial magnetic field B_z and A_z. As expected, this relation looks like a single-valued function and the relation between the two mentioned magnitudes is, approximately, linear. The obtained fitting line equation is:

$$B_z(A_z) = 4.875 + 0.153(\mathrm{nT/(T \cdot m)}) \cdot A_z \ (\mathrm{nT}) \qquad (6.3)$$
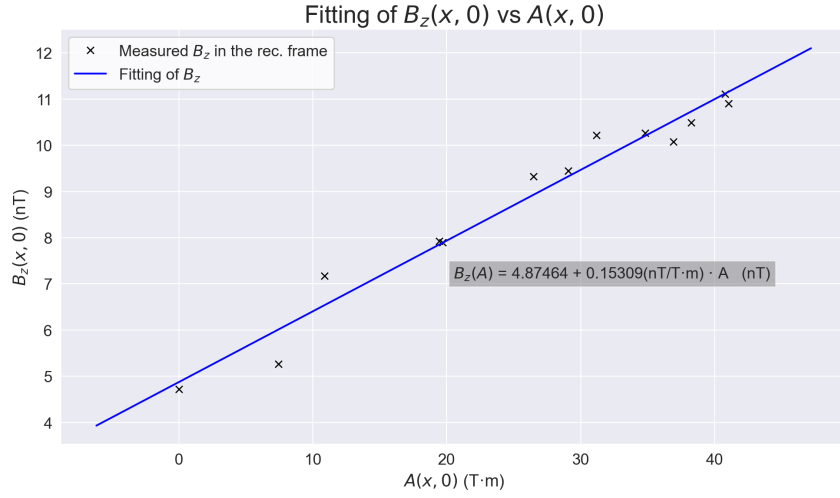
Figure 6.7: Magnetic field components in the reconstruction frame.

Finally, we studied the pressure evolution inside the flux rope, as shown in the next figure. We clearly see that the plasma pressure is much smaller than the magnetic pressure (upper plot), which implies that the beta parameter is small (lower plot). The beta parameter is lower than 0.06 throughout the whole flux rope. As for the transverse pressure, we observe that it has a well-defined maximum at around 0.08 AU. According to Jian's classification (section 6.1), it corresponds to a Group 1 magnetic cloud.
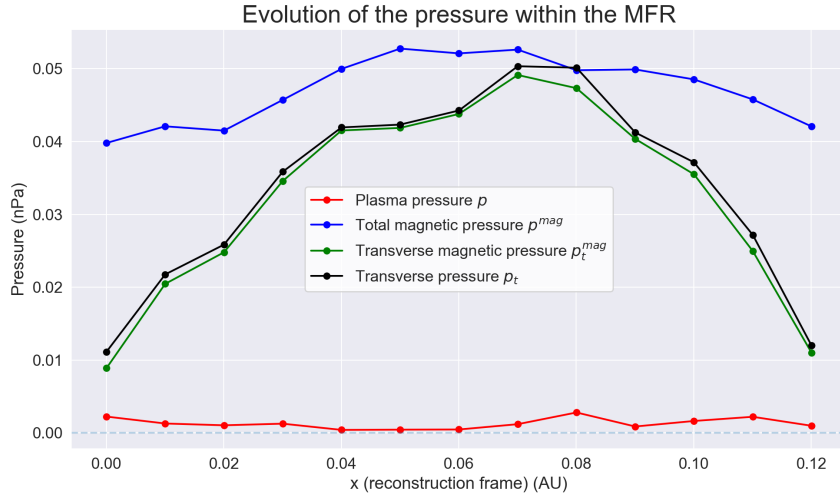
Figure 6.8: Evolution of the pressures along the trajectory of the spacecraft inside the MFR. The red line represents the plasma pressure, the green line the transverse magnetic pressure $B_z^2/2\mu_0$, the black line the total transverse pressure and the blue line the total magnetic pressure. The plasma pressure (red) is much smaller than the transverse pressure (black).
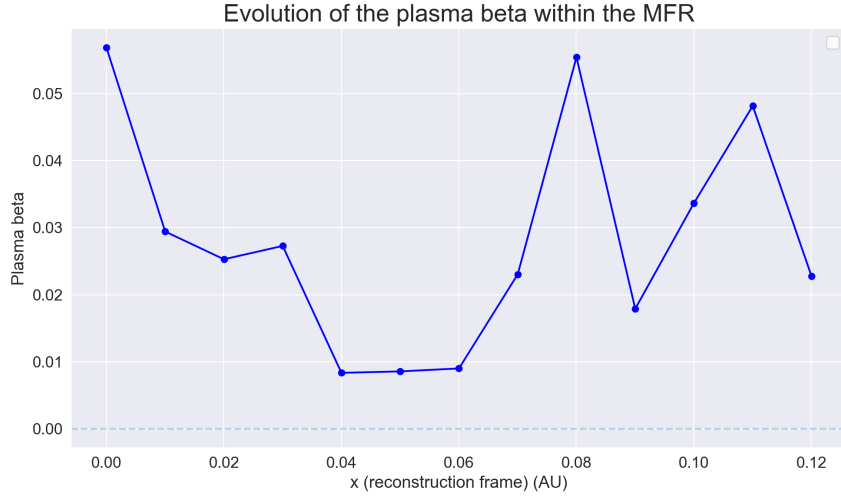
Figure 6.9: Evolution of the beta parameter along the trajectory of the spacecraft inside the MFR. It is lower than 0.06 throughout the whole flux rope, meaning that the magnetic forces are much greater than the fluid forces.

The relationship between the transverse pressure and the magnetic potential was determined. This turned out to be almost linear. We used a polynomial of degree $f_p = 2$ to fit the transverse pressure (blue). We then added exponential tails to both ends (red).
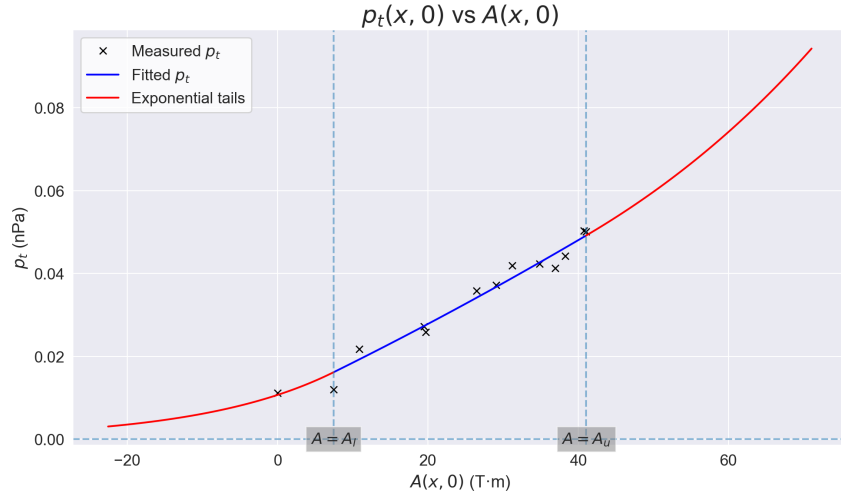
Figure 6.10: Transverse pressure versus $A(x,0)$. The measurements of STEREO A are represented with a white cross whereas the fitting between A_l and A_u is done by a degree $f_p = 2$ polynomial (blue line). Exponential tails (red) are used outside the interval $[A_l, A_u]$.

The previous plot is differentiated to obtain the right-hand-side of the GS equation, which is solved in the cross-section using the following parameters:

- $\Delta y = 0.1 \Delta x$

- $n_y = 271$

- The solution is filtered using the filter detailed in section 4.4.2 and $\alpha = 2/3$.

The impact parameter obtained is $y_0 = 0.0325$ AU, the axial magnetic field at the center is $B_z^0 = 12.3$ nT and the axial current density at the center is $J_z^0 = 1.256$ pA/m^2

64

The results of the reconstruction can be seen in figure 6.11. On the B_z and J_z plots, we have represented the magnetic measurements of the spacecraft in the x-y plane with white arrows. The x and y components have been represented in the B_x and B_y plots, respectively.
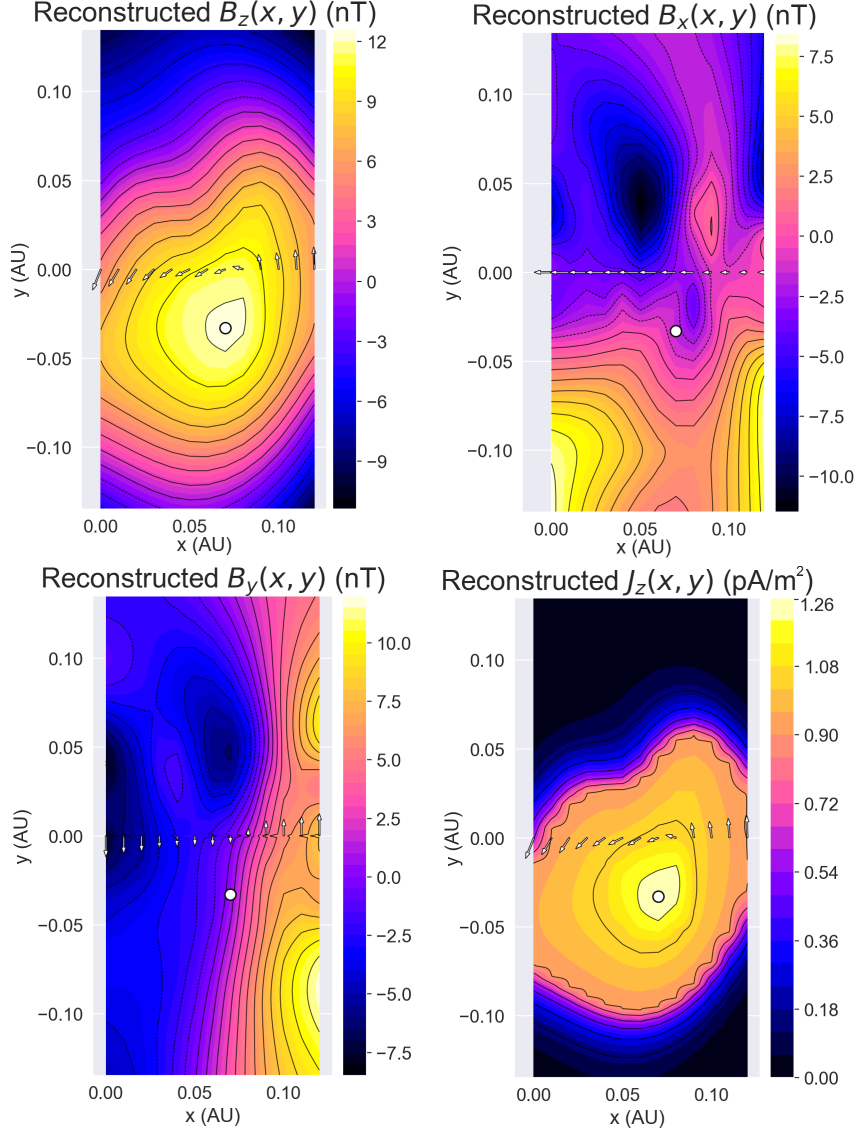
Figure 6.11: At the top-left, the reconstructed magnetic field B_z, at the top-right, B_x, at the bottom-left B_y and at the bottom-right, the axial current density j_z in the MFR cross-section.

From the axial current density, we can compute the total (axial) current through the cross-section, by integrating j_z in the MFR boundary. This leads to a current value of $I = 322.5$ A.

Figure 6.11 shows that the cross-section of the flux rope ($A_z(x, y)$ or $B_z(x, y)$ plot) is looks like an ellipse with some rotation. Motivated by this fact, ellipses were fitted to the plot of $A_z(x, y)$ for different values of the potential. Each ellipse provided a major and minor axis from which the distortion could be determined. Plus, the rotation angle could also be determined. Next, we present the results obtained, where the uncertainty of each parameter is the standard deviation.

- Distortion $\delta = 0.7300 \pm 0.0136$

- Ellipse rotation angle $\xi = (-37.71 \pm 2.45)°$

In figure 6.12, the distortion and rotation angle of the ellipse are plotted against the major semiaxis

of the fitted ellipse. We can see that the distortion ranges from 0.72 to 0.77 while the rotation axis ranges from around -42° to -34°.
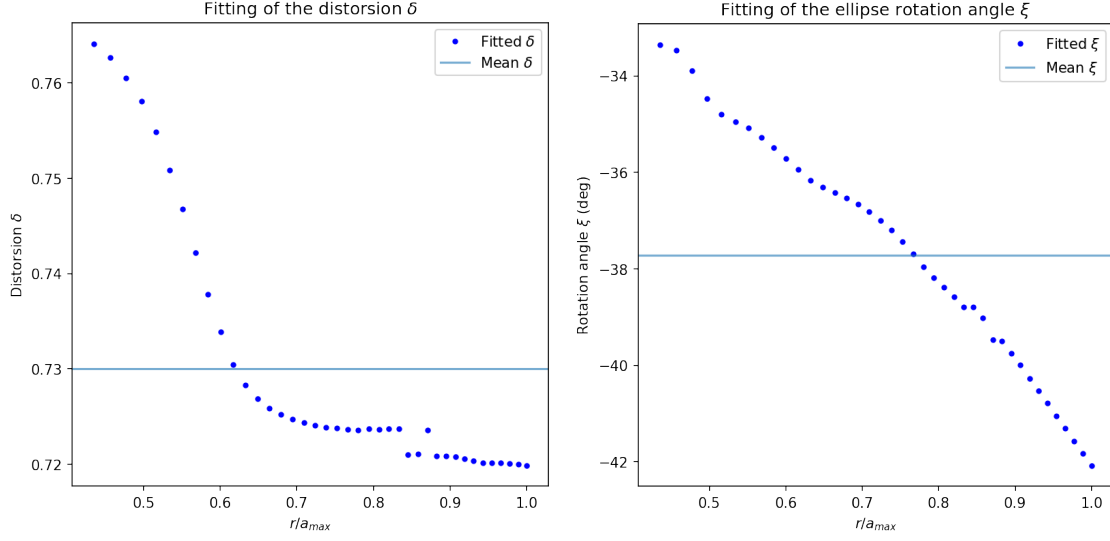
Figure 6.12: (Left) Distortion δ of the fitting ellipses for different values of the major semiaxis. The distortion is greater near the center of the MFR and decreases towards its boundary. (Right) Ellipse rotation angle ξ of the fitting ellipsed for different values of the major semiaxis. The rotation ranges from -34° near the center to -42° at the boundary.

Finally, we provide a summary of all the important magnitudes and parameters of this event.

Summary of the results

- Times:
  - Start time: 00:50:00 h
  - End time: 12:14:00 h
  - Total elapsed time: 11h 23 min

- Velocities:
  - Leading edge speed: $\|\boldsymbol{v_l}\| = 529.7$ km/s
  - Trailing edge speed: $\|\boldsymbol{v_t}\| = 469.8$ km/s
  - Expansion speed: $v_{exp} = \dfrac{\|\boldsymbol{v_l} - \boldsymbol{v_t}\|}{2} = 32.76$ km/s $= 0.06669\|\boldsymbol{v}_{HT}\|$

- Axis orientation:
  - MVAB: $\varphi = 220.0°$, $\theta = 41.8°$
  - MVUB: $\varphi = 221.0°$, $\theta = 39.7°$
  - Miniumum residue direction: $\varphi = 220°$, $\theta = 32°$

- Physical magnitudes:
  - Central axial magnetic field $B_z^0 = 12.3$ nT
  - Central axial current density $J_z^0 = 1.256$ pA/m^2
  - Total axial current $I = 322.5$ A

- Geometrical parameters:

66

- Impact parameter $y_0 = 0.0325$ AU
- Central axial field $B_z^0 = 12.3$ nT
- Current $I = 322.5$ A
- Distortion $\delta = 0.7300 \pm 0.0136$
- Ellipse rotation angle $\xi = (-37.71 \pm 2.45)°$

6.3   More real event analysis

In this work we have only presented the analysis of a real event. However, the tool created has the potential of analyzing an infinitude of other interesting ICMEs. This is why, together with Dr. Nieves-Chinchilla, we are preparing a paper in which we will present the analysis with a novel event.

We are also collaborating with Fernando Carcaboso in the analysis of the May, 16-18, 2012 event measured by two different spacecrafts at different angles. Figure 6.13 shows the fist results of the reconstruction.

Figure 6.13: Reconstructed cross-section of the May, 16-18, 2012 event measured by STEREO A. A fraction of the magnetic flux rope can be observed at the lower center part of the figure.

7. Accomplishments, conclusions and future work

7.1 Accomplishments and outcomes

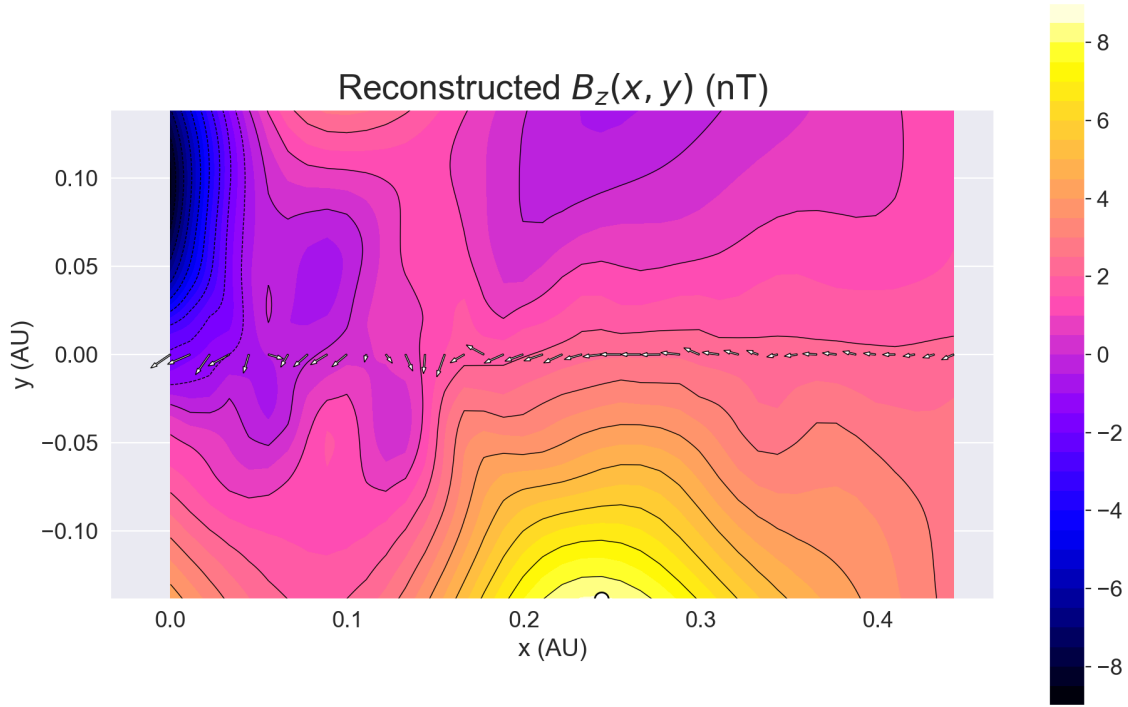We believe that two main accomplishments have been made at the end of this research. In the first place, a Grad-Shafranov Reconstruction Technique tool has been developed with `Python`. The tool is able to compute many physical magnitudes of the flux rope such as magnetic field, current density, Lorentz force, twist and pressure. The program is able to carry out the whole analysis of an event: from the data treatment to the post-processing of the physical magnitudes. The determination of the distortion of the flux rope has been automated and added as a functionality of the program. In short, an open-source, easy-to-use complete tool to analyze magnetic structures in the heliosphere using in-situ measurements has been made available to the scientific community.

The second main achievement we have accomplished is the connection between the Grad-Shafranov Reconstruction Technique and the CC and EC model. Both methods are able to describe and reconstruct magnetic flux ropes with high accuracy. The CC and EC models have been used as input for the GSRT and the technique was able to reconstruct the cross-section of the MFR with accuracy.

As for my personal accomplishments, I believe that the realization of this thesis has had an impact on me in many different aspects. First of all, we fully had the science researcher experience. From knowing nothing about a topic to being able to discuss advanced questions with senior researchers there is a process. I describe this process as being utterly stressful sometimes, but very rewarding in the end. I firmly believe that the opportunity to present a poster in the American Geophysical Union (AGU) Fall Meeting 2021 was an enriching experience. I realized that communication, both written and spoken in research is more important than it may look at first. Also, the opportunity of presenting my thesis in front of the heliophysics department at NASA GSFC, answering the questions, doubts and listening to the feedback was an enlightening experience. And my work does not stop here, I am giving an oral presentation at the European Geophysical Union (EGU) General Assembly 2022 at the end of May. We are also in preparation of an article together with Nieves-Chinchilla on the connection between the CC and EC models with the GSRT. In this paper, we are planning to provide an analysis of a recent event measured by Solar Orbiter or Parker Solar Probe. Furthermore, other outcomes of this research are the collaboration with Marcel Ayora in a paper related to the calculus of current densities profiles inside MFRs using a 4-spacecraft configuration like Cluster. In addition, we are also collaborating with Fernando Carcaboso on a novel analysis of a multi-spacecraft measurement of an ICME.

7.2 Conclusions

The main conclusions of our research are the following:

- The validity of the GSRT tool has been checked by the analysis of a real event previously and its comparison with the results obtained by Möstl et al. (2009).

- The created tool is able to reconstruct flux ropes defined by the CC and EC models when their pressure is calculated with the momentum equation for plasma in equilibrium. The CC and EC model fulfils the GS equation.

- We are able to determine the distortion of the flux rope using the GSRT when the distortions between $\delta = 0.6$ and $\delta = 1$.

- The results of the GSRT can vary substantially depending on the parameters, filters and fitting functions used. These details should always be indicated when the method is applied.

7.3   Future work

Some work we believe could be done in the same direction as our research is:

- The implementation of a multi-spacecraft GSRT. How can we treat the multiple boundary conditions provided by several spacecraft?

- The implementation of the toroidal GSRT using Python. A large fraction of the provided code for the cylindrical GSRT could be reused and adapted.

- The study of the Grad-Shafranov equation for a toroidal geometry with a distortion could be of special interest since flux ropes have been observed to present a non-negligible distortion in their cross-section that cannot be explained using the toroidal GS equation.

- The creation of a GUI based on the `Python` code provided for even easier use of the GSRT. A good starting point could be the use of the GUI Amun-Solar Application by Fernando Carcaboso.

- Further research on the effect of noise in the measurements to the GSRT.

- Use the provided tool to analyze a large number of events and extract meaningful parameters in order to perform a statistical study with them.

8. Annex

8.1 Grad-Shafranov equation for circular geometry

In this section we derive the Grad-Shafranov equation for circular geometry, that is, there is no variation in the azimuthal coordinate φ. For this reason we will use cylindrical coordinates (see equations (3.1) and (3.2)).

We start from Ampère-Maxwell's law and using the expression for the curl in cylindrical coordinates (equation (3.4)):

$$\boldsymbol{B} = \boldsymbol{\nabla} \times \boldsymbol{A} = -\frac{\partial A_\varphi}{\partial z}\hat{\boldsymbol{e}}_{\boldsymbol{r}} + \left(\frac{\partial A_r}{\partial z} - \frac{\partial A_z}{\partial r}\right)\hat{\boldsymbol{e}}_{\boldsymbol{\varphi}} + \frac{1}{r}\frac{\partial\left(rA_\varphi\right)}{\partial r}\hat{\boldsymbol{e}}_{\boldsymbol{z}} \tag{8.1}$$

We observe that the following mathematical equality holds: $\boldsymbol{\nabla} \times (A_\varphi\hat{\boldsymbol{e}}_{\boldsymbol{\varphi}}) = -\frac{\partial A_\varphi}{\partial z}\hat{\boldsymbol{e}}_{\boldsymbol{r}} + \frac{1}{r}\frac{\partial(rA_\varphi)}{\partial r}\hat{\boldsymbol{e}}_{\boldsymbol{z}}$. The two terms of the right hand side of this expression appear in equation (8.1). Therefore we can express the $\boldsymbol{B}$ as:

$$\boldsymbol{B} = \boldsymbol{\nabla} \times (A_\varphi\hat{\boldsymbol{e}}_{\boldsymbol{\varphi}}) + \left(\frac{\partial A_r}{\partial z} - \frac{\partial A_z}{\partial r}\right)\hat{\boldsymbol{e}}_{\boldsymbol{\varphi}} \tag{8.2}$$

Note that the previous equation expresses the magnetic field as its azimuthal component (second term) and component perpendicular to $\hat{\boldsymbol{e}}_{\boldsymbol{\varphi}}$ (first term).

Next, two key definitions are introduced:

$$\Psi(r,z) := -rA_\varphi \qquad\qquad \text{(Poloidal magnetic flux)} \tag{8.3}$$

$$F(r,z) := rB_\varphi = r\left(\frac{\partial A_r}{\partial z} - \frac{\partial A_z}{\partial r}\right) \qquad\qquad \text{(Poloidal current)} \tag{8.4}$$

where Ψ is the poloidal stream funcion and represents the and represents the poloidal magnetic flux, whereas F is the poloidal current (Atanasiu et al., 2004). Recalling the expression of the gradient in cylindrical coordinates, one can calculate the gradient of φ:

$$\boldsymbol{\nabla}\varphi = \frac{1}{r}\hat{\boldsymbol{e}}_{\boldsymbol{\varphi}} \tag{8.5}$$

With this we can rewrite the first term of equation (8.2) as:

$$\boldsymbol{\nabla} \times (A_\varphi\hat{\boldsymbol{e}}_{\boldsymbol{\varphi}}) = \boldsymbol{\nabla} \times (-\Psi\boldsymbol{\nabla}\varphi) = -\boldsymbol{\nabla}\Psi \times \boldsymbol{\nabla}\varphi - \Psi\underbrace{(\boldsymbol{\nabla} \times \boldsymbol{\nabla}\varphi)}_{0} = \boldsymbol{\nabla}\varphi \times \boldsymbol{\nabla}\Psi \tag{8.6}$$

Where we have used the following two property of the curl: given g a scalar function and $\boldsymbol{H}$ a

vector field:

- The curl of the gradient of any scalar field g is always the zero vector field: $\boldsymbol{\nabla} \times (\boldsymbol{\nabla} g) = 0$

- Leibniz rule for the curl: $\boldsymbol{\nabla} \times (g\boldsymbol{H}) = (\boldsymbol{\nabla} g) \times \boldsymbol{H} + g(\boldsymbol{\nabla} \times \boldsymbol{H})$

With this and the previous definitions we can rewrite equation (8.2) as:

$$\boldsymbol{B} = \boldsymbol{\nabla}\varphi \times \boldsymbol{\nabla}\Psi + F\boldsymbol{\nabla}\varphi \tag{8.7}$$

By substituting the previous expression for the magnetic field into Ampère's equation, we obtain:

$$\mu_0 \boldsymbol{j} = \boldsymbol{\nabla} \times \boldsymbol{B} = \boldsymbol{\nabla} \times (\boldsymbol{\nabla}\varphi \times \boldsymbol{\nabla}\Psi) + \boldsymbol{\nabla} \times (F\boldsymbol{\nabla}\varphi) = \boldsymbol{\nabla} \times \left[\frac{1}{r}\hat{\boldsymbol{e}}_{\boldsymbol{\varphi}} \times \left(\frac{\partial\Psi}{\partial r}\boldsymbol{e_r} + \frac{\partial\Psi}{\partial z}\boldsymbol{e_z}\right)\right] + \boldsymbol{\nabla}F \times \boldsymbol{\nabla}\varphi \tag{8.8}$$

Performing the vector product and further expanding the expression we obtain:

$$\mu_0 \boldsymbol{j} = \left(\frac{\partial^2\Psi}{\partial z^2} - \frac{1}{r}\frac{\partial\Psi}{\partial r} + \frac{\partial^2\Psi}{\partial r^2}\right)\boldsymbol{\nabla}\varphi + \boldsymbol{\nabla}F \times \boldsymbol{\nabla}\varphi \tag{8.9}$$

We define the following elliptical operator:

$$\Delta^*\Psi = \frac{\partial^2\Psi}{\partial z^2} - \frac{1}{r}\frac{\partial\Psi}{\partial r} + \frac{\partial^2\Psi}{\partial r^2} \tag{8.10}$$

Therefore, we have $\mu_0 \boldsymbol{j} = \Delta^*\Psi\boldsymbol{\nabla}\varphi + \boldsymbol{\nabla}F \times \boldsymbol{\nabla}\varphi$.

Plugging the expressions for $\boldsymbol{j}$ and $\boldsymbol{B}$ into the momentum equation for a plasma in equilibrium:

$$\boldsymbol{\nabla}p = \boldsymbol{j} \times \boldsymbol{B} = \frac{1}{\mu_0}(\Delta^*\Psi\boldsymbol{\nabla}\varphi + \boldsymbol{\nabla}F \times \boldsymbol{\nabla}\varphi) \times (\boldsymbol{\nabla}\varphi \times \boldsymbol{\nabla}\Psi + F\boldsymbol{\nabla}\varphi) \tag{8.11}$$

To further simplify this expression we will show that the pressure is a function of just Ψ, that is, $p = p(\Psi)$. From the momentum equation, multiplying scalarly by $\boldsymbol{B}$ on both sides we get, on the one hand:

$$\boldsymbol{B} \cdot \boldsymbol{\nabla}p = \boldsymbol{B} \cdot (\boldsymbol{j} \times \boldsymbol{B}) = 0 \implies \boldsymbol{\nabla}p \perp \boldsymbol{B} \tag{8.12}$$

Since we have no dependencies on the angle φ we can write $\boldsymbol{\nabla}p = \frac{\partial p}{\partial r}\boldsymbol{e_r} + \frac{\partial p}{\partial y}\boldsymbol{e_y}$, which is perpendicular to $\hat{\boldsymbol{e}}_{\boldsymbol{\varphi}}$ and consequently also to $\boldsymbol{\nabla}\varphi$. Then, on the other hand we have:

$$0 = \boldsymbol{B} \cdot \boldsymbol{\nabla} p = (\boldsymbol{\nabla}\varphi \times \boldsymbol{\nabla}\Psi + g\boldsymbol{\nabla}\varphi) \cdot \boldsymbol{\nabla} p = (\boldsymbol{\nabla}\varphi \times \boldsymbol{\nabla}\Psi) \cdot \boldsymbol{\nabla} p = \left(\frac{\hat{\boldsymbol{e}}_{\boldsymbol{\varphi}}}{r} \times \boldsymbol{\nabla}\Psi\right) \cdot \boldsymbol{\nabla} p = \frac{\hat{\boldsymbol{e}}_{\boldsymbol{\varphi}}}{r} \cdot (\boldsymbol{\nabla}\Psi \times \boldsymbol{\nabla} p)$$

(8.13)

Since both $\boldsymbol{\nabla}\Psi$ and $\boldsymbol{\nabla} p$ are both perpendicular to $\hat{\boldsymbol{e}}_{\boldsymbol{\varphi}}$, the previous expression implies that $\boldsymbol{\nabla}\Psi \times \boldsymbol{\nabla} p = 0$, which means $\boldsymbol{\nabla}\Psi \parallel \boldsymbol{\nabla} p$. Since the gradients of both functions always point in the same direction, we conclude that we can express the pressure p only as a function of Ψ, and therefore $\boldsymbol{\nabla} p = \frac{\mathrm{d}p}{\mathrm{d}\Psi}\boldsymbol{\nabla}\Psi$ as we wanted.

An analogous procedure shows that $g = g(\Psi)$ and $\boldsymbol{\nabla} g = \frac{\mathrm{d}g}{\mathrm{d}\Psi}\boldsymbol{\nabla}\Psi$.

Combining this into equation (8.11) we obtain:

$$\frac{\mathrm{d}p}{\mathrm{d}\Psi}\boldsymbol{\nabla}\Psi = \frac{1}{\mu_0}(\Delta^*\Psi\boldsymbol{\nabla}\varphi + \frac{\mathrm{d}g}{\mathrm{d}\Psi}\boldsymbol{\nabla}\Psi \times \boldsymbol{\nabla}\varphi) \times (\boldsymbol{\nabla}\varphi \times \boldsymbol{\nabla}\Psi + F\boldsymbol{\nabla}\varphi) = \tag{8.14}$$

$$= \frac{1}{\mu_0}\Delta^*\Psi\boldsymbol{\nabla}\varphi \times (\boldsymbol{\nabla}\varphi \times \boldsymbol{\nabla}\Psi) + \frac{1}{\mu_0}F\left[\frac{\mathrm{d}g}{\mathrm{d}\Psi}(\boldsymbol{\nabla}\Psi \times \boldsymbol{\nabla}\varphi) \times \boldsymbol{\nabla}\varphi\right] = \tag{8.15}$$

$$= \frac{1}{\mu_0}\frac{\Delta^*\Psi}{r^2}\hat{\boldsymbol{e}}_{\boldsymbol{\varphi}} \times (\hat{\boldsymbol{e}}_{\boldsymbol{\varphi}} \times \boldsymbol{\nabla}\Psi) + \frac{1}{\mu_0}\frac{F}{r^2}\frac{\mathrm{d}F}{\mathrm{d}\Psi}(\boldsymbol{\nabla}\Psi \times \hat{\boldsymbol{e}}_{\boldsymbol{\varphi}}) \times \hat{\boldsymbol{e}}_{\boldsymbol{\varphi}} \tag{8.16}$$

Recalling that $\boldsymbol{\nabla}\Psi \perp \hat{\boldsymbol{e}}_{\boldsymbol{\varphi}}$ and $||\hat{\boldsymbol{e}}_{\boldsymbol{\varphi}}|| = 1$ we have that $\hat{\boldsymbol{e}}_{\boldsymbol{\varphi}} \times (\hat{\boldsymbol{e}}_{\boldsymbol{\varphi}} \times \boldsymbol{\nabla}\Psi) = (\boldsymbol{\nabla}\Psi \times \hat{\boldsymbol{e}}_{\boldsymbol{\varphi}}) \times \hat{\boldsymbol{e}}_{\boldsymbol{\varphi}} = -\boldsymbol{\nabla}\Psi$. Using this, the previous equation is simplified:

$$\mu_0\frac{\mathrm{d}p}{\mathrm{d}\Psi}\boldsymbol{\nabla}\Psi = -\frac{\Delta^*\Psi}{r^2}\boldsymbol{\nabla}\Psi - \frac{F}{r^2}\frac{\mathrm{d}F}{\mathrm{d}\Psi}\boldsymbol{\nabla}\Psi \tag{8.17}$$

We can get rid of the vector character of the equation, which finally leads to the Grad-Shafranov equation:

$$\Delta^*\Psi = -\mu_0 r^2\frac{\mathrm{d}p}{\mathrm{d}\Psi} - F\frac{\mathrm{d}F}{\mathrm{d}\Psi} \tag{8.18}$$

Bibliography

M. V. Alves, E. Echer, and W. D. Gonzalez. Geoeffectiveness of corotating interaction regions as measured by Dst index. *Journal of Geophysical Research*, 111(A7):A07S05, 2006. DOI. URL.

C. V. Atanasiu, S. Günter, K. Lackner, and I. G. Miron. Analytical solutions to the Grad–Shafranov equation. *Physics of Plasmas*, 11(7):3510–3518, July 2004. DOI. URL.

M. A. Berger and G. B. Field. The topological properties of magnetic helicity. *Journal of Fluid Mechanics*, 147(-1):133, Oct. 1984. DOI. URL.

D. A. Daniel, A. H. Mishi, J. O. Love, R. John, A. D. Amos, and D. S. Yaula. Derivation and Applications of Grad-Shafranov Equation In Magnetohydrodynamics (MHD). page 5, 2021.

P. A. Davidson. *Introduction to Magnetohydrodynamics*. University of Cambridge, 2nd edition edition, Feb. 2017. URL.

P. Démoulin and S. Dasso. Causes and consequences of magnetic cloud expansion. *Astronomy & Astrophysics*, 498(2):551–566, May 2009. DOI. URL.

E. T. F. De Hoffmann. Magneto-hydrodynamic shocks. *Physical Review*, 80(4):692–703, July 1950. DOI. URL.

M. Florido-Llinàs. Study of the kink instability and twist distribution of heliospheric magnetic flux ropes. 2020. URL.

R. Garner. Parker Solar Probe Instruments, Feb. 2021. URL.

G. A. Gary. Plasma beta above a solar active region - rethinking the paradigm. *Solar Physics*, 203:16, 2001. DOI.

J. P. H. Goedbloed and S. Poedts. *Principles of Magnetohydrodynamics*. Cambridge University, 2004. URL.

H. Grad and H. Rubin. Hydromagnetic Equilibria and Force-Free Fields. *Proceedings of the 2nd UN Conference on the Peaceful Uses of Atomic Energy, Geneva*, 31, 1958. URL.

L.-N. Hau and B. U. Sonnerup. Two-dimensional coherent structures in the magnetopause: Recovery of static equilibria from single-spacecraft data. *Journal of Geophysical Research: Space Physics*, 104(A4):6899–6917, Apr. 1999. DOI. URL.

P. Holoborodko. Smooth noise-robust differentiators, 2008. URL.

T. Howard. *Coronal Mass Ejections - An introduction*. Springer, 2011. URL.

Q. Hu. The Grad-Shafranov Reconstruction of Toroidal Magnetic Flux Ropes: Method Development and Benchmark Studies. *Solar Physics*, 292(9):116, Sept. 2017a. DOI. URL. arXiv: 1706.02732.

Q. Hu. The Grad-Shafranov reconstruction in twenty years: 1996–2016. *Science China Earth Sciences*, 60(8):1466–1494, Aug. 2017b. DOI. URL.

Q. Hu and B. U. Sonnerup. Magnetopause transects from two spacecraft: A comparison. *Geophysical Research Letters*, 27(10):1443–1446, May 2000. DOI. URL.

Q. Hu and B. U. Sonnerup. Reconstruction of magnetic flux ropes in the solar wind. *Geophysical Research Letters*, 28(3):467–470, Feb. 2001. DOI. URL.

Q. Hu and B. U. Sonnerup. Reconstruction of magnetic clouds in the solar wind: Orientations and configurations. *Journal of Geophysical Research*, 107(A7):1142, 2002. DOI. URL.

Q. Hu, M. G. Linton, B. E. Wood, P. Riley, and T. Nieves-Chinchilla. The Grad-Shafranov Reconstruction of Toroidal Magnetic Flux Ropes: First Applications. *Solar Physics*, 292(11): 171, Nov. 2017. DOI. URL. arXiv: 1707.09454.

Q. Hu, W. He, L. Zhao, and E. Lu. Configuration of a Magnetic Cloud from Solar Orbiter and Wind Spacecraft In-situ Measurements. 2021. URL.

L. Jian, C. T. Russell, J. G. Luhmann, and R. M. Skoug. Properties of Interplanetary Coronal Mass Ejections at One AU During 1995 – 2004. *Solar Physics*, 239(1-2):393–436, Dec. 2006. DOI. URL.

R. P. Lepping, J. A. Jones, and L. F. Burlaga. Magnetic field structure of interplanetary magnetic clouds at 1 AU. *Journal of Geophysical Research*, 95, 1990. DOI.

B. F. Massimo Materassi and S. S. Anthea J. Coster, editors. *The Dynamical Ionosphere: A Systems Approach to Ionospheric Irregularity*. Elsevier, 2020. URL.

D. D. G. Mohsen Sheikholeslami. *Applications of Semi Analytical Methods for Nanofluid Flow and Heat Transfer*. 2018.

C. Möstl, C. J. Farrugia, H. K. Biernat, M. Leitner, E. K. J. Kilpua, A. B. Galvin, and J. G. Luhmann. Optimized Grad – Shafranov Reconstruction of a Magnetic Cloud Using STEREO-Wind Observations. *Solar Physics*, 256(1-2):427–441, May 2009. DOI. URL.

T. Nieves-Chinchilla, M. G. Linton, M. A. Hidalgo, A. Vourlidas, N. P. Savani, A. Szabo, C. Farrugia, and W. Yu. A Circular-cylindrical Flux-Rope Analytical Model for Magnetic Clouds. *The Astrophysical Journal*, 823(1):27, May 2016. DOI. URL.

T. Nieves-Chinchilla, M. G. Linton, M. A. Hidalgo, and A. Vourlidas. Elliptic-cylindrical Analytical Flux Rope Model for Magnetic Clouds. *The Astrophysical Journal*, 861(2):139, July 2018. DOI. URL.

E. Parker. Dynamics of the Interplanetary Gas and Magnetic Fields. *Astrophysical Journal*, 128: 664, 1958. DOI.

G. Paschmann and P. W. Daly. Analysis Methods for Multi-Spacecraft Data. page 536, 1998.

T. Paschmann and B. U. Sonnerup. Proper Frame Determination and Walén Test. page 10, 2008.

C. H. M. e. a. S. Dasso. Magnetic helicity analysis of an interplanetary twisted flux tube. *Journal of Geophysical Research*, 108(A10):1362, 2003. DOI. URL.

V. Shafranov. Plasma equilibrium in a magnetic field. *Reviews of Plasma Physics*, 2, 1966.

M. Skan. Reconstructing ICMEs with the toroidal Grad-Shafranov method. 2019. URL.

B. U. Sonnerup and M. Guo. Magnetopause transects. *Geophysical Research Letters*, 23(25): 3679–3682, Dec. 1996. DOI. URL.

B. U. Sonnerup, H. Hasegawa, W.-L. Teh, and L.-N. Hau. Grad-Shafranov reconstruction: An overview. *Journal of Geophysical Research*, 111(A9):A09204, 2006. DOI. URL.

L. Villanueva. A study of the solar wind from the Voyager spacecraft, 1977-1992. *Massachusetts Institute of Technology, Dept. of Physics*, 1994.